Riker, J. M., Cashman, K. V., Rust, A. C., & Blundy, J. D. (2015). Experimental constraints on plagioclase crystallization during H_2O- and H_2O-CO_2-saturated magma decompression. *Journal of Petrology, 56*(10), 1967-1998. [egv059]. https://doi.org/10.1093/petrology/egv059

Experimental Constraints on Plagioclase Crystallization during H_2O- and H_2O–CO_2-Saturated Magma Decompression

Jenny M. Riker*, Katharine V. Cashman, Alison C. Rust, Jon D. Blundy
School of Earth Sciences, University of Bristol, Bristol, BS8 2PU, United Kingdom

*Corresponding author: Tel: +44 (0)117 331 5181. Fax: +44 (0)117 925 3385. Email: jenny.riker@bristol.ac.uk

Running Title: Decompression-Driven Plagioclase Crystallization

Keywords: crystal textures; magma decompression; magma degassing; Mount St. Helens; plagioclase feldspar

Abstract

Experiments simulating magma decompression allow the textures of volcanic rocks to be calibrated against known eruptive conditions. Interpretation of natural samples may be complicated, however, by both the decompression path and the composition of exsolving volatiles, which affect the time evolution of crystal textures. Here we present the results of decompression experiments at elevated temperature and pressure designed to assess the effects of degassing path on crystallization of Mount St. Helens rhyodacite. Three families of experiments were employed to simulate varied PH_2O–*t* trajectories: single-step, H_2O-saturated decompression (SSD); continuous, H_2O-saturated decompression (CD); and continuous, H_2O–CO_2 saturated decompression. Quantitative textural data (crystal abundance, number density, and size) are used to calculate plagioclase nucleation and growth rates and assess deviations from equilibrium in run products. These are the first experiments to quantify feldspar nucleation and growth rates during H_2O–CO_2 saturated decompression. We find that reducing the initial melt water content through addition of CO_2 increases nucleation rates relative to the pure water case, an effect most pronounced at low d*P*/d*t*. Moreover, these early-formed textural distinctions persist at the lowest pressures examined, suggesting that deep H_2O–CO_2 fluids could leave a lasting textural 'fingerprint' on erupted magmas. Crystals formed prior to decompression during the annealing process also modulate sample textures, and growth on pre-existing crystals contributes significantly to added crystallinity at a wide range of experimental conditions. The phase assemblage itself is a dynamic variable that can be used in conjunction with textural data to infer conditions of magma ascent and eruption. Finally, quantitative textural data from experimental samples are compared to those of natural pyroclasts erupted during the summer 1980 explosive-effusive transition at Mount St. Helens. This comparison supports a model of magma ejected from multiple storage regions present in the upper crust following the May 18 Plinian eruption, such that subsequent eruptions tapped magmas that experienced varied decompression and degassing histories.

INTRODUCTION

Magma ascent controls, to a large extent, the style of volcanic eruptions. The reasons for this are largely kinetic – timescales of decompression-driven vesiculation and crystallization strongly influence the ease of gas escape from viscous melts (Cashman, 2004; Rust & Cashman, 2011). Vesiculation is the dominant process operating on very short timescales (seconds to minutes; Gardner *et al.* 1999; Mourtada-Bonnefoi & Laporte 1999); however,

feedbacks between water exsolution, which raises the liquidus temperatures of anhydrous minerals (Tuttle & Bowen, 1958), and crystallization in response to degassing become increasingly important at longer timescales (t > hours; Hammer & Rutherford 2002; Couch *et al.* 2003; Martel & Schmidt 2003). The interplay between gas loss and crystallization is therefore relevant to a wide spectrum of eruptive behavior in arc volcanic settings, from moderately explosive to effusive. Because the timescales of eruptive activity and crystallization overlap, disequilibrium features – in particular groundmass textures – provide important constraints on magma ascent histories, and by extension, eruption dynamics (Cashman, 1992; Hammer *et al.,* 1999; Cashman & McConnell, 2005; Pichavant *et al.,* 2007; Blundy & Cashman, 2008).

Experiments simulating magmatic decompression provide a means of calibrating textures against known ascent conditions. Early work first established the relevance of degassing-induced crystallization on magmatic and volcanic timescales (Fenn, 1977; Swanson, 1977; Muncill & Lasaga, 1988; Geschwind & Rutherford, 1995). Since then, a rapidly expanding body of experimental literature has aimed to correlate quantitative descriptors of crystal texture (i.e., abundance, number density, size, and morphology) with kinetic variables such as undercooling ($\Delta T = T_{liq}–T$, the difference between the phase liquidus temperature and the experimental run temperature), decompression rate (dP/dt), and time (Hammer & Rutherford, 2002; Couch *et al.,* 2003; Martel & Schmidt, 2003; Pupier *et al.,* 2008; Brugger & Hammer, 2010*a*; Cichy *et al.,* 2011; Martel, 2012; Mollard *et al.,* 2012; Arzilli & Carroll, 2013; Shea & Hammer, 2013). Together these studies establish baseline crystallization kinetics of common magmatic minerals (Hammer & Rutherford, 2002; Martel & Schmidt, 2003; Mollard *et al.,* 2012), provide a context for linking groundmass crystal textures to specific eruptive events (Couch *et al.,* 2003; Szramek *et al.,* 2006; Suzuki *et al.,* 2007; Blundy & Cashman, 2008; Martel, 2012), and compare the textural "fingerprints" of decompression- and cooling-induced crystallization (Arzilli & Carroll, 2013; Shea & Hammer, 2013). The collective results of dynamic decompression experiments suggest the potential for applications as geospeedometers (Rutherford & Hill, 1993; Toramaru, 2008) and geobarometers (Blundy & Cashman, 2008; Mollard *et al.,* 2012) and provide an essential reference for numerical models of magma ascent (Melnik & Sparks, 2005).

A key theme arising from the growing cache of experimental data is that decompression path – not simply rate – affects the evolution of crystal textures, in particular of feldspar, which is the dominant crystallizing phase in intermediate to silicic bulk compositions. Experiments have typically employed one of three P–t paths: an instantaneous "single-step"

pressure drop, followed by a fixed dwell time at final pressure (SSD, or "static" decompression experiments, after Hammer 2008); a continuous, controlled decompression at a constant rate, designed to simulate steady ascent (CD, or "dynamic" decompression); or a series of small pressure steps and intervening dwell times (MSD, or multi-step decompression), also approximating dynamic ascent, but employed out of technical necessity (Brugger & Hammer, 2010*a*). Comparisons of decompressions along different P–*t* paths at the same time-integrated decompression rate (= ΔP/time available for crystallization) have revealed striking contrasts in the evolution of feldspar abundance and morphology (Hammer & Rutherford, 2002; Couch *et al.,* 2003; Brugger & Hammer, 2010*a*; Martel, 2012).

An avenue that remains largely unexplored from a kinetic standpoint is the effect of fluid composition during progressive decompression, where PH_2O–*t* paths vary along different degassing trajectories (Riker *et al.,* in press). Although H_2O is typically the most abundant volatile species in silicate melts, CO_2 is almost always present, and its presence has a strong modulating effect on H_2O solubility. Only one previous work compares crystallization kinetics in H_2O and H_2O–CO_2 bearing systems (Cichy *et al.,* 2011); their study investigates varied decompression rates at constant terminal pressure but does not consider the time-evolution of crystal textures. These observations highlight the need for experimental studies that simulate the effects of varied PH_2O–*t* ascent paths on the evolution of magmatic textures, and that directly compare experimentally generated textures with those of well-contextualized natural samples.

Here we present the results of laboratory decompression experiments on rhyodacitic melt saturated with H_2O and H_2O–CO_2 fluids. These experiments simulate magma decompression from shallow crustal to near-surface pressures along varied PH_2O–*t* paths. Our target composition is a rhyodacite from Mount St. Helens, a volcanic system whose erupted products are well characterized, and for which an extensive record of quantitative textural data already exists (Cashman, 1988, 1992; Cashman & McConnell, 2005; Muir *et al.,* 2012). Through quantitative assessment of experimentally-generated crystal textures, proportions, and nucleation and growth rates, we assess the effect of H_2O and H_2O–CO_2 saturated decompression on the time-evolution of crystal textures and phase relations and evaluate the role of growth on pre-existing crystals in decompressing magmas. Although both points have been considered in previous works (Cichy *et al.*, 2001; Martel. 2012), we go significantly further in quantifying the kinetic effects of these processes. We conclude by comparing textural parameters derived from experimental and natural data sets to constrain the evolution of the magmatic plumbing system during recent eruptions of Mount St. Helens.

EXPERIMENTAL AND ANALYTICAL METHODS

Experimental Methods

Experimental strategy

H_2O exsolution from decompressing magma triggers crystallization in a manner analogous to cooling (Yoder, 1965; Anderson, 1984; Blundy & Cashman, 2001; Hammer & Rutherford, 2002); this change is driven by the difference in free energy between metastable melt+vapor and stable melt+vapor+crystals. The magnitude of this free energy change scales with the effective undercooling, ΔT_{eff} (hereafter simply ΔT), defined as the difference between the liquidus temperature of the phase of interest and the ambient temperature (e.g., Hammer & Rutherford 2002). Together with time, ΔT is an important variable modulating the evolution of crystal textures.

Our experimental strategy utilizes decompressions along different PH_2O–*t* trajectories, and thus different ΔT–*t* trajectories, to investigate the effect of ascent path on textural development. Experiments may be grouped into three series. In the first series, decompression was executed in a single-step (SSD), after which the sample was allowed to dwell at final pressure (P_f) for a period of one day or one week prior to quench. In these runs, water exsolves rapidly following the pressure step, and the system responds to a near-instantaneous ΔT. In the remaining two series, samples were decompressed continuously (CD) at a range of rates; these series differ only in the initial fluid composition in the charge ($XH_2O^{fl} = 1.0$ versus 0.8). Continuously decompressed samples were quenched at varying P_f along each decompression path, affording snapshots of the temporal evolution of crystal textures (e.g., Hammer & Rutherford, 2002; Brugger & Hammer, 2010*a*). In these runs, the imposed undercooling is a function of time – a "dynamic" undercooling, $d\Delta T/dt$ – that reflects both the melt H_2O content and the crystallization efficiency at all previous pressures (Hammer, 2008). All else being equal, the different PH_2O–P_{total} trajectories defined by water-saturated and closed-system degassing (e.g., Riker *et al.,* in press) should yield distinct PH_2O–*t* paths that are relevant to natural decompressing magmas.

CD experiments were run at decompression rates of 1 and 10 MPa hr^{-1}. These values correspond to magma ascent rates characteristic of effusive to low-intensity explosive volcanic eruptions, as estimated by a variety of techniques (seismicity, mass eruption rate, petrologic constraints; e.g., Rutherford 2008). A single additional run at 100 MPa hr^{-1} more closely approximates decompression during explosive eruptions. Quench pressures (100, 50,

and 25 MPa) are identical in each series and correspond to a region of shallow storage depths inferred for the post-1980 magmatic plumbing system of Mount St. Helens (MSH; Cashman, 1992; Cashman & McConnell, 2005).

Initial conditions (temperature and initial pressure, P_i) were chosen to match those of an upper crustal magma storage region feeding the 1980–1986 MSH eruptions. Combined constraints from phase equilibria experiments (Rutherford *et al.,* 1985; Rutherford & Devine, 1988; Gardner *et al.,* 1995b; Rutherford & Devine, 2008) and petrologic analysis of erupted products (Blundy *et al.,* 2008) indicate pre-eruptive storage pressures of 220–320 MPa, temperatures between 870–875 °C, and an oxygen fugacity near NNO+1. Our exact starting conditions, P_i = 200 MPa and T = 885 °C, differ slightly from these values owing to physical limitations of the experimental apparatus, as well as our desire to minimize the proportion of plagioclase formed during equilibration. The initial fluid composition selected for H_2O–CO_2 bearing runs (X_{H2O}^{fl} = 0.8) corresponds to that anticipated at our P_i and run T for closed-system degassing of a representative Mount St. Helens melt inclusion composition (after Blundy *et al.* 2010).

Our experiments and analysis focus on plagioclase feldspar, the most abundant groundmass phase in many natural magmas and in our chosen experimental system. Feldspar crystallization is highly sensitive to changes in both PH_2O and ΔT (Fenn, 1977; Swanson, 1977; Geschwind & Rutherford, 1995; Hammer & Rutherford, 2002) and therefore represents the ideal marker of magmatic decompression conditions.

Starting materials

The starting material used for all decompression experiments is a synthetic, volatile-free analog of the Sugar Bowl rhyodacite (dome sample DS-63 of Smith & Leeman 1987). This evolved composition is well-suited to the study of groundmass crystallization at Mount St. Helens, as it falls at the intersection of whole rock and groundmass glass major element trends (e.g., Blundy *et al.* 2008). Phase equilibria studies on the same starting powder (Fig. 1; Riker *et al.,* in press) provide a baseline for our decompression experiments, and full details of material preparation can be found therein. Briefly, the powder was prepared as a mechanical mixture of oxides and carbonates, decarbonated in a box furnace, then repeatedly heated in a gas-buffered vertical furnace equilibrated at NNO+1 (near the ambient fO_2 imposed by the Ni-alloy pressure vessel), quenched to glass, and reground to homogenize. The measured major element composition of starting material SB3 is given in Table 1.

Experimental procedure

For each run, ~50 mg of starting powder was loaded into a 3 mm diameter Au75Pd25 capsule, along with sufficient liquid water and (in CO_2-bearing runs) $Ag_2C_2O_4$ to saturate the charge with a fluid of target composition. The necessary amounts of H_2O and $Ag_2C_2O_4$ were determined directly from the results of phase equilibria experiments. Loaded capsules were micro-welded shut, then weighed and heated to check for mass loss. Although a gold–palladium alloy is not required by our run temperatures, Au failed repeatedly during decompression to P_f = 25 MPa in pilot experiments; AuPd significantly reduced the incidence of capsule leakage, either by preventing pressure welding of the capsule crimp, or through its added mechanical strength. If the latter, we note the possibility of a slight overpressure in runs at the lowest P_f, such that P_f <50 MPa are minimum values.

Decompression experiments were run in externally heated cold seal Nimonic pressure vessels at the University of Bristol, or in identical apparatus at the University of Oregon. A nickel alloy filler rod was used to position samples in the hotspot of the external furnace, and static pressure was applied using water as the pressurizing medium. Temperature was maintained at 885±5 °C using K-type thermocouples and monitored throughout each run. Pressure was monitored using both digital transducers and factory-calibrated Heise gauges; pressure was maintained to within ±1 MPa of the target value during periods of isobaric equilibration (i.e., anneal and dwell periods). All charges were allowed to equilibrate at P_i for a fixed period of time prior to the onset of decompression (72 hours for XH_2O^{fl} = 1.0 and 168 hours XH_2O^{fl} = 0.8, as required by the initial melt H_2O content). Following this "anneal" period, single-step decompressions were executed manually by opening a pressure bleed valve to bring the run near-instantaneously to the desired P_f. Continuous decompressions employed a programmable pressure controller linked to a motorized screw to drive a piston into or out of an external water-filled reservoir (Johnston & Senkovich, 2007). Throughout decompression, these external controllers regulated pressure to within 0.2 MPa of the set point, although a slight offset was sometimes observed between digital gauges on the pressure controller and cold seal apparatus (always <1 MPa). Two samples (XH_2O^{fl} = 1.0 and XH_2O^{fl} = 0.8) were not decompressed, but were quenched immediately following the anneal period (Fig. 2). These reference samples provide information on the equilibrium state of our charges prior to the onset of decompression.

The oxygen fugacities of select experiments were monitored using a conventional NiPd sensor technique (Taylor *et al.,* 1992; Pownceby & O'Neill, 1994). In these runs, a sealed, 2

mm diameter Pd capsule containing a combination of $Ni(OH)_2 \pm Ni \pm H_2O$ was positioned in the holder, adjacent to the sample capsule. This allowed the displacement of fO_2 relative to the NNO buffer to be monitored via the alloying of nickel metal with the Pd capsule (Taylor *et al.,* 1992). Electron microprobe analysis of capsule walls yields fO_2 of NNO+2±0.7 (calculated using the activity–composition relationships of Pownceby & O'Neill 1994); due to a functional relationship between fH_2 and water activity, the true fO_2 in CO_2-bearing charges will be slightly lower than measured values (e.g., Scaillet & Evans, 1999; Sisson *et al.,* 2005). Although these conditions are somewhat more oxidizing than our target fO_2, they should not affect the textural evolution of plagioclase feldspar, as demonstrated by Martel *et al.* (2012) for experiments at NNO+1 and NNO+3 .

After quench, capsules containing a pure H_2O fluid were weighed and pierced to confirm water saturation. CO_2-bearing charges were weighed and then frozen; the fluid compositions were measured by mass balance by puncturing the frozen capsule, weighing to determine the mass of free CO_2, then heating and reweighing to determine the mass of free water (e.g., Tamic *et al.* 2001). The final fluid composition was calculated from the masses (m) of excess H_2O and CO_2 released from the charge as:

$$XH_2O^{fl} = (m_{H2O}/18.01)/ [(m_{H2O}/18.01) + (m_{CO2} /44.02)] \quad (1)$$

Both initial (pre-decompression) and final (post-decompression) fluid compositions are reported in Table 2; except where explicitly stated, XH_2O^{fl} refers to the initial fluid composition of a charge.

Analytical methods

Compositional analysis

The compositions of quenched experimental glasses were analyzed on a Cameca SX-100 electron microprobe at the University of Bristol. Glass analyses were run at 15 kV accelerating voltage and 2 nA beam current using a 10–15 μm beam diameter to minimize alkali migration (Humphreys *et al.,* 2006). During data reduction, H was processed as a by-difference element to yield estimates of dissolved H_2O content. Reported compositions are an average of 10–15 analyses per charge (see supplementary materials).

Textural analysis

Two methods of quantitative textural characterization are widely employed in the

volcanological literature: those based on two-dimensional attributes of the bulk crystal population ("batch" methods; e.g., Hammer & Rutherford 2002), and those based on the density distribution of individual crystal sizes (the crystal size distribution, or CSD; e.g., Randolph & Larson 1971; Marsh 1988). Batch methods and similar bulk calculation techniques (such as those based on maximum crystal length, L_{max}) are routinely used to estimate crystal growth and nucleation rates in experimental studies (Hammer & Rutherford, 2002; Couch *et al.,* 2003; Martel & Schmidt, 2003; Brugger & Hammer, 2010*a*; Martel, 2012; Mollard *et al.,* 2012; Arzilli & Carroll, 2013; Shea & Hammer, 2013). This approach is rapid and may be confidently applied when the crystallization timescale is known. Published examples of experimentally constrained CSDs are rare (exceptions include Pupier *et al.,* 2008; Brugger & Hammer, 2010*a*; Cichy *et al.,* 2011). Textural studies of natural samples, in contrast, often utilize the complete crystal size distribution as a means of extracting kinetic information (e.g., Armienti, 2008; Blundy & Cashman, 2008). Following the convention of previous experimental work, we emphasize batch-calculated kinetic parameters in this study. However, to facilitate application of our results to existing natural datasets, including several for Mount St. Helens (Cashman, 1988, 1992; Cashman & McConnell, 2005; Muir *et al.,* 2012), we have acquired full CSDs for a subset of 17 samples.

Back-scattered electron (BSE) images of polished, carbon-coated sample mounts were acquired on a Hitachi S-3500N scanning electron microscope (SEM) at the University of Bristol (15 kV accelerating voltage, 10 mm working distance). Up to six images were acquired from representative regions of each sample at magnifications of 200×, 250×, or 500×. Plagioclase crystals in each image were thresholded according to their greyscale values and then converted to binary images using the image processing freeware ImageJ (distributed by the National Institute of Health; Abràmoff *et al.* 2004). Touching crystals were digitally separated on the basis of visual inspection of crystal shape and orientation. Axially radiating crystals were treated as separate nucleation sites. Conversely, closely spaced, sub-parallel dendritic lathes present at high undercoolings were assumed to represent planar sections of radiator-shaped forms (e.g., Hammer & Rutherford 2002) and treated as single nucleation sites.

ImageJ enabled automated measurement of crystal number, area, and size (calculated as the major and minor axes of an equivalent ellipse) in each binary image. The resolution of this approach, determined from the minimum object size included in measurements (10 pixels, as recommended by Higgins 2006), is ~0.8 μm at the highest magnifications utilized. To ensure appropriate treatment of edge-intersecting crystals, each image was processed

twice: once including crystals in contact with the image boundary (for determination of the total crystal area), and once excluding these crystals (for complete crystal size distributions; Higgins, 2006; Hammer, 2008). Areal number densities include a count from two of the four image boundaries.

Batch calculations Image analysis output was used to calculate the plagioclase area fraction (ϕ) and areal number density (N_A, the number of crystals per unit area, in mm^{-2}) in each sample. Both values are normalized to a vesicle-free reference area (e.g., Hammer *et al.* 1999), also determined in ImageJ. For randomly oriented crystals, the area fraction may be assumed to equal the volume fraction, ϕ (DeHoff & Rhines, 1968). Together, N_A and ϕ give the characteristic two-dimensional crystal size, expressed as the square root of the mean crystal area,

$$S_N = (\phi / N_A)^{1/2}. \quad (2)$$

Volumetric number density, N_V, may then be calculated via a standard stereological conversion that corrects for cut and intersection effects (Underwood, 1970):

$$N_V = N_A / S_N \quad (3)$$

(Cheng & Lemlich, 1983; Hammer *et al.,* 1999; Blundy & Cashman, 2008). These values are related to time-integrated nucleation (I, $mm^{-3}\ s^{-1}$) and growth rates (G, $mm\ s^{-1}$) as

$$I = N_V / t \quad (4)$$

$$G = S_N / t, \quad (5)$$

where t is the crystallization interval (Hammer & Rutherford, 2002). Reported uncertainties in ϕ, N_A, S_N, G, and I are estimated from the 1σ variation between multiple analyzed images or, in cases where only a single image was analyzed, from the variation of sub-sampled crystal populations within each image.

The initial conditions of our experiments are below the plagioclase liquidus of the bulk composition, and in all runs, some feldspar crystallized during the initial equilibration period.

As these crystals did not form during decompression, we have subtracted the number density and abundance of plagioclase in equilibrium reference samples (422±74 mm^{-2} for DSB6 and 1018±80 mm^{-2} for DSB39) from measured N_A and ϕ prior to calculation of nucleation and growth rates (e.g., Brugger & Hammer 2010*a*). Throughout this paper, we report only the equilibrium-referenced N_A (= measured N_A – $N_{A\ REF}$), G, and I to facilitate comparison between pure water and mixed fluid experiments, which have different initial number densities.

Crystal size distributions Size information derived from image analysis may also be used to generate crystal size distributions (CSDs), which provide a statistical framework for the interpretation of quantitative textural parameters (Randolph & Larson, 1971; Cashman & Marsh, 1988; Marsh, 1988). The size distribution represents a population balance of crystals as they grow into (or out of) a specific size range, *L*, while fluxing into (or out of) a control volume of interest. This population balance may be described in terms of three key variables: G, the mean linear crystal growth rate; τ, the average crystal residence time; and n^0, the number density of nucleus-sized crystals (i.e., $L \rightarrow 0$; Cashman & Marsh, 1988).

The application of CSD theory to natural datasets requires conversion of areal (apparent) crystal dimensions to true three-dimensional crystal shapes. These conversions were executed using the software program CSDCorrections (v. 1.4; Higgins 2000), now widely used in the geological community for the generation of crystal size distributions. The program attempts to account for three sources of stereological error (e.g., Hammer *et al.* 1999): (1) cut effects, which result from planar sectioning of crystals at different orientations; (2) intersection probability, which means small crystals are less likely to be sectioned than larger ones; and (3) deviations arising from nonspherical crystal habit. Key inputs for CSDCorrections are measured crystal sizes, *L*, here defined as the long axis of a best-fit ellipse, as output by ImageJ. Additional required inputs include crystal shape (the ratios of short to intermediate to long axes), sample fabric, and grain roundness. Our samples contain no perceptible fabric, and a roundness factor of 0.1 was inferred for all samples based on visual inspection. Shape factors were determined using the Excel database CSDSlice (v. 5; Morgan & Jerram 2006), which compares the distribution of area-based crystal aspect ratios to those generated by random sectioning of known crystal shapes to determine the best-fit three-dimensional habit. Importantly, this assumes that a single shape factor applies to the entire crystal population.

From these data, logarithmic bin intervals of L were used to generate size distributions as cumulative plots of $\ln(n^0) > L$ (in mm^{-4}) versus L (in mm), as described by Marsh (1988) and Cashman & Marsh (1988). Quantitative kinetic information is derived by least-squares regression of the $\ln(n^0)$–L slope, which is inversely proportional to the product of growth rate and residence time:

$$\text{slope} = -1/G\tau \quad (6)$$

(Marsh, 1988). The regression intercept n^0 is equal to the ratio of nucleation and growth rates, such that

$$I = n^0 G. \quad (7)$$

Uncertainties in CSD-derived parameters have been estimated from the standard errors of regression intercepts and slopes, as reported in Table 4.

A tremendous diversity of approaches has been used to generate crystal size distributions since early applications of theory to magmatic crystallization. In particular, choices of characteristic crystal length L vary considerably (e.g., major axis length, caliper length, crystal width, square root of crystal area), as do approaches to stereological conversion (Peterson, 1996; Sahagian & Proussevitch, 1998; Higgins, 2000). Following Brugger & Hammer (2010*b*), we adopt methods and assumptions that have been widely used in recent textural studies of igneous systems. Our aim is to facilitate comparison of our experimental results with past (and future) datasets. This is important, as Muir *et al.* (2012) have shown that size distributions generated using different techniques applied to identical samples can yield vastly different values of calculated kinetic parameters.

RESULTS

Phase relations

All experimental run products contain glass, vesicles, and crystals formed during equilibration and subsequent decompression. Experimental mineral assemblages consist of plagioclase + Fe-Ti oxides ± amphibole ± orthopyroxene ± silica; plagioclase is the most abundant phase in all charges. Two reference samples equilibrated at P_i = 200 MPa contain plagioclase + amphibole + Fe-Ti oxides (at XH_2O^{fl} = 1.0) and plagioclase + amphibole + orthopyroxene + Fe-Ti oxides (at XH_2O^{fl} = 0.8), consistent with equilibrium P– XH_2O^{fl} phase

relations for the Sugar Bowl rhyodacite at 885 °C (Fig. 1). In contrast, the phase assemblages of decompressed samples may differ considerably from the equilibrium assemblage at a given quench pressure, P_f (Table 2).

In pure-H_2O runs, amphibole routinely persists to the lowest P_f examined (25 MPa); resorption (manifest as rounding) and incipient reaction rims form in slowly decompressed samples (dP/dt = 1 MPa hr^{-1}) at P_f <50 MPa and in a single instantaneous decompression to 50 MPa (dwell = 24 hrs). At higher decompression rates, amphibole crystals maintain euhedral forms throughout the decompression interval. Amphibole is absent from three single-step decompressions at high undercoolings (P_f = 25 MPa) and/or long dwell times (t = 168 hours), indicating complete reaction of the phase with surrounding melt at these conditions; given that experimental amphiboles are typically ~5–10 μm across, these observations imply hornblende reaction rates somewhat faster than those inferred by Rutherford & Hill (1993) for Mount St. Helens dacites. Also in pure-H_2O samples, orthopyroxene crystallization is delayed to pressures below the equilibrium curve, to <100 MPa at dP/dt = 1 MPa hr^{-1}, and to <25 MPa at $dP/dt \geq 10$ MPa hr^{-1}. In instantaneous decompressions, we observe orthopyroxene at all P_f <100 MPa and at all dwell t = 168 hours. Euhedral orthopyroxene often mantles rounded amphibole cores; this may be a reaction feature or a kinetic one (e.g., preferential heterogeneous nucleation of pyroxene crystals on amphibole), although it is texturally distinct from the fine-grained rims typically associated with hornblende breakdown (Rutherford & Hill, 1993; Browne & Gardner, 2006). A silica polymorph (probably cristobalite) forms only in single-step decompressions to low P_f, present as fractured, pseudo-hexagonal crystals up to 100 μm in length. Cristobalite forms between dwell times of 24 and 168 hours at P_f = 50 MPa, and in <24 hours at P_f = 25 MPa.

In CO_2-bearing decompressions (XH_2O^{fl} = 0.8), amphibole breakdown is shifted to higher pressures and/or shorter residence times, in keeping with equilibration conditions closer to the limiting H_2O content of amphibole stability (~4 wt%; Fig. 1). For dP/dt = 10 MPa hr^{-1}, reaction rims are observed at P_f = 25 MPa (compared to unreacted euhedral crystals in the pure-H_2O system at the same conditions); at lower dP/dt, incipient breakdown is observed at P_f = 100 MPa, and amphibole is absent by P_f = 50 MPa. Orthopyroxene is present in all CO_2-bearing charges, including the equilibrium reference sample. Orthopyroxene growth is evidenced by pronounced and generally sharp zonation of crystal rims towards more Fe-rich compositions, as indicated by semi-quantitative EDS. Silica is not observed in any decompressions at XH_2O^{fl} = 0.8.

Metastable phase assemblages are a common feature of decompression experiments (Hammer & Rutherford, 2002; Cichy *et al.,* 2011; Martel, 2012; Shea & Hammer, 2013); the absence of phases that might otherwise be stable at final pressure is often attributed to a nucleation delay associated with the time required for structural reorganization of the melt (e.g., Fokin *et al.* 1981). What is clear from our experimental suite is that nucleation lags are not a unique function of time, as also emphasized by the results of Brugger & Hammer (2010a). As a consequence, samples with comparable crystallization intervals (decompression time, t_{dc} + dwell time, t_{dw}) but different decompression rates may contain disparate assemblages. Under disequilibrium conditions, then, the phase assemblage is not independent of the decompression path. Rather, the assemblage itself is a dynamic variable with the potential to provide key information about the ascent history of its host magma.

Phase Compositions

Compositions of experimental glasses and plagioclase crystals are reported in the supplementary materials. Glass compositions record progressive melt evolution in response to decompression-driven crystallization, with incompatible components like K_2O (Fig. 4) becoming concentrated in the melt with decreasing P_f in all three sets of experiments. Glass K_2O contents of water-saturated decompression experiments are compared to those from a corresponding set of isobaric experiments (Riker *et al.*, in press) in Figs. 4a and c (no corresponding dataset is available for runs at $XH_2O = 0.8$). In continuous decompressions, glass compositions lag behind equilibrium values at all experimental P_f, suggesting equilibrium crystallinities are not achieved at any point during decompression. Moreover, the gap between experimental and equilibrium glass compositions increases systematically with increasing decompression rate, as also observed by Brugger & Hammer (2010*a*). In contrast, single-step decompressions reach equilibrium melt K_2O contents within 24 hours, after which point melt K_2O remains constant. Hammer & Rutherford (2002) note a similar distinction between single-step and multi-step decompressions, although their SSD runs do not reach equilibrium crystallinities at $P_f < 40$ even after 7 days, perhaps owing to the lower temperature and/or more silicic composition of their experiments.

Plagioclase compositions are known to be strongly dependent on PH_2O (e.g., Putirka, 2005), and experimental plagioclase anorthite contents span a range of values in each sample (5 to >20 mol% An; Fig. 4). These ranges record plagioclase crystallization at varied melt water contents during or after decompression, and show that early-formed cores fail to re-equilibrate on the timescales of our runs. In keeping with the findings of previous

experimental studies (Castro & Gardner, 2008; Brugger & Hammer, 2010*a*; Mollard *et al.*, 2012), compositions are not clearly correlated with crystal size or decompression rate. Compositional zones in our experimental plagioclase crystals are often smaller than the electron beam, such that many analyses represent a mixture of cores and rims. As such, it is difficult to capture the complete compositional range in all samples. The most anorthitic crystals in H_2O–saturated runs have $An_{52–56}$ (exceptions are two SSD runs at P_f = 50 MPa, in which we may not have captured the most calcic crystals) and reflect the compositions of plagioclase formed during the initial anneal period; the maximum An contents in H_2O–CO_2–saturated runs are more sodic ($An_{46–50}$) owing to lower initial melt water contents. The clearest distinction between our three sets of experiments, however, is in their approach to equilibrium An contents (Riker *et al.*, in press). For a given P_f, the most albitic plagioclase crystals are consistently more calcic than equilibrium values in continuous decompression experiments (both H_2O- and H_2O–CO_2-saturated), while plagioclase in single-step decompressions reach equilibrium compositions at all but the lowest P_f (despite, in many cases, shorter run durations). Plagioclase in SSD runs at P_f = 25 MPa may extend to more albitic compositions that could not be captured due to the small size of newly-formed crystals and rims, an interpretation consistent with equilibrium glass K_2O contents in these samples.

That glass compositions sensitively record the extent of crystallization of decompressed samples is consistent with previous experimental work (Hammer & Rutherford, 2002; Couch *et al.* 2003), which has shown that concentrations of incompatible elements in decompressed glasses more closely approach equilibrium values in single-step decompressions than in continuous or multi-step decompressions of similar duration. The compositions of crystallizing plagioclase, however, may be expected to depend on both melt water content (a function of P_f) and melt composition (i.e., degree of crystallization). In CD experiments, then, plagioclase compositions may fall short of equilibrium because of limited crystallization time at low water contents, or because crystallization itself is not keeping pace; more likely, both factors contribute to the lag in equilibrium anorthite contents. It is also possible that feldspar crystals have very thin rims in equilibrium with surrounding melt, which cannot be measured by conventional techniques.

Plagioclase textures

Feldspar crystallized in all decompressed samples by way of nucleation and/or growth (Fig. 3). Plagioclase microlites formed during decompression are observed at all quench pressures and decompression rates and constrain nucleation delays to <100 hours for runs at 1 MPa hr^{-}

485 [1], <10 hours at 10 MPa hr^{-1}, and (for XH_2O^{fl} = 1.0) <1 hour at 100 MPa hr^{-1}. For SSD
486 experiments, nucleation delays are <24 hours. Evidence of feldspar growth in pure-H_2O runs
487 is given by a marked increase in the apparent size of the largest crystals (relative to the
488 equilibrium reference sample) and the ubiquitous presence of low-greyscale crystal rims
489 visible in BSE images. Because greyscale in BSE mode is proportional to mean atomic
490 number, these darker rims reflect growth of more albitic plagioclase on pre-existing "cores"
491 formed during the anneal period (Fig. 3a,b). Contrast between feldspar cores and rims
492 (proportional to the difference in anorthite content) increases with decreasing P_f. The nature
493 of zonation also varies systematically with decompression rate: core-rim boundaries are
494 diffuse in runs at 1 MPa hr^{-1} and sharpest in the SSD series (Fig. 3a,f). Unequivocal evidence
495 of plagioclase zoning in CO_2-bearing experiments is visible only in runs with P_f <50 MPa
496 (Fig. 3c,d).
497
498 *Plagioclase morphology*
499 Feldspar morphology is known to be a strong function of undercooling (Lofgren, 1980;
500 Kirkpatrick, 1981; Hammer & Rutherford, 2002), and visual inspection of BSE images shows
501 coherent variation of crystal forms within each experimental series (Fig. 3). Here we adopt
502 the terminology of Shea & Hammer (2013) to describe feldspar textures as a function of
503 morphology (euhedral, hopper/swallowtail, skeletal), habit (blocky, elongate, tabular, or
504 acicular, in order of increasing aspect ratio) and crystal arrangement (individual, clustered, or
505 spherulitic).
506
507 *Continuous decompression (XH_2O^{fl} = 1.0)* Pure-H_2O CD experiments are characterized
508 by euhedral feldspar crystals. Swallowtail or skeletal overgrowths are visible on crystal rims
509 at $P_f \leq 50$ MPa in slowly decompressed samples (1 MPa hr^{-1}), and at all P_f for more rapid
510 decompressions. These disequilibrium features become increasingly abundant with
511 decreasing P_f or, at constant P_f, with increasing decompression rate. Plagioclase habits are
512 generally elongate to tabular; shape factors suggest that at each decompression rate, growing
513 crystals become first slightly more equant (e.g., long: intermediate axis ratio, *l*:*i*, decreases
514 relative to the equilibrium reference) before aspect ratios increase at low P_f (from *l*:*i* <2 to *l*:*i*
515 = 3–4). There is no clear relationship between aspect ratio and d*P*/d*t*. Rare smaller crystals
516 (presumably nucleated during the decompression interval) have hopper or skeletal forms and
517 higher aspect ratios than their larger counterparts. Crystals in this series tend to be isolated,
518 although occasional crystal clusters appear at high d*P*/d*t* and low P_f.

519

520 *Continuous decompression (XH_2O^{fl} = 0.8)* Feldspars with hopper morphologies are
521 abundant in CO_2-bearing experiments, in keeping with their prevalence in the reference
522 sample equilibrated at XH_2O^{fl} = 0.8 (Fig. 2). In contrast to pure-H_2O runs, plagioclase
523 morphologies display limited variation across the range of conditions examined. Hopper
524 forms are dominant at all P_f and dP/dt, while skeletal crystals are rare in this sample suite.
525 Crystal habits are acicular in planar section; aspect ratios decrease with decreasing P_f but are
526 uncorrelated with dP/dt. Although newly nucleated crystals appear to be abundant, they are
527 not easily distinguished from crystals formed during equilibration on the basis of
528 morphology. Instead, textural variations in H_2O–CO_2 runs are manifest primarily as
529 variations in plagioclase size and abundance. The differences between pure-H_2O and CO_2-
530 bearing runs suggest that the evolution of crystal morphologies in our experiments is strongly
531 modulated by the initial fluid composition. This modulating effect persists throughout the
532 decompression interval.
533

534 *Single-step decompression (XH_2O^{fl} = 1.0)* Non-euhedral feldspar forms are common in
535 all SSD experiments, consistent with the large ΔT imposed by instantaneous decompression.
536 These evolve from predominantly hopper and swallowtail habits at P_f = 100 MPa to
537 predominantly skeletal habits at P_f = 25 MPa. New plagioclase forms as both overgrowths on
538 subhedral prismatic cores (formed during the anneal) and as smaller, isolated crystals
539 nucleated during decompression. The latter become increasingly abundant at $P_f \leq 50$ MPa,
540 generating a distinctly bimodal population of plagioclase crystals (Fig. 3). Crystal habits are
541 tabular to acicular, and aspect ratios progress towards more acicular habits with decreasing
542 quench pressure. Shape factors were not determined for two experiments decompressed to P_f
543 = 25 MPa, because 2D intersection-based techniques do not provide meaningful shape
544 descriptors of skeletal crystal forms (e.g., Higgins 2006); however, visual inspection suggests
545 that aspect ratios of newly-formed dendrites are even higher in these runs. Plagioclase forms
546 primarily individual crystals at P_f = 100 MPa, while clustered and spherulitic arrangements
547 are common at lower P_f. Dendrites in high ΔT experiments manifest as groups of parallel
548 laths which may be connected in three dimensions (e.g., Hammer & Rutherford 2002). SSD
549 runs at identical P_f also provide snapshots of the temporal evolution of crystal morphologies
550 at dwell times of one day and one week. Some rounding of crystals can be seen in the time
551 series at P_f = 100 MPa. In runs at $P_f \leq 50$ MPa, feldspar morphologies do not appear to vary

552 on the timescales investigated.
553
554 *Plagioclase abundance, number density, and size*
555 The evolution of experimentally generated plagioclase textures can be quantitatively
556 described in terms of volumetric abundance (ϕ), areal number density (N_A), and characteristic
557 crystal size (S_N). These data are plotted against quench pressure in Figure 5a–c for each
558 experimental series. For CD experiments, trends represent the time evolution of textural
559 parameters during progressive decompression. At a given decompression rate, the length of
560 the crystallization interval increases along the x-axis. For SSD experiments, symbols
561 designate experiments with identical crystallization intervals following the application of
562 progressively higher ΔT (i.e., lower P_f). To enable more direct comparison to the time
563 sequence represented by CD experiments, the data from SSD runs are also plotted against t_{dw}
564 in Figure 5d.
565 Plagioclase volume fractions in all series show an accelerating increase in ϕ with
566 decreasing P_f. In water-saturated runs, these values may be directly compared to those
567 measured in equilibrium experiments at the same quench pressure (Riker *et al.,* in press; Fig.
568 6). For CO_2-bearing decompressions, equilibrium plagioclase volume fractions are estimated
569 from measured melt water contents (see supplementary materials) using a simple, polynomial
570 parameterization of the ϕ–H_2O relationship of water-saturated phase equilibria experiments
571 (e.g., Riker *et al.,* in press).
572 Feldspar abundances echo trends recorded by glass compositions. In CD experiments
573 (XH_2O^{fl} = 1.0 and 0.8), ϕ are consistently lower than equilibrium values, and deviation from
574 equilibrium ϕ increases systematically with decreasing quench pressure. This effect is most
575 pronounced in the single run at dP/dt = 100 MPa hr^{-1}, where crystallinity at P_f = 25 MPa is
576 less than a third of that measured in the corresponding equilibrium experiment. Crystallinities
577 in runs at 1 and 10 MPa hr^{-1} are both about half that of the equilibrium experiment at the
578 same P_f. In SSD experiments, ϕ values are coincident with the equilibrium curve for all P_f,
579 regardless of dwell time, implying that most plagioclase crystallizes within 24 hours of
580 decompression. After this period, plagioclase ϕ remains more or less constant (Fig. 6d).
581 The degree to which plagioclase crystallization keeps pace with (or lags behind)
582 equilibrium in our experiments can be ascribed primarily to (a) decompression rate and (b)
583 time available for crystallization. At the large instantaneous undercoolings experienced by
584 SSD runs, equilibrium crystallinities are rapidly achieved at all P_f. In contrast, the short

crystallization interval associated with continuous decompression at high dP/dt limits the time available for crystallization, even though the effective undercooling (in this case a dynamic undercooling, dΔT/dt) is relatively large. At slow to intermediate decompression rates (1–10 MPa hr^{-1}), the competing effects of undercooling and time appear to balance one another, such that ϕ at any given P_f remains fairly constant across an order of magnitude change in the decompression rate. This fortuitous effect has been observed in previous experimental studies (Brugger & Hammer, 2010*a*; Cichy *et al.,* 2011) and suggests that, at a wide range of geologically relevant decompression rates, plagioclase crystallinity alone is insensitive to ascent conditions. Perhaps also fortuitously, initial ϕ and/or fluid composition appear to have little effect on the evolution of plagioclase crystallinity at the range of conditions examined.

Areal plagioclase number densities vary coherently both within and between series. At every decompression rate, CD experiments show an accelerating increase in N_A with decreasing quench pressure. Plagioclase number densities also increase with increasing decompression rate. In pure-H_2O runs, N_A achieve maximum values of 827, 1673, and 1857 mm^{-2} at P_f = 25 MPa for dP/dt = 1, 10, and 100 MPa hr^{-1}, respectively. N_A are consistently higher in CO_2-bearing runs, with maxima of 1702 and 2984 mm^{-2} at 1 and 10 MPa hr^{-1}. In CD runs, then, the number of crystals nucleated during decompression to any given P_f increases with dP/dt, despite the fact that the crystallization interval is proportionately shortened. SSD experiments also show a pronounced increase in plagioclase number density with decreasing quench pressure (increasing ΔT; Fig. 5c), with N_A nearly an order of magnitude higher than those observed in CD experiments at identical P_f (747–15,234 mm^{-2}; Table 4). Almost all crystals in SSD runs nucleate within the first 24 hours of the dwell period (Fig. 5d); subsequent time-dependence of N_A is either invariant within uncertainty (at P_f = 25 and 50 MPa) or slightly negative (at P_f = 100 MPa). These observations are consistent with an early nucleation event in all instantaneous decompressions (within one day of the imposed undercooling), followed by limited nucleation, or even ripening at high P_f, up to a dwell time of one week.

Apparent (2D) average plagioclase sizes range from 5–16 μm and, when plotted against P_f, reveal the shifting contributions of small and large crystals to the total crystallinity. Here we report the bulk-averaged quantity, S_N, rather than the maximum crystal length, L_{max} (e.g., Fenn 1977; Hammer & Rutherford 2002; Couch *et al.* 2003; Martel 2012), because crystals formed during annealing are not easily distinguished from those formed during

decompression, and L_{max} is less sensitive to size variations in the smallest (i.e., nucleating) crystals. In continuous decompressions, nearly all samples progress through a maximum S_N at some finite P_f. For a given quench pressure, S_N increases with decreasing dP/dt (Fig. 5). For XH_2O^{fl} = 1.0, S_N peaks at P_f = 50 MPa at 1MPa hr^{-1} (S_N =16μm) and P_f = 100 MPa at 10 MPa hr^{-1} (S_N =13μm). S_N peaks at P_f = 100 MPa for CO_2-bearing runs at 1 MPa hr^{-1} (S_N = 12 μm), although the amplitude of this peak is considerably smaller than those observed in the pure-H_2O system. Plagioclase crystals in CO_2-bearing runs decompressed at 10 MPa hr^{-1} show no clear peak size; instead, S_N = 9–10 μm at all experimental P_f. By analogy with pure-H_2O runs, crystal size may peak at higher pressure (i.e., we are not resolving the S_N maximum), or nucleation may balance the contributions of crystal growth across a wide decompression interval. The same is true of the single pure-H_2O run at 100 MPa hr^{-1} (S_N = 8 μm; Fig. 5), for which the presence or absence of a maximum crystal size cannot be determined. In SSD runs, S_N is highest at P_f = 100 MPa and drops off sharply with decreasing P_f (increasing ΔT). Because S_N is a function of ϕ and N_A, the time-variance of crystal size in SSD experiments mimics that of other textural parameters; that is, average size remains approximately constant (or increases slightly) between t_{dw} = 24 and 168 hours.

Average crystal sizes reveal something that is not immediately obvious from trends in ϕ and N_A, which is the competition between nucleation of new crystals and growth on pre-existing crystals that defines the distribution of crystal sizes in a sample with multiple crystal populations. The observed S_N maxima reflect a shift in the relative dominance of these two processes. In the following section, we examine this balance further through quantification of plagioclase nucleation and growth rates.

Plagioclase nucleation and growth rates

Batch calculations

The textural parameters ϕ, N_A, and S_N enable calculation of time-integrated plagioclase nucleation and growth rates according to the relationships in equations 2–5 ("batch" methods). Batch nucleation (I) and growth rates (G) for all experimental samples are reported in Table 3 and plotted against P_f in Figure 6. Calculated nucleation rates range from 10^{-2}–10^{1} mm^{-3} s^{-1} and are similar to those reported in previous experimental studies of plagioclase crystallization in silicic melts (10^{-3}–10^{2} mm^{-3} s^{-1}; Hammer & Rutherford 2002; Couch *et al.* 2003; Brugger & Hammer 2010*a*; Mollard *et al.* 2012). Because nucleation rates are coupled to areal number densities via equation 3, trends in I with changing P_f parallel those shown for

N_A (Fig. 5). However, for a given P_f, I is more sensitive to decompression rate, as the crystallization interval used to calculate I decreases with increasing dP/dt. Within and between series, the time-averaged nucleation rate increases with (a) decreasing P_f and (b) increasing decompression rate (Fig. 6). I is also consistently higher in CO_2-bearing runs than in H_2O-only runs at the same conditions. Unlike Brugger & Hammer (2010*a*), we observe no nucleation rate maxima in our experiments (despite overlapping ranges of dP/dt), suggesting that nucleation rates peak at $P_f < 25$ MPa.

Calculated plagioclase growth rates span three orders of magnitude ($G = 10^{-8}$–10^{-6} mm s^{-1}), also falling within the range measured in prior experimental studies (10^{-9}–10^{-6} mm s^{-1}; Hammer & Rutherford 2002; Couch *et al.* 2003; Brugger & Hammer 2010*a*; Mollard *et al.* 2012). Growth rates in CD experiments are strongly correlated with decompression rate, and within each CD series, an order of magnitude increase in dP/dt yields a corresponding increase in G (Fig. 6). Likewise, the range of G values is highest in faster decompressions. Growth rates in all CD runs decrease with decreasing P_f, such that no maxima are observed. In SSD experiments, average G decreases with P_f (for constant t_{dw}) and with t_{dw} between 24 and 168 hours at constant P_f. Time-averaged growth rates in SSD runs are typically lower than G measured for CD experiments, except at high P_f and short t_{dw}.

Crystal size distributions

Full plagioclase crystal size distributions (CSDs) have been calculated for a subset of 19 experimental samples (plotted as ln(n) versus L in Figure 7), including the two equilibrium runs, which are shown for reference. We report CSD-calculated nucleation and growth rates, in addition to batch-calculated rates, to facilitate comparison with kinetic parameters derived from studies of natural volcanic rocks.

All decompression experiments produce non-linear CSDs with concave upward and/or kinked forms (Fig. 7). An overturn in population density is frequently, but not always, observed in the smallest sizes (L = 1–4 μm), while the largest size class (or classes) of some samples exhibit a slight downturn. The latter may be an artifact of the imaging process, reflecting magnification scales too high to capture statistically meaningful numbers of the largest crystals; it may also record a lack of late nucleation. Overturns at small size classes have been variously attributed to ripening (e.g., Higgins & Roberge 2003; Pupier *et al.,* 2008), under-compensation for intersection probability (e.g., Brugger & Hammer 2010*b*), or insufficient resolution (e.g., Cashman & Ferry 1988; Hammer *et al.* 1999), although our image resolution is more than adequate to capture crystals >1 μm in length. The most

685 pronounced feature of our size distributions is, however, their curvature, which has been
686 ascribed to a plethora of natural processes in the volcanological literature (e.g., magma
687 mixing, crystal accumulation, textural coarsening, two-stage crystallization, or accelerating
688 nucleation and growth; Marsh 1988; Armienti *et al.* 1994; Higgins 1998; Bindeman 2003;
689 Higgins & Roberge 2003; Shea *et al.* 2010a), or to artifacts produced by the 2D–3D
690 conversion because of variations in crystal shape (Castro *et al.* 2004). Like Brugger &
691 Hammer (2010*b*), we interpret curvature based on the known experimental histories of these
692 samples, which includes two separate crystal populations (those formed during the initial
693 anneal period and those formed during decompression) with distinct nucleation regimes. The
694 strength of this curvature, and the crystal size, L, at its inflection point, vary with changing
695 decompression conditions and likely reflect the shifting contributions of nucleation and
696 growth to the evolution of each population.

697 Following convention, we fit our CSDs with two separate linear, ln(n)–L regressions,
698 one at small L (representing crystals formed during decompression), and one at large L
699 (representing crystals formed during the anneal period). Splitting the CSD into segments
700 requires a choice of L that divides the two crystal populations, and previous textural studies
701 have typically applied a fixed size class cut-off to all samples (Cashman, 1988; Piochi *et al.,*
702 2005; Salisbury *et al.,* 2008; Muir *et al.,* 2012). However, a fixed size range is unlikely to
703 characterize microlites grown under varied experimental conditions, nor do we have an
704 independent estimate of growth rate for crystals produced during annealing. To avoid
705 arbitrary or biased segmentation of size distributions, we have used a simple iterative
706 calculation to minimize the total residuals (Σr^2) of both regressions by varying the size
707 classes assigned to each fit. Slopes ($= -1/G\tau$) and intercepts ($= n^0$) for regressions fit to
708 decompression-nucleated crystals are reported in Table 4.

709 CSD-derived 3D nucleation and growth rates are almost always within an order of
710 magnitude of those estimated by batch techniques (Fig. 8). This close correspondence is
711 remarkable given the relatively large uncertainties in regression fits. Batch values of I are
712 typically displaced to slightly lower values than those derived from size distributions, as also
713 observed by Brugger & Hammer (2010*b*); in most cases the relative deviation is <40%.
714 Growth rates are in slightly poorer agreement, but are still within a factor of two. Our results
715 support the use of 2D textural analysis methods as an efficient alternative to the acquisition of
716 3D kinetic parameters (and one that involves considerably fewer stereological assumptions;
717 e.g., Cashman *et al.,* 1999; Hammer *et al.,* 2000; Brugger & Hammer, 2010*b*). An important
718 caveat is the need to separate different crystal populations when applying these methods to

natural samples.

While our feldspar nucleation and growth rates (both 2D and 3D) are consistent with the ranges reported in the experimental literature, they also reveal important distinctions between individual studies. Results from H_2O-saturated CD runs are most directly comparable to those of Brugger & Hammer (2010*a*, 2010*b*), who conducted continuous decompression of rhyolitic melt (71 wt% SiO_2) at a comparable temperature (880 °C) and range of decompression rates (0.5–10 MPa hr^{-1}). Batch-calculated growth rates are similar in the two studies: G as a function of P_f for the two datasets overlap and are often the same, within error, at a given decompression rate. Nucleation rates, however, are typically 1–2 orders of magnitude *lower* in our CD runs compared with those of Brugger & Hammer (2010a), with a parallel discrepancy seen in number densities (<3000 mm^{-2} in our runs, and up to 31,000 mm^{-2} in Brugger & Hammer 2010*a* and 2010*b*; only our SSD runs obtain N_A >10,000 mm^{-2}). As equilibrium plagioclase crystallinity curves in the two compositions are the same (cf. Fig. 5a with Fig. 8 of Brugger & Hammer 2010*a*), these distinctions point to different kinetic environments in the two sets of runs, despite similar compositions and run conditions. We consider possible reasons for these offsets in the following discussion.

DISCUSSION

The evolution of crystal textures during progressive crystallization reflects a balance between the thermodynamic factors that encourage crystallization and the kinetic factors that inhibit it (e.g., Dowty 1980; Kirkpatrick 1981; James 1985; Cashman, 1993). During isothermal decompression, effective undercooling (ΔT) provides the driving force for crystal formation, while melt viscosity, largely controlled by melt water content, presents the primary kinetic barrier to continued crystallization through its effect on both component diffusivities and crystal-melt interfacial energies (Hammer, 2008). In this way, crystallization kinetics are closely linked to the PH_2O–*t* path of decompressing magma. While no one path is a perfect analogy for magma decompression during all eruptive scenarios, the end-member paths simulated by our experiments bracket conditions that prevail during many volcanic eruptions. In the following discussion, we examine how the shifting balance between crystal nucleation and growth along varied degassing trajectories governs the evolution of magmatic textures. We emphasize three key observations stemming from this study: crystallization kinetics in CD versus SSD experiments; the effect of melt water content on crystal nucleation; and the influence of pre-existing crystals on crystal growth.

753 **Crystallization kinetics**

754 Crystallization kinetics are first examined for SSD experiments, which experience an initial,
755 quantifiable ΔT proportional to the experimental quench pressure P_f, as defined by the phase
756 diagram (e.g., Fig. 1). Trends in calculated nucleation and growth rates are consistent with
757 the functional relationships defined by kinetic theory (Kirkpatrick, 1981; James, 1985) and
758 observed in previous experimental studies of static decompression (Hammer & Rutherford,
759 2002; Couch *et al.,* 2003; Mollard *et al.,* 2012; Arzilli & Carroll, 2013; Shea & Hammer,
760 2013), such that nucleation rates increase, and growth rates decrease, with decreasing P_f
761 (increasing ΔT). More important, however, are the observed variations in average, or
762 *apparent* (time-integrated), growth and nucleation rates, which change with time because of
763 the non-linear response to temporal changes in undercooling as equilibrium conditions are
764 approached (Fig. 5d; e.g., Mollard *et al.,* 2012).

765 Changing crystallization rates with time are illustrated using the example of
766 experiments at P_f = 25 MPa (Fig. 9a). Here the apparent nucleation rates decrease from 635
767 $mm^{-2}\,hr^{-1}$ (or 12 $mm^{-3}\,s^{-1}$) to 87 $mm^{-2}\,hr^{-1}$ (2.1 $mm^{-3}\,s^{-1}$) as the t_{dw} increases from 24 to 168
768 hours. Moreover, instantaneous nucleation rates at shorter times must have been much higher,
769 although the exact values cannot be constrained. Evidence for more rapid rates of nucleation
770 can be found in the shortest CD experiment (100 MPa hr^{-1}), which records apparent
771 nucleation rates of 1061 $mm^{-2}hr^{-1}$ (38 $mm^{-3}s^{-1}$) over a crystallization time of 1.75 hours. The
772 same picture emerges for crystal growth rates (Fig. 9b). Here we also include SSD
773 experiments with P_f = 50 and 100 MPa, to include peak growth rates peak at P_f = 100 MPa,
774 where apparent growth rates decrease from 1.35 x 10^{-7} to 2.3 x 10^{-8} mm s^{-1} as dwell time
775 increases from 24 to 168 hours. As with nucleation, growth is most rapid (1.22 x 10^{-6} mm s^{-1})
776 in the short (1.75 hours) 100 MPa hr^{-1} CD experiments.

777 The data in Figure 9b show a systematic decrease in apparent growth rate (G) with
778 increasing crystallization time (t). A compilation of all the textural data (including runs at
779 XH_2O^{fl} = 0.8) shows that log G decreases linearly with *t* but with two distinct slopes: short
780 duration experiments (SSD with t_{dw} = 24 hours and all CD experiments performed at ≥ 10
781 MPa hr^{-1}) form one group, while long duration experiments (SSD with t_{dw} = 168 hours and
782 CD experiments performed at 1 MPa hr^{-1}) form another group (Fig. 9c). A linear fit to the
783 short duration experiments yields a slope of 0.05 and an intercept of -5.9 (or -5.8 if only pure
784 H_2O experiments are considered), which defines the most rapid crystal growth allowed under
785 these conditions. That this rate is close to the rate estimated for the 100 MPa hr^{-1} experiments
786 suggests that this decompression rate is close to the limiting rate allowable for

decompression-driven crystallization, such that we would expect more rapidly decompressed experiments to quench to glass.

The dynamic interplay between cooling rate and crystallization can be quantified using total crystallinity as a measure of chemical disequilibrium ($\Delta\phi = \phi^{eq} - \phi$, where ϕ^{eq} is the equilibrium crystallinity at $P = P_f$; Brugger & Hammer, 2010*a*). All SSD experiments achieve equilibrium ($\Delta\phi = 0 \pm$ experimental uncertainty) within 24 hours (Fig. 9d), following an inferred spike near $t = 0$ (assuming a crystallization lag longer than the timescale of decompression). CD experiments show a very different pattern, such that $\Delta\phi$ increases with time (decreasing P_f). At the lowest P_f (25 MPa), the maximum crystallization efficiency is achieved at the lowest decompression rate (1 MPa hr^{-1}), although crystallinities are still 10-20% lower than in SSD runs of similar duration. Higher $\Delta\phi$ values at both 100 and 10 MPa hr^{-1} most likely reflect limited time spent at either optimal nucleation or growth rates. The competing contributions of nucleation and growth to progressive crystallization may be quantified by the ratio I/G, equivalent to the intercept, n^0, of the ln(n)–*L* slope. I/G varies from 4×10^5 to 6×10^8 mm^{-4}, with the lowest values for slow CD experiments and highest values for SSD experiments. The shift in dominant crystallization mechanism from growth (low I/G) to nucleation (high I/G) is reflected in sample textures (Fig. 3). For H_2O-only experiments, crystals in growth-dominated CD runs are faceted with planar surfaces (indicating interface-limited growth at low effective undercoolings; Lofgren, 1974; Sunagawa, 1981) at all P_f, while nucleation-dominated SSD runs are characterized by abundant hopper and skeletal forms (indicating diffusion-limited growth at higher undercoolings; Lofgren, 1974; Donaldson, 1976; Sunagawa, 1981; Faure *et al.,* 2003). Average crystal sizes are consistently smaller in SSD runs (Fig. 5, 8b), again reflecting the dominance of nucleation over growth. Even the phase assemblage preserves a record of the decompression path, with delays observed in both the appearance of orthopyroxene and silica and the breakdown of amphibole in growth-dominated CD experiments relative to nucleation-dominated SSD experiments with similar crystallization intervals. These dynamic phase relations may reflect nucleation delays, in the classical sense (Sato *et al.,* 1981; Fokin *et al.,* 2006), which are sensitive to the imposed undercooling. Alternatively, they may arise from simple phase-equilibria constraints in PH_2O–T–X space (e.g., Martel 2012).

Similar textural distinctions have been observed in comparisons of single versus multi-step decompression (MSD; Hammer & Rutherford, 2002; Couch *et al.,* 2003) and stepped versus continuous decompression (Brugger & Hammer, 2010*a*). Textural variations in the

products of SSD and MSD experiments have been explained by variations in the effective undercooling imposed at each decompression step (or in infinitely small steps, during continuous decompression), which is much smaller than that imposed during instantaneous decompression (Hammer, 2008). Reduced dynamic undercooling in quasi-continuous decompressions encourages interface-controlled growth (Lofgren, 1974; Sunagawa, 1981); it also reduces the driving force for crystallization, causing crystallinity to lag behind equilibrium values, as seen in the consistently lower $\Delta\phi$ in our SSD relative to CD runs (Fig. 9d). Curiously, however, CD experiments appear to produce higher crystallinities than MSD experiments, despite morphological evidence consistent with higher effective undercooling in the latter (c.f. this study, Brugger & Hammer, 2010*a*). Taken together, these results raise the interesting possibility of a minimum crystallization efficiency at dynamic undercooling conditions intermediate between continuous and instantaneous decompression, perhaps corresponding to the gap between growth and nucleation rate maxima. These data underline the assertion of Brugger & Hammer (2010*a*) that crystallinity alone is a poor indicator of ascent rate or closure pressure in all but the most extreme conditions (i.e., very rapid ascent).

The effect of initial melt water content

A key finding of this study is that H_2O–CO_2-saturated charges have consistently higher nucleation (and conversely lower growth) rates than charges saturated with a pure-H_2O fluid. This observation is not entirely intuitive, as low rates of water loss during early decompression of mixed H_2O-CO_2 fluids may be expected to impose low instantaneous undercoolings, fostering crystal growth. Martel (2012) observed a similar increase in feldspar number density (nucleation rate) in water-undersaturated relative to water-saturated experiments, an effect she attributed to the presence of pre-existing crystals in undersaturated runs. All of our experiments, however, contain pre-existing crystals – if anything, we would expect the higher number density of plagioclase crystals in the H_2O–CO_2 reference sample to provide ready substrate for growth, thereby suppressing nucleation. We suggest that textural distinctions between H_2O and H_2O–CO_2 experiments reflect differences in the initial melt water content (5.8 versus 4.9 wt%, respectively, as estimated using the solubility model of Papale et al. 2006). By analogy with the temperature-dependence of steady-state nucleation in silicate melts, decreasing melt water content with respect to undercooling would shift the nucleation maximum to higher T (Fokin *et al.* 2006), consistent with the greater number and more skeletal habit of plagioclase in CO_2-bearing experiments (Fig. 3).

Different melt water contents at the onset of decompression present one possible explanation for the lower nucleation rates observed in our continuous decompressions compared to those of Brugger & Hammer (2010*a*). Their water-saturated runs initiate at lower pressure (P_i = 130 MPa, compared to 200 MPa in our water-saturated CD runs) and correspondingly lower water contents (4.3 wt%, as estimated by the authors). Comparison of our H_2O and H_2O–CO_2-saturated runs suggests that a 0.9 wt% reduction in initial water content increases nucleation rates by a factor of 2–7 at dP/dt of 1–10 MPa hr^{-1}. While significant, a further reduction of 0.6 wt% H_2O is probably insufficient to cause the 1–2 orders of magnitude offset in nucleation rates with the experiments of Brugger & Hammer, unless the system response is highly non-linear. Water contents are likely a contributing factor, but other variables – for example, differences in the degree of superheating of starting materials (Shea & Hammer 2013), or the presence and distribution of pre-existing crystals (discussed below) – may be needed to explain the offset fully.

Although the importance of melt H_2O content is well recognized in kinetic studies (Fenn, 1977; Muncill & Lasaga, 1988; Davis *et al.,* 1997; Fokin *et al.,* 2006), it is not often explicitly considered as a variable in experimental investigations of magmatic decompression. This may be, in part, because it is difficult to deconvolve the competing effects of ΔT and melt H_2O in experiments where water loss acts as the undercooling mechanism. The results of Shea & Hammer (2013), who compared cooling- and decompression-driven crystallization in hydrous mafic andesite, are significant in this respect: the apparent mechanism-independent behavior of experiments undercooled with respect to T and P would suggest that melt water content has a negligible effect on crystallization kinetics at all but the highest undercoolings (ΔT >137 °C in their experimental system). Based on these observations, the authors suggest that feldspar crystallization may be modeled as a path-independent process in P–T space. Our results raise an important caveat: at the high (near-instantaneous) undercoolings investigated by Shea & Hammer (2013), the thermodynamic driving force for crystallization far outweighs the inhibiting effects of lower melt water contents across the pressure range. In our CD experiments, where the instantaneous undercooling at any point in time is much lower, a modest decrease in the melt water content has a noticeable effect on crystallization kinetics. Specifically, decreasing PH_2O through the addition of CO_2 increases rates of crystal nucleation relative to growth and gives textural evidence (elongate skeletal crystals) of high effective supersaturations. These early-established textural distinctions persist throughout the decompression interval. In this way, initial fluid composition may modulate the evolution of plagioclase textures across a

887 wide pressure and/or depth range, particularly at the low effective $d\Delta T/dt$ associated with
888 slow, steady decompression.
889
890 **Interpreting magmatic textures: The importance of crystal growth**
891 Growth on pre-existing crystals is an important aspect of decompression-driven
892 crystallization in degassing magmatic systems (Cashman & Taggart, 1983; Cashman, 1988;
893 Martel & Schmidt, 2003). This process has generally been neglected in experimental
894 investigations, which tend to emphasize the formation of new crystals over growth of existing
895 ones. Although such studies provide important constraints on the baseline kinetics of
896 plagioclase crystallization in silicate melts, they may neglect other aspects of crystallization
897 in natural systems – namely the role of phenocrysts, microphenocrysts, and microlites in the
898 evolution of magmatic textures and compositions. Our experiments, which contain a
899 distributed population of feldspar crystals at the onset of decompression, afford an
900 opportunity to examine the influence of pre-existing crystals on subsequent growth and
901 nucleation of plagioclase.
902 The same data used to construct CSDs may be presented as crystal size–area histograms
903 (Fig. 10; see supplementary data for all plots), analogous to vesicle volume distributions used
904 to examine multiple vesicle populations (e.g., Klug *et al.,* 2002; Shea *et al.,* 2010). We
905 designate crystal size as the square root of crystal area, S_N, rather than L (the major axis of an
906 equivalent ellipse), to minimize variations introduced by differences in two-dimensional
907 crystal habits. Reference samples for H_2O and H_2O-saturated experiments (Fig. 10a,b) have
908 unimodal, approximately log-normal plagioclase size distributions with modes at ~10 μm.
909 Continuous decompression to 100 MPa preserves the unimodal shape of the distributions
910 while at the same time shifting the mode to larger sizes (recording growth of pre-existing
911 crystals) and extending the tail to smaller sizes (recording nucleation of new crystals; Fig.
912 10c,d). Further decompression to 25 MPa shows the development of a secondary mode at
913 large sizes and an increase in the small crystal population (Fig. 10e,f) that reflects the
914 increasing importance of crystal nucleation relative to growth at low pressures. Area
915 histograms from SSD experiments, in contrast, are dominated by small crystals, even at
916 moderate pressures, an observation consistent with nucleation-dominated crystallization (Fig.
917 10g,h). The most striking feature of the size histograms, however, is the area distribution of
918 crystals formed during the anneal period (shown as gray in Fig. 10), which we estimate from
919 the number density of plagioclase crystals in equilibrium reference samples by assuming the
920 largest crystals in each charge are those formed during equilibration. In almost all cases,

these crystals represent the majority of the area under the histogram curve. Although the shaded region includes a contribution from crystal "cores" formed prior to decompression (designated as ϕ^{eq} in Fig. 10), new growth still constitutes 25–50% of the total crystallinity in most samples. Thus, at most of the decompression conditions investigated, growth on pre-existing crystals contributes significantly to the total amount of crystallization.

This observation has important implications for interpreting volcanological processes from erupted products. For example, the chemical and textural "stratigraphy" preserved in complexly zoned phenocrysts is routinely used to interpret the T–X or PH_2O–T–X paths experienced by individual crystals during magma storage and ascent (Berlo *et al.,* 2007; Boyce & Hervig, 2008; Rutherford & Devine, 2008; Streck *et al.,* 2008; Thornber *et al.,* 2008; Saunders *et al.,* 2012; Cashman & Blundy, 2013). The most sophisticated of these studies link crystal rim chemistry to intensive variables via parameterization of experimentally constrained phase compositions and partition coefficients (e.g., Blundy & Cashman 2008; Cashman & Blundy, 2013), on the assumption that growth proceeds in equilibrium with surrounding melt. Disequilibrium, however, is a necessary condition of crystal growth. Kinetic studies have repeatedly documented departures from equilibrium mineral-melt partitioning, for example, of mafic components during cooling of basalt (Grove & Bence, 1979; Hammer, 2006) and of plagioclase components during decompression of hydrous silicic magmas (Brugger & Hammer, 2010*a*; Martel, 2012). While it is tempting to assume that phenocrysts grow primarily at near-equilibrium conditions (e.g., Costa *et al.* 2008), our experiments demonstrate that growth on preexisting crystals can contribute significantly to continued crystallization even at the high undercoolings associated with nucleation-dominated regimes.

As noted above, experimental studies have traditionally focused on nucleation and growth of groundmass crystals, yet most volcanic samples contain (abundant) phenocrysts. Our experiments further suggest that a substantial proportion of phenocryst growth could be syn-eruptive. Although many phenocrysts have antecrystic cores that reflect remobilization of near-solidus magma, crystal ages estimated from diffusion studies and CSDs are typically <100 years, suggesting that much of the crystallization occurs shortly before eruption (e.g., Cooper & Kent, 2014). Evidence to support this interpretation comes from comparisons of the phenocryst content of pumice clasts (the products of rapid decompression) and lavas (the products of slow decompression) from the same eruptive sequence (Fig. 11). Data from Mount St. Helens are best-constrained: magma of constant bulk composition was erupted at

954 rates that ranged from >1 m s^{-1} for pumice-forming eruptions (~100 MPa hr^{-1}; 24-28%
955 phenocrysts), to ~0.1 m s^{-1} for lava domes that immediately followed sub-Plinian eruptions
956 (~10 MPa hr^{-1}; 37-41% phenocrysts), to $<10^{-4}$ m s^{-1} during continuous lava spine extrusion
957 between 2004 and 2008 (~0.01 MPa hr^{-1}; 42-52% phenocrysts; Cashman *et al.,* 2008).
958 Importantly, increases in phenocryst content are accompanied by groundmass crystallization
959 that ranges from 0% in the pumice to ~40-50% in spine samples. These observations are
960 consistent with our experiments, which evidence abundant growth on pre-existing crystals
961 (phenocryst equivalents) at dome-forming decompression rates. The more extensive
962 phenocryst and groundmass crystallization observed in the spine samples is not surprising
963 given the much slower decompression of spine-producing magma. Similar patterns of
964 phenocryst abundance for other pumice-lava pairs (Colima, Merapi, and Mont Pelee; Fig. 11)
965 suggest that phenocryst growth adds substantially to the total extent of decompression-driven
966 syn-eruptive crystallization.
967 A final point relates to diffusion chronometry, which uses mineral zoning profiles to
968 quantify the timescales of volcanic processes (e.g., Morgan & Costa*,* 2010; Druitt *et al.,*
969 2012; Saunders *et al.,* 2012). Such studies model the diffusive relaxation of compositional
970 zoning as a function of time and require an a priori assumption regarding the form of the
971 compositional profile at $t = 0$. The most common assumption is that this profile is stepped
972 (Morgan *et al.,* 2004, 2006; Saunders *et al.,* 2012), although more complex initial profiles
973 have also been used (Costa *et al.,* 2008). In our experiments, compositional growth profiles
974 vary with decompression path. Although our crystals are too small for quantitative analysis,
975 we illustrate this point using the zoning profiles of plagioclase in two experimental samples
976 (Fig. 12, where grayscale is a proxy for anorthite content), one sharp, one diffuse. Both
977 samples experienced the same magnitude of pressure perturbation, but by different paths: the
978 sharply zoned crystal ascended near-instantaneously, while the diffusely zoned crystal
979 ascended continuously. Although both profiles represent $t \approx 0$ from a diffusion chronometry
980 standpoint, qualitative comparison of core to rim traverses clearly shows that the slowly
981 decompressed crystal will yield a longer timescale if the initial compositional profile is
982 assumed to be stepped. Slow, coupled diffusion of Na–Si and Ca–Al in plagioclase is an
983 extreme example of this phenomenon, but it illustrates our point, which is equally relevant to
984 decompression- and cooling-induced growth: any final diffusion profile is modulated by the
985 original kinetic profile of the growing crystal rim. The nature of this kinetic effect will
986 depend on the T-P-X-*t* path of the perturbation responsible for rim growth, and will not
987 necessarily be correlated with time.

Comparison of natural and experimental data

Decompression experiments provide a key means of referencing the groundmass textures of natural pyroclasts to magma ascent histories. At Mount St. Helens, the textures of pyroclasts produced by a series of increasingly pulsatory sub-Plinian to Vulcanian eruptions between 12 June and 16 Oct 1980 record a complex history of magma decompression and eruption (Cashman, 1988; 1992; Klug & Cashman, 1994; Cashman & McConnell, 2005; Muir *et al.,* 2012). Eruptions on 22 July and 7 August were particularly well observed and provide important constraints on eruption conditions (Hoblitt, 1986). Both were preceded by high rates of gas and ash emission; in July, this was followed by ~1 hour of short Vulcanian explosions and small dense pyroclastic flows caused by overpressure buildup beneath the edifice and disruption of the overlying lava dome (emplaced in June). The July eruption produced no lava dome, thus the August eruption lacked Vulcanian explosions but was preceded by 1.5 hours of fluctuating ash emissions through vent-filling debris. Both eruptions, then, comprised multiple short (~5 min) explosive events caused by rapid downward propagation of a decompression wave that unloaded and fragmented magma stored within the conduit. This was followed by slower refilling of the conduit with decompressed (but non-erupted) magma during repose intervals of hours. Post-eruptive conduit refilling produced visible lava domes after eruptions in June, August and October.

We can quantitatively compare textures of natural pyroclasts produced by these eruptions to our experimental samples using the parameters N_A and ϕ, which are not subject to errors involved in conversion of 2D data to 3D, and which together define the "crystallization regime" (e.g., Cashman *et al.,* 1999; Hammer *et al.,* 1999; Cashman & McConnell, 2005; Blundy & Cashman, 2008; Riker *et al.,* 2009; Brugger & Hammer, 2010*a*; Martel, 2012; Mollard *et al.,* 2012). The slopes of N_A–ϕ curves are inversely proportional to the average crystal size, such that groundmass textures characterized by high N_A at low ϕ (small average sizes) record nucleation-dominated crystallization, while increasing ϕ at near constant N_A (large average sizes) records growth-dominated crystallization. Our experimental samples define distinct N_A–ϕ trajectories that document increasing crystallization with decreasing quench pressure (Fig. 13a). Trajectories for CD experiments steepen with increasing decompression rate, illustrating the growing influence of nucleation at high dP/dt. CO_2-bearing experiments also define steeper crystallization paths than H_2O-saturated runs at the same decompression rate. The data for SSD experiments, in contrast, are time invariant;

these are shown as bands in N_A–ϕ space that represent the termini of curved paths taken during the first 24 hours of crystallization (Fig. 13b).

For context, data from select experimental studies are also displayed in Figures 13c and d. We restrict our comparison to isothermal decompressions of rhyolitic melts at temperatures similar to ours (850–880 °C) and consider only runs with comparable decompression paths: continuous or quasi-continuous decompressions quenched immediately at P_f (Brugger & Hammer, 2010*a*; Martel, 2012) or single-step decompressions followed by a finite dwell (Couch, 2003). Nonetheless, there are offsets between datasets not easily explained by the variables these studies intend to test. For example, our own runs have much lower N_A than those of Brugger & Hammer (2010*a*), despite similar d*P*/d*t* (as discussed above; Fig. 13c); the CD runs of Martel (2012) and Brugger & Hammer (2010*a*) have overlapping N_A and ϕ, despite generally lower d*P*/d*t* in the latter (Fig. 13c); and the SSD runs of Couch have lower N_A at a given ϕ compared to CD runs from the literature (Fig. 13d) – in our own (internally-consistent) dataset, the textures of CD and SSD runs overlap. These observations highlight the challenges of comparing experimental studies in which a large number of variables influence nucleation and growth kinetics. These include not only temperature, composition, decompression rate and path, but also the nature of the starting material (in particular superliquidus heating, which suppresses nucleation, e.g. Shea & Hammer, 2013) and, as our own experiments show, melt water content and the presence and distribution of pre-existing crystals. Strong similarities between our SSD data and those of Couch may reflect the fact that both studies use synthetic (superheated) starting material and contain a small population of crystals formed during the experimental anneal period.

Also shown in Figures 13a and b are data fields for three textural classes of natural pyroclasts from the summer 1980 eruptions of Mount St. Helens (as defined by Cashman & McConnell, 2005): (1) "LND" clasts with low number densities of prismatic plagioclase microlites; (2) "BML" clasts with bimodal plagioclase populations of larger, zoned prismatic microlites surrounded by smaller, acicular crystals; and (3) "HND" clasts containing high number densities of acicular, skeletal plagioclase microlites. Our experimental data overlap with the fields of LND and BML pyroclasts and can be used to provide additional constraints on the conditions of magma storage and ascent during this period.

LND pyroclasts have moderate crystallinities (~25%), low N_A and equant plagioclase morphologies (crystal axis ratios of 1:2:5), all of which suggest crystallization in a growth-dominated regime. Plagioclase phenocrysts in these clasts have melt inclusion H_2O contents

indicating pre-eruptive magma storage at 70–90 MPa (Cashman & McConnell, 2005), consistent with textural constraints provided by the SSD experiments (Fig. 13b; see also Couch *et al.,* 2003). It is important to note, however, that LND clasts bear strong textural similarities to experiments decompressed continuously at 1–10 MPa hr^{-1}, including zoned prismatic crystals with occasional hopper or swallowtail overgrowths, and rare smaller (i.e. newly nucleated) crystals. Slow, steady decompression is also consistent with the presence of coarse-grained breakdown rims on amphibole (Browne & Gardner, 2006). Thus, although we prefer an interpretation that involves rapid, syn-eruptive decompression of LND magma, possibly followed by ascent and annealing between eruptions, the textural data alone do not provide unambiguous confirmation of either pre-eruptive storage depths or residence times at shallow levels (provided shallow storage was sufficiently brief to prevent nucleation of a silica phase and/or diffusive H_2O loss from melt inclusions).

BML clasts, with two distinct microlite size classes, resemble the textures generated in single-step decompressions to shallow pressures (25–50 MPa, or ~1–2 km), followed by isobaric storage. This ascent path is consistent with evidence for amphibole breakdown and pervasive silica formation in both natural and experimental samples, and with melt inclusion volatile contents that suggest pre-eruptive magma storage at ~37 MPa (Cashman & McConnell, 2005). We note, however, an inconsistency in crystal habit – nucleated crystals in our SSD experiments are dominantly skeletal, while those in natural bimodal samples are equant to acicular with limited swallowtail or skeletal features (crystal axis ratios of 1:2:2 and 1:2:5; Cashman & McConnell, 2005). This discrepancy could reflect a difference in conditions at the onset of decompression, as our experimental decompressions started with a microlite population that is absent from low-density (microlite-free) pyroclasts from the summer 1980 eruptions (material presumably derived directly from an upper crustal storage region; e.g., Blundy & Cashman, 2005; Cashman & McConnell, 2005). For this reason, it seems likely that BML clasts experienced two stages of decompression, one producing the larger equant crystals (equivalent to LND clasts) and a second generating the smaller and more elongate crystals (e.g., Cashman & McConnell, 2005). Alternatively, it is possible that the smaller (nucleation-dominated) crystal population was generated by fluxing with CO_2-rich gas (see below).

HND pyroclasts have very high N_A and low ϕ; in this they represent an endmember of nucleation-dominated crystallization. As in other experimental studies, we were unable to replicate these textures. One possible reason is that our experiments extended only to 25

MPa; nucleation should continue with decompression to lower pressures (e.g., Martel, 2012). In view of our comparison of H_2O and H_2O–CO_2-saturated runs, however, and by analogy with the mixed-volatile vesiculation experiments of Mangan *et al.* (2004), we suggest that fidelity between natural and experimental datasets might be improved by further addition of CO_2. The water-rich conditions considered here may be insufficient to produce the very high number densities of the HND samples, but fluxing by more CO_2-rich vapor compositions, such as those proposed by Blundy *et al.* (2010) based on melt inclusion and matrix glass CO_2–H_2O trends of samples erupted during this period (XH_2O^{fl} <0.5), could have a more pronounced effect on feldspar nucleation. Elevated gas emissions observed elsewhere immediately after short (Vulcanian–sub-Plinian) explosions have been interpreted as gas release from rapid decompression of non-erupted magma (e.g., Edmonds *et al.,* 2003). Such rapid decompression of H_2O–CO_2 saturated magma to shallow depths at low $XH2O^{fl}$ could potentially generate textures in the HND field (consider extension of the 100 MPa hr^{-1} curve in Fig. 13, displaced to the left by additional CO_2). That these magmas did not all remain long in shallow storage is evidenced by low crystallinities (sometimes <30 vol%) and the absence of an Si-phase. Intra-eruptive gas fluxing may have enhanced rapid crystallization during the repose intervals between individual explosive events.

Absent from Figure 13 are microlite-free samples (the highly vesicular "VES" type), as well as holocrystalline samples ("HXT") that are interpreted as remnants of shallow domes or plugs. We can constrain minimum decompression rates for the VES-type pumice clasts to >100 MPa hr^{-1}, based on the observation that even our most rapidly decompressed runs contain crystals nucleated during decompression. Assuming VES magma was stored between ~200 and 125 MPa (e.g., Cashman & Blundy, 2013), this minimum rate corresponds to a decompression time of less than two hours, which is approximately the length of time separating the initial Vulcanian explosions/gas emissions from subsequent eruption column development – inferred by Hoblitt (1986) to represent the decompression time. Decompression rates as high as ~3600 MPa hr^{-1} have been estimated for the May 18, 1980 eruption from H_2O diffusion profiles in glass embayments in phenocrysts (Humphreys *et al.* 2008), although these rates are maxima due to the possibility of kinetic vesiculation delays.

Our comparison of natural and experimental samples highlights the detailed information that can be derived from experimentally contextualized analysis of pyroclast textures, as well as the sensitivity of quench pressures inferred from N_A–ϕ relationships to the ascent path. An important corollary of our interpretations relates to the distinction between

magma decompression and magma ascent. Magma ascent usually causes decompression (although gas exsolution may cause overpressures to develop, particularly beneath conduit plugs and lava domes). Decompression, however, does not require magma ascent. In fact, rapid downward-propagating decompression waves caused by plug disruption during Vulcanian eruptions (such as those at Mount St. Helens during the summer of 1980) commonly triggers decompression, and even fragmentation, of magma from deep within volcanic conduits. Decompression of non-erupted magma may also cause elevated gas loss from deeper within the system. Rapidly decompressed magma may then ascend slowly, re-filling the conduit during intra-eruptive (or post-eruptive) periods. Our experiments suggest that the textural signature of the initial rapid decompression event may be preserved in clast textures, even if subsequent magma ascent is slow – another caveat when using decompression experiments to interpret the history of erupted products. For this reason, it is important to use multiple petrologic indicators (i.e., phase equilibria, breakdown rims, habit, melt inclusion compositions) to develop a detailed history of magma decompression and eruption (e.g., Hammer *et al.* 1999; Cashman & McConnell, 2005).

CONCLUSIONS

Recent experimental studies suggest that decompression path, in addition to decompression rate, plays a key role in modulating the development of crystal textures. We have undertaken a series of decompression experiments designed to assess the effect of degassing path on progressive crystallization of Mount St. Helens rhyodacite, simulating decompression along varied PH_2O–t trajectories (continuous versus single-step decompression and H_2O- versus H_2O–CO_2-saturated ascent). Quantitative textural data (plagioclase abundance, number density, and size) have been used to calculate time-averaged nucleation and growth rates for experimentally decompressed samples. A key finding of our work is that nucleation rates are higher in H_2O-CO_2 saturated (compared to H_2O-saturated) runs, presumably due to lower initial melt water contents, which facilitate feldspar nucleation during the experimental equilibration period.. These early-formed textural distinctions are most noticeable at low undercoolings and persist to low pressures, underscoring the importance of initial decompression conditions in controlling subsequent textural development in natural systems. Additionally, our data underline the sensitivity of instantaneous nucleation and growth rates to time. Distinguishing instantaneous from apparent (time-averaged) rates is important for interpreting crystal size distributions, often inferred to form at constant growth rates. Finally, our runs show that, at a wide range of experimental conditions, growth on pre-existing

crystals represents a significant proportion of the additional crystallization due to decompression (25–50%). The presence of crystals prior to the onset of decompression may modulate magmatic textures by suppressing feldspar nucleation relative to growth.

Our experimental data provide a context for interpreting the textures of natural pyroclasts. Importantly, the phase assemblage itself is a dynamic variable that can be used in conjunction with sample textures to infer eruptive conditions. Comparison of N_A–ϕ relationships in natural and experimental datasets from Mount St. Helens support a model of multiple magma storage depths during this period (e.g., Cashman & McConnell 2005), whereby variably degassed and crystallized magmas stored in the shallow plumbing system (1–2 km depth) are erupted alongside magmas sourced from a deeper storage region (~6–8 km). N_A–ϕ trends of CD and SSD experiments overlap, stressing that these two parameters do not uniquely define the magma closure pressure.

ACKNOWLEDGMENTS

We are grateful to Dana Johnston and David Senkovich at the University of Oregon for allowing us to use their experimental facilities and providing technical guidance throughout. We thank Richard Brooker and Carrie Brugger for helpful discussions on experimental technique. Thanks also to Stuart Kearns and Ben Buse for assistance with the University of Bristol EPMA and SEM facilities.

FUNDING

This work was supported by a University of Bristol Postgraduate Research Scholarship to JMR; an AXA Research Chair in Volcanology to KVC; a Royal Society University Research Fellowship to ACR; and European Research Council Advanced Grant “CRITMAG” to JDB.

REFERENCES

Abràmoff, M., Magalhães, P. & Ram, S. (2004). Image processing with ImageJ. *Biophotonics International* **11**, 36–42.

Anderson, A. (1984). Probable relations between plagioclase zoning and magma dynamics, Fuego Volcano, Guatemala. *American Mineralogist* **69**, 660–676.

Armienti, P., Pareschi, M., Innocenti, F. & Pompilio, M. (1994). Effects of magma storage and ascent on the kinetics of crystal growth. *Contributions to Mineralogy and Petrology* **115**, 402–414.

Arzilli, F. & Carroll, M. (2013). Crystallization kinetics of alkali feldspars in cooling and decompression-induced crystallization experiments in trachytic melt. *Contributions to Mineralogy and Petrology* **166**, 1011–1027.

Berlo, K., Blundy, J., Turner, S. & Hawkesworth, C. (2007). Textural and chemical variation in plagioclase phenocrysts from the 1980 eruptions of Mount St. Helens, USA. *Contributions to Mineralogy and Petrology* **154**, 291–308.

Bindeman, I. (2003). Crystal sizes in evolving silicic magma chambers. *Geology* **31**, 367–370.

Blundy, J. & Cashman, K. (2001). Ascent-driven crystallization of dacite magmas at Mount St. Helens, 1980–1986. *Contributions to Mineralogy and Petrology* **140**, 631–650.

Blundy, J. & Cashman, K. (2005). Rapid decompression-driven crystallization recorded by melt inclusions from Mount St. Helens volcano. *Geology* **33**, 793–796.

Blundy, J. & Cashman, K. (2008). *Petrologic reconstruction of magmatic system variables and processes.* In: Putirka, K. & Tepley, F. (eds.) *Minerals, Inclusions, and Volcanic Processes.* Reviews in Mineralogy and Geochemistry **69**, 179–239.

Blundy, J., Cashman, K. & Berlo, K. (2008). *Evolving magma storage conditions beneath Mount St. Helens inferred from chemical variations in melt inclusions from the 1980– 1986 and current (2004–2006) eruptions.* In: Sherrod, D., Scott, W. & Stauffer, P. (eds.) *A Volcano Rekindled: The Renewed Eruption of Mount St. Helens, 2004–2006.* U.S. Geological Survey Professional Paper **1750**, 755–790.

Blundy, J., Cashman, K., Rust, A. & Witham, F. (2010). A case for CO_2-rich arc magmas. *Earth and Planetary Science Letters* **290**, 289–301.

Boyce, J. & Hervig, R. (2008). Magmatic degassing histories from apatite volatile stratigraphy. *Geology* **36**, 63–66.

Browne, B. & Gardner, J. (2006). The influence of magma ascent path on the texture, mineralogy, and formation of hornblende reaction rims. *Earth and Planetary Science Letters* **246**, 161–176.

Brugger, C. & Hammer, J. (2010*a*). Crystallization kinetics in continuous decompression experiments: Implications for interpreting natural magma ascent processes. *Journal of Petrology* **51**, 1941–1965.

Brugger, C. & Hammer, J. (2010*b*). Crystal size distribution analysis of plagioclase in experimentally decompressed hydrous rhyodacite magma. *Earth and Planetary Science Letters* **300**, 246–254.

Casadevall, T., Johnston, D., Harris, D., Rose, W., Malinconico, L., Stoiber, R., Bornhorst, T., Williams, S., Woodruff, L. & Thompson, J. (1981). *SO_2 emission rates at Mount St. Helens from March 29 through December, 1980.* In: Lipman, P. & Mullineaux, D. (eds.) *The 1980 eruptions of Mount St. Helens, Washington.* U.S. Geological Survey Professional Paper **1250**, 193–200.

Cashman, K. & Taggart, J. (1983). Petrologic monitoring of 1981 and 1982 eruptive products from Mount St. Helens. *Science* **221**, 1385–1387.

Cashman, K. (1988). Crystallization of Mount St. Helens 1980–1986 dacite: A quantitative textural approach. *Bulletin of Volcanology* **50**, 194–209.

Cashman, K. & Marsh, B. (1988). Crystal size distribution (CSD) in rocks and the kinetics and dynamics of crystallization II: Makaopuhi lava lake. *Contributions to Mineralogy and Petrology* **99**, 292–305.

Cashman, K. & Ferry, J. (1988). Crystal size distribution (CSD) in rocks and the kinetics and dynamics of crystallization III: Metamorphic crystallization. *Contributions to Mineralogy*

and Petrology **99**, 401–415.

Cashman, K. (1992). Groundmass crystallization of Mount St. Helens dacite, 1980–1986: A tool for interpreting shallow magmatic processes. *Contributions to Mineralogy and Petrology* **109**, 431–449.

Cashman, K. & Hoblitt, R. (1994). Magmatic precursors to the 18 May 1980 eruption of Mount St. Helens, USA. *Geology* **32**, 141–144.

Cashman, K., Thornber, C. & Kauahikaua, J. (1999). Cooling and crystallization of lava in open channels, and the transition of pāhoehoe lava to ʻaʻā. *Bulletin of Volcanology*, **61**, 306–323.

Cashman, K. & McConnell, S. (2005). Multiple levels of magma storage during the 1980 summer eruptions of Mount St. Helens, WA. *Bulletin of Volcanology* **68**, 57–75.

Cashman, K., Thornber, C. & Pallister, J. (2008). *From dome to dust: shallow crystallization and fragmentation of conduit magma during the 2004-2006 dome extrusion of Mount St. Helens, Washington.* In: Sherrod, D., Scott, W. & Stauffer, P. (eds.) *A Volcano Rekindled: The Renewed Eruption of Mount St. Helens, 2004–2006.* U.S. Geological Survey Professional Paper **1750**, 387–413.

Cashman, K. & Blundy, J. (2013). Petrological cannibalism: The chemical and textural consequences of incremental magma body growth. *Contributions to Mineralogy and Petrology* **166**, 703–729.

Castro, J., Cashman, K. & Manga, M. (2004). A technique for measuring 3D crystal size distributions of prismatic microlites in obsidian. *American Mineralogist* **88**, 1230–1240.

Cheng, H. & Lemlich, R. (1983). Errors in the measurement of bubble size distribution in foam. *Industrial & Engineering Chemistry Fundamentals* **22**, 105–109.

Christiansen, R. & Peterson, D. (1981). *Chronology of the 1980 eruptive activity.* In: Lipman, P. & Mullineaux, D. (eds.) *The 1980 eruptions of Mount St. Helens, Washington.* U.S.

Geological Survey Professional Paper **1250**, 17–30.

Cichy, S., Botcharnikov, R., Holtz, F. & Behrens, H. (2011). Vesiculation and microlite crystallization induced by decompression: A case study of the 1991–1995 Mt. Unzen eruption (Japan). *Journal of Petrology* **52**, 1469–1492.

Costa, F., Dohmen, R. & Chakraborty, S. (2008). *Time scales of magmatic processes from modeling the zoning patterns of crystals.* In: Putirka, K. & Tepley, F. (eds.) *Minerals, Inclusions, and Volcanic Processes.* Reviews in Mineralogy and Geochemistry **69**, 545–594.

Couch, S., Sparks, R. & Carroll, M. (2003). The kinetics of degassing-induced crystallization at Soufriere Hills Volcano, Montserrat. *Journal of Petrology* **44**, 1477–1502.

Davis, M., Ihinger, P. & Lasaga, A. (1997). Influence of water on nucleation kinetics in silicate melt. *Journal of Non-Crystalline Solids* **219**, 62–69.

DeHoff, R. & Rhines, F. (1968). *Quantitative Microscopy.* McGraw-Hill, New York.

Donaldson, C. (1976). An experimental investigation of olivine morphology. *Contributions to Mineralogy and Petrology* **57**, 187–213.

Dowty, E. (1980). *Crystal growth and nucleation theory and the numerical simulation of igneous crystallization.* In: Hargraves, R. (ed.) *The Physics of Magmatic Processes.* Princeton University Press, 419–485.

Druitt, T., Costa, F., Deloule, E., Dungan, M. & Scaillet, B. (2012). Decadal to monthly timescales of magma transfer and reservoir growth at a caldera volcano. *Nature* **482**, 77–80.

Ebadi, A. & Johannes, W. (1991). Beginning of melting and composition of first melts in the system Qz–Ab–Or– H_2O – CO_2. *Contributions to Mineralogy and Petrology* **106**, 286–295.

Edmonds, M., Oppenheimer, C., Pyle, D., Herd, R. & Thompson, G. (2003). SO_2 emissions from Soufriere Hills Volcano and their relationship to conduit permeability, hydrothermal

1322 interaction and degassing regime. *Journal of Volcanology and Geothermal Research* **124**,
1323 23–43.
1324
1325 Faure, F., Trolliard, G., Nicollet, C. & Montel, J.-M. (2003). A developmental model of
1326 olivine morphology as a function of the cooling rate and the degree of undercooling.
1327 *Contributions to Mineralogy and Petrology* **145**, 251–263.
1328
1329 Fenn, P. (1977). The nucleation and growth of alkali feldspar from hydrous melts. *Canadian*
1330 *Mineralogist* **15**, 135–161.
1331
1332 Fokin, V., Kalinina, A. & Filipovich, V. (1981). Nucleation in silicate glasses and effect of
1333 preliminary heat treatment on it. *Journal of Crystal Growth* **52**, 115–121.
1334
1335 Fokin, V., Zanotto, E., Yuritsyn, N. & Schmelzer, J. W. (2006). Homogeneous crystal
1336 nucleation in silicate glasses: a 40 years perspective. *Journal of Non-Crystalline Solids* **352**,
1337 2681–2714.
1338
1339 Gardner, J., Rutherford, M., Carey, S. & Sigurdsson, H. (1995). Experimental constraints on
1340 pre-eruptive water contents and changing magma storage prior to explosive eruptions of
1341 Mount St. Helens volcano. *Bulletin of Volcanology* **57**, 1–17.
1342
1343 Gardner, J., Hilton, M. & Carroll, M. (1999). Experimental constraints on degassing of
1344 magma: isothermal bubble growth during continuous decompression from high pressure.
1345 *Earth and Planetary Science Letters* **168**, 201–218.
1346
1347 Geschwind, C. & Rutherford, M. (1995). Crystallization of microlites during magma ascent:
1348 The fluid mechanics of 1980–1986 eruptions at Mount St. Helens. *Bulletin of Volcanology*
1349 **57**, 356–370.
1350
1351 Grove, T. & Bence, A. (1979). Crystallization kinetics in a multiply saturated basalt magma:
1352 An experimental study of Luna 24 ferrobasalt. *Proceedings of the 10th Lunar and Planetary*
1353 *Science Conference*, 439–478.
1354
1355 Hammer, J. (2006). Influence of fO_2 and cooling rate on the kinetics and energetics of Fe-rich

basalt crystallization. *Earth and Planetary Science Letters* **248**, 618–637.

Hammer, J., Cashman, K., Hoblitt, R. & Newman, S. (1999). Degassing and microlite crystallization during pre-climactic events of the 1991 eruption of Mt. Pinatubo, Philippines. *Bulletin of Volcanology* **60**, 355–380.

Hammer, J. & Rutherford, M. (2002). An experimental study of the kinetics of decompression-induced crystallization in silicic melt. *Journal of Geophysical Research* **107**, 1–23.

Hammer, J. (2008). *Experimental studies of the kinetics and energetics of magma crystallization.* In: Putirka, K. & Tepley, F. (eds.) *Minerals, Inclusions, and Volcanic Processes.* Reviews in Mineralogy and Geochemistry **69**, 9–59.

Higgins, M. (1998). Origin of anorthosite by textural coarsening: Quantitative measurements of a natural sequence of textural development. *Journal of Petrology* **39**, 1307– 1323.

Higgins, M. (2000). Measurement of crystal size distributions. *American Mineralogist* **85**, 1105–1116.

Higgins, M. (2006). *Quantitative Textural Measurements in Igneous and Metamorphic Petrology.* Cambridge University Press, Cambridge.

Higgins, M. & Roberge, J. (2003). Crystal size distribution of plagioclase and amphibole from Soufrière Hills Volcano, Montserrat: evidence for dynamic crystallization– textural coarsening cycles. *Journal of Petrology* **44**, 1401–1411.

Hoblitt, R. (1986). *Observations of the Eruptions of July 22 and August 7, 1980, at Mount St. Helens, Washington.* U.S. Government Printing Office, Washington.

Humphreys, M., Kearns, S. & Blundy, J. (2006). SIMS investigation of electron-beam damage to hydrous, rhyolitic glasses: Implications for melt inclusion analysis. *American Mineralogist* **91**, 667–679.

1390 Humphreys, M., Menand, T., Blundy, J., & Klimm, K. (2008). Magma ascent rates in
1391 explosive eruptions: Constraints from H_2O diffusion in melt inclusions. *Earth and Planetary*
1392 *Science Letters* **270**, 25–40.
1393
1394 Humphreys, M., Edmonds, M., Plail, M., Barclay, J., Parkes, D. & Christopher, T. (2013). A
1395 new method to quantify the real supply of mafic components to a hybrid andesite.
1396 *Contributions to Mineralogy and Petrology* **165**, 191–215.
1397
1398 Innocenti, S., Andreastuti, S., Furman, T., del Marmol, M.-A. & Voight, B. (2013). The pre-
1399 eruption conditions for explosive eruptions at Merapi Volcano as revealed by crystal texture
1400 and mineralogy. *Journal of Volcanology and Geothermal Research* **261**, 69–86.
1401
1402 James, P. (1985). Kinetics of crystal nucleation in silicate glasses. *Journal of Non-Crystalline*
1403 *Solids* **73**, 517–540.
1404
1405 Johnston, A. & Senkovich, D. (2007). Rapid quench cold-seal apparatus with computer
1406 controlled pressure and temperature cycling. *AGU Fall Meeting Abstracts.*
1407
1408 Kirkpatrick, R. (1981). *Kinetics of crystallization of igneous rocks.* In: Lasaga, A. &
1409 Kirkpatrick, R. (eds.) *Kinetics of Geochemical Processes.* Reviews in Mineralogy **8**, 321–
1410 397.
1411
1412 Klug, C. & Cashman, K. (1994). Vesiculation of May 18, 1980, Mount St. Helens magma.
1413 *Geology* **22**, 468– 472.
1414
1415 Klug, C., Cashman, K. & Bacon, C. (2002). Structure and physical characteristics of pumice
1416 from the climactic eruption of Mount Mazama (Crater Lake), Oregon. *Bulletin of*
1417 *Volcanology* **64**, 486–501.
1418
1419 Lofgren, G. (1974). An experimental study of plagioclase crystal morphology: Isothermal
1420 crystallization. *American Journal of Science* **274**, 243–273.
1421
1422 Lofgren, G. (1980). *Experimental studies on the dynamic crystallization of silicate melts.* In:
1423 Hargraves, R. (ed.) *The Physics of Magmatic Processes.* Princeton University Press,

Princeton, 487–551.

Luhr, J. & Carmichael, I. (1980). The Colima Volcanic Complex, Mexico. *Contributions to Mineralogy and Petrology* **71**, 343–372.

Luhr, J. & Carmichael, I. (1982). The Colima Volcanic Complex, Mexico: III. *Contributions to Mineralogy and Petrology* **80**, 262–275.

Mangan, M., Mastin, L. & Sisson, T. (2004). Gas evolution in eruptive conduits: Combining insights from high temperature and pressure decompression experiments with steady state flow modeling. *Journal of Volcanology and Geothermal Research* **129**, 23–36.

Marsh, B. (1988). Crystal size distribution (CSD) in rocks and the kinetics and dynamics of crystallization I: Theory. *Contributions to Mineralogy and Petrology* **99**, 277–291.

Martel, C. & Schmidt, B. (2003). Decompression experiments as an insight into ascent rates of silicic magmas. *Contributions to Mineralogy and Petrology* **144**, 397–415.

Martel, C. (2012). Eruption dynamics inferred from microlite crystallization experiments: Application to plinian and dome-forming eruptions of Mt. Pelee (Martinique, Lesser Antilles). *Journal of Petrology* **53**, 699–725.

Melnik, O. & Sparks, R. (2005). Controls on conduit magma flow dynamics during lava dome building eruptions. *Journal of Geophysical Research* **110**, 1–21.

Mollard, E., Martel, C. & Bourdier, J. (2012). Decompression-induced crystallization in hydrated silica-rich melts: Empirical models of experimental plagioclase nucleation and growth kinetics. *Journal of Petrology* **53**, 1743–1766.

Morgan, D., Blake, S., Rogers, N., DeVivo, B., Rolandi, G., Macdonald, R. & Hawkesworth, C. (2004). Time scales of crystal residence and magma chamber volume from modeling of diffusion profiles in phenocrysts: Vesuvius 1944. *Earth and Planetary Science Letters* **222**, 933–946.

1458 Morgan, D. & Jerram, D. (2006). On estimating crystal shape for crystal size distribution
1459 analysis. *Journal of Volcanology and Geothermal Research* **154**, 1–7.
1460
1461 Morgan, D., Blake, S., Rogers, N., De Vivo, B., Rolandi, G. & Davidson, J. (2006). Magma
1462 chamber recharge at Vesuvius in the century prior to the eruption of A.D. 79. *Geology* **34**,
1463 845–848.
1464
1465 Morgan, D. & Costa, F. (2010). *Timescales of Magmatic Processes.* In: Dosseto, A. Turner,
1466 S. & Van-Orman, J. (eds.) *Timescales of Magmatic Processes*. Wiley-Blackwell.
1467
1468 Mourtada-Bonnefoi, C. & Laporte, D. (1999). Experimental study of homogeneous bubble
1469 nucleation in rhyolitic magmas. *Geophysical Research Letters* **26**, 3505–3508.
1470
1471 Muir, D., Blundy, J. & Rust, A. (2012). Multiphase petrography of volcanic rocks using
1472 element maps: A method applied to Mount St. Helens, 1980–2005. *Bulletin of Volcanology*
1473 **74**, 1101–1120.
1474
1475 Muncill, G. & Lasaga, A. (1988). Crystal-growth kinetics of plagioclase in igneous systems:
1476 Isothermal H_2O-saturated experiments and extension of a growth model to complex silicate
1477 melts. *American Mineralogist* **73**, 982–992.
1478
1479 Peterson, T. (1996). A refined technique for measuring crystal size distributions in thin
1480 section. *Contributions to Mineralogy and Petrology* **124**, 395–405.
1481
1482 Pichavant, M., Martel, C., Bourdier, J. & Scaillet, B. (2002). Physical conditions, structure,
1483 and dynamics of a zoned magma chamber: Mount Pelee (Martinique, Lesser Antilles Arc.
1484 *Journal of Geophysical Research* **107**, 1–29.
1485
1486 Pichavant, M., Costa, F., Burgisser, A., Scaillet, B., Martel, C. & Poussineau, S. (2007).
1487 Equilibration scales in silicic to intermediate magmas – Implications for experimental
1488 studies. *Journal of Petrology* **48**, 1955–1972.
1489
1490 Piochi, M., Mastrolorenzo, G. & Pappalardo, L. (2005). Magma ascent and eruptive
1491 processes from textural and compositional features of Monte Nuovo pyroclastic products,

Campi Flegrei, Italy. *Bulletin of Volcanology* **67**, 663–678.

Pownceby, M. & O'Neill, H. (1994). Thermodynamic data from redox reactions at high temperatures. III. Activity-composition relations in Ni–Pd alloys from EMF measurements at 850–1250 K, and calibration of the NiO+Ni−Pd assemblage as a redox sensor. *Contributions to Mineralogy and Petrology* **116**, 327–339.

Pupier, E., Duchene, S. & Toplis, M. (2008). Experimental quantification of plagioclase crystal size distribution during cooling of a basaltic liquid. *Contributions to Mineralogy and Petrology* **155**, 555–570.

Putirka, K.D. (2005). Igneous thermometers and barometers based on plagioclase + liquid equilibria: Tests of some existing models and new calibrations. *American Mineralogist* **90**, 336–346.

Randolph, A. & Larson, M. (1971). *Theory of Particulate Processes: Analysis and Techniques of Continuous Crystallization.* Academic Press, New York.

Riker, J., Cashman, K., Kauahikaua, J. & Montierth, C. (2009). The length of channelized lava flows: Insight from the 1859 eruption of Mauna Loa Volcano, Hawai'i. *Journal of Volcanology and Geothermal Research* **183**, 139–156.

Riker, J., Blundy J., Rust, A., Botcharnikov, R. & M. Humphreys (in press). Experimental phase equilibria of a Mount St. Helens rhyodacite: A framework for interpreting crystallization paths in degassing silicic magmas. *Contributions to Mineralogy and Petrology***,** doi: 10.1007/s00410-015-1150-7.

Rust, A. & Cashman, K. (2011). Permeability controls on expansion and size distributions of pyroclasts. *Journal of Geophysical Research* **116**, 1–17.

Rutherford, M., Sigurdsson, H., Carey, S. & Davis, A. (1985). The May 18, 1980, eruption of Mount St. Helens 1. Melt composition and experimental phase equilibria. *Journal of Geophysical Research* **90**, 2929–2947.

Rutherford, M. & Devine, J. (1988). The May 18, 1980, eruption of Mount St. Helens 3. Stability and chemistry of amphibole in the magma chamber. *Journal of Geophysical Research* **93**, 11949–11959.

Rutherford, M. & Hill, P. (1993). Magma ascent rates from amphibole breakdown – An experimental study applied to the 1980-1986 Mount St. Helens eruptions. *Journal of Geophysical Research* **98**, 19667–19685.

Rutherford, M. & Devine, J. (2008). *Magmatic conditions and processes in the storage zone of the 2004–2006 Mount St. Helens dacite.* In: Sherrod, D., Scott, W. & Stauffer, P. (eds.) *A Volcano Rekindled: The Renewed Eruption of Mount St. Helens, 2004–2006.* U.S. Geological Survey Professional Paper **1750**, 703–725.

Rutherford, M. (2008). *Magma ascent rates.* In: Putirka, K. & Tepley, F. (eds.) *Minerals, Inclusions, and Volcanic Processes.* Reviews in Mineralogy and Geochemistry **69**, 241– 271.

Sahagian, D. & Proussevitch, A. (1998). 3D particle size distributions from 2D observations: Stereology for natural applications. *Journal of Volcanology and Geothermal Research* **84**, 173–196.

Salisbury, M., Bohrson, W., Clynne, M., Ramos, F. & Hoskin, P. (2008). Multiple plagioclase crystal populations identified by crystal size distribution and in situ chemical data: Implications for timescales of magma chamber processes associated with the 1915 eruption of Lassen Peak, CA. *Journal of Petrology* **49**, 1755–1780.

Sato, K., Kashima, K. & Sunagawa, I. (1981). Measurements of nucleation rates and real growth rates of plagioclase in a solution of basaltic composition. *Journal of the Japanese Association for Mineralogy, Petrology, and Economic Geology* **76**, 294–307.

Saunders, K., Blundy, J., Dohmen, R. & Cashman, K. (2012). Linking petrology and seismology at an active volcano. *Science* **336**, 1023–1027.

Scaillet, B. & Evans, B. (1999). The 15 June 1991 eruption of Mount Pinatubo I. Phase equilibria and pre-eruption P–T–fO_2–fH_2O conditions of the dacite magma. *Journal of Petrology* **40**, 381–411.

Shea, T., Houghton, B., Gurioli, L., Cashman, K., Hammer, J. & Hobden, B. (2010). Textural studies of vesicles in volcanic rocks: An integrated methodology. *Journal of Volcanology and Geothermal Research* **190**, 271–289.

Shea, T. & Hammer, J. (2013). Kinetics of cooling and decompression-induced crystallization in hydrous mafic-intermediate magmas. *Journal of Volcanology and Geothermal Research* **260**, 127–145.

Sisson, T., Ratajeski, K., Hankins, W. & Glazner, A. (2005). Voluminous granitic magmas from common basaltic sources. *Contributions to Mineralogy and Petrology* **148**, 635–661.

Smith, D. & Leeman, W. (1987). Petrogenesis of Mount St. Helens dacitic magmas. *Journal of Geophysical Research* **92**, 10313–10334.

Streck, M., Broderick, C., Thornber, C., Clynee, M. & Pallister, J. (2008). *Plagioclase populations and zoning in dacite of the 2004–2005 Mount St. Helens eruption: Constraints for magma origin and dynamics.* In: Sherrod, D., Scott, W. & Stauffer, P. (eds.) *A Volcano Rekindled: The Renewed Eruption of Mount St. Helens, 2004–2006.* U.S. Geological Survey Professional Paper **1750**, 791–808.

Sunagawa, I. (1981). Characteristics of crystal growth in nature as seen from the morphology of mineral crystals. *Bulletin of Mineralogy* **104**, 81–87.

Suzuki, Y., Gardner, J. & Larsen, J. (2007). Experimental constraints on syneruptive magma ascent related to the phreatomagmatic phase of the 2000 AD eruption of Usu volcano, Japan. *Bulletin of Volcanology* **69**, 423–444.

Swanson, S. (1977). Relation of nucleation and crystal growth rate to the development of granitic textures. *American Mineralogist* **62**, 966–978.

1592 Szramek, L., Gardner, J. & Larsen, J. (2006). Degassing and microlite crystallization of
1593 basaltic andesite magma erupting at Arenal volcano, Costa Rica. *Journal of Volcanology and*
1594 *Geothermal Research* **157**, 182–201.
1595
1596 Tamic, N., Behrens, H. & Holtz, F. (2001). The solubility of H_2O and CO_2 in rhyolitic melts
1597 in equilibrium with a mixed CO_2–H_2O fluid phase. *Chemical Geology* **174**, 333–347.
1598
1599 Taylor, J., Wall, V. & Pownceby, M. (1992). The calibration and application of accurate
1600 redox sensors. *American Mineralogist* **77**, 284–295.
1601
1602 Thornber, C., Pallister, J., Lowers, H., Rowe, M., Mandeville, C. & Meeker, G. (2008).
1603 *Chemistry, mineralogy, and petrology of amphibole in Mount St. Helens 2004-2006 dacite.*
1604 In: Sherrod, D., Scott, W. & Stauffer, P. (eds.) *A Volcano Rekindled: The Renewed Eruption*
1605 *of Mount St. Helens, 2004–2006.* U.S. Geological Survey Professional Paper **1750**, 727–754.
1606
1607 Toramaru, A., (2008). MND (microlite number density) water exsolution rate meter. *Journal*
1608 *of Volcanology and Geothermal Research* **175**, 156–167.
1609
1610 Tuttle, O. & Bowen, N. (1958). *Origin of Granite in the Light of Experimental Studies in the*
1611 *System* $NaAlSi_3O_8$–$KAlSi_3O_8$–SiO_2– H_2O. Geological Society of America.
1612
1613 Underwood, E. (1970). *Quantitative Stereology.* Addison-Wesley, Reading.
1614
1615 Yoder, H. (1965). Diopside–anorthite–water at five and ten kilobars and its bearing on
1616 explosive volcanism. *Carnegie Institute of Washington Yearbook* **64**, 82–89.
1617

Figure 1: Equilibrium P– XH_2O^{fl} phase diagram for Sugar Bowl rhyodacite at 885 °C. Open and closed circles show H_2O- and H_2O–CO_2-saturated experiments, respectively. Final fluid compositions of CO_2-bearing charges were determined by gravimetry; initial fluid compositions were $XH_2O^{fl} \approx 0.8$. Solid lines are phase boundaries (plag: plagioclase, opx: orthopyroxene, amph: amphibole, ox: Fe–Ti oxides). Dashed lines contour measured melt water contents. Solidus after Ebadi & Johannes (1991).

Figure 2: BSE images of equilibrium reference samples, showing abundance and textures of plagioclase crystals (light grey) at each fluid composition prior to decompression. Phases present are labeled: plagioclase (plag), amphibole (amph), orthopyroxene (opx), Fe-Ti oxides (ox), and vesicles (vesc). Large white circles in (a) are vesicles infilled with Au coating. Reference samples were equilibrated at 200 MPa and 885 °C; (a) run DSB6 with XH_2O^{fl} = 1.0, equilibrated for 72 hours, (b) run PSB39 with XH_2O^{fl} = 0.8, equilibrated for 168 hours. Plagioclase abundance is higher in (b) due to lower melt water content of charge.

Figure 3: Representative BSE images of experimentally decompressed samples. Same scale in all images. Light grey crystals are plagioclase, high-contrast phases are Fe–Ti oxides, orthopyroxene, and/or amphibole, black areas are vesicles. Vertical image stacks are (a) pure-H_2O runs decompressed at 1 MPa hr^{-1}; (b) pure- H_2O runs decompressed at 10 MPa hr^{-1}; (c) H_2O–CO_2 runs decompressed at 1 MPa hr^{-1}; (d) H_2O–CO_2 runs decompressed at 10 MPa hr^{-1}; (e) SSD with t_{dw} = 24 hours; (f) SSD with t_{dw} = 168 hours. Quench pressure P_f decreases from top to the bottom.

Figure 4: Plagioclase anorthite contents and glass K_2O contents of experimental run products as a function of quench pressure. Bars show the range of plagioclase compositions in each sample; cross bars show mean of analyzed values. Orange symbols and lines give equilibrium values from a corresponding set of phase equilibria experiments (Riker *et al.* in press); equilibrium plagioclase compositions at $XH2O^{fl}$ = 0.8 are inferred from the An–H_2O–P relationships of these runs. Equilibrium glass K_2O contents for runs at $XH2O^{fl}$ = 0.8 are not shown, as we have no corresponding equilibrium dataset at this fluid composition.

Figure 5: Plagioclase volume fraction (ϕ), areal number density (N_A), and average size (S_N) versus quench pressure for (a) CD at XH_2O^{fl} = 1.0, (b) CD at XH_2O^{fl} = 0.8, and (c) SSD. (d)

shows ϕ, N_A, and S_N versus t_{dw} at final pressure for SSD; lines connect samples with identical P_f. Plagioclase N_A corrected for pre-existing crystals using equilibrium reference samples; ϕ and S_N include contribution from pre-existing plagioclase. Grey lines in ϕ–P_f plots are estimated equilibrium curves based on phase equilibria experiments in the pure-H_2O system (small grey dots; Riker *et al.*, in press). Error bars show 1σ variance of multiple analyzed images, or sub-sampled crystal populations within a single image.

Figure 6: Time-integrated plagioclase growth (G) and nucleation rates (I) versus quench pressure. Rates have been corrected for the presence of pre-existing crystals as discussed in text. Error bars give the 1σ variability within each sample. Arrows show the direction of progressive decompression.

Figure 7: Crystal size distributions of experimentally decompressed samples calculated using CSDCorrections (Higgins, 2000). Experiments are separated by decompression rate (CD at 1, 10, and 100 MPa hr^{-1}, or SSD) and fluid composition (XH_2O^{fl} = 1.0 or 0.8). All CSDs have concave-upward forms that we attribute to the combined effect of crystals formed during equilibration and nucleated during decompression; curvature changes with decompression rate, path, and fluid composition.

Figure 8: Comparison of CSD- and batch-derived (a) growth rates (G) and (b) nucleation rates (I) for plagioclase crystals formed during decompression. Regression fits used in CSD calculations are given in Table 4. CSD-derived growth rates are consistently lower than batch-derived rates; CSD-derived nucleation rates are slightly higher.

Figure 9: Time variance of kinetic parameters for decompression crystallization derived from experimental data. (a) Batch-derived nucleation rates for SSD at P_f = 25 MPa (open squares, black dashed lines) and CD at P_f = 25 MPa and XH_2O^{fl} = 1.0 (open circles, red dotted lines). Curves are schematic, lines are apparent (time-averaged) nucleation rates labeled as number $mm^{-2}\,hr^{-1}$; brackets are rates in number $mm^{-3}s^{-1}$ (lines are extrapolated beyond the data for clarity only). (b) Batch-derived growth rates for SSD at P_f = 25 MPa (open squares, black dashed lines), P_f = 50 MPa (gray squares, gray dashed lines), P_f = 100 MPa (black squares, solid black lines) and CD at P_f = 25 MPa and XH_2O^{fl} = 1.0 (circles, red dotted lines). Curves are schematic; lines are apparent (time-averaged) growth rates labeled

as mm $s^{-1} \times 10^{-8}$. (c) Variation in apparent G of all experiments as function of crystallization time. Short duration (≤ 24 hour) experiments form a trend that is distinct from long duration (≥ 100 hour) experiments. (d) Total crystallinity as measure of chemical disequilibrium: $\Delta\phi = \phi^{eq} - \phi$, where ϕ^{eq} is equilibrium crystallinity at $P = P_f$ (Brugger & Hammer, 2010*a*). X-axis offset for clarity. Symbols are as above, with gray circles CD at P_f = 50 MPa and black circles CD at P_f = 100 MPa (both at $XH_2O^{fl} = 1.0$). All samples overlap at origin, where $\phi = \phi^{eq}$. Dashed lines show inferred trends for SSD runs, assuming a crystallization lag longer than the timescale of decompression.

Figure 10: Size histograms (as area fraction) of all plagioclase crystals in representative samples: (a) DSB6, (b) DSB39, (c) DSB16, (d) DSB19, (e) DSB26, (f) DSB18, (g) DSB23, (h) DSB13. Crystals formed during anneal period (grey shading) identified using plagioclase N_A in equilibrium reference samples, assuming largest crystals in decompressed samples formed during equilibration. Total crystal volume fraction (ϕ) and the volume fraction represented by pre-existing cores of anneal crystals (ϕ^{eq}) are labeled. Additional growth of pre-existing crystals constitutes ~25–50% decompression crystallization.

Figure 11: Comparison of phenocryst abundance in paired pumice (open symbols) and lava (filled symbols) samples. MSH: Mount St. Helens (1980 pumice and lava [grey] from Cashman & Taggart, 1983; 2004–6 spine data [black] from Cashman *et al.,* 2008); COL: Colima (data from Luhr & Carmichael, 1980; 1982); MER: Merapi (data from Innocenti *et al.,* 2013); MP: Mount Pelee (data from Pichavant *et al.,* 2002, maximum and minimum only).

Figure 12: Compositional zoning profiles in experimentally decompressed plagioclase crystals. Grey scale intensity is proportional to anorthite content; brighter regions are more anorthite rich. (a) Diffusely zoned plagioclase crystal, CD at 1 MPa hr^{-1}, P_f = 25. (b) Sharply zoned plagioclase crystal, SSD, P_f = 25 MPa, t_{dw} =168 hours. Crystallization intervals both ~7 days, but time since pressure perturbation is *longer* in crystal (b), which has the sharpest boundary. (c) Core-to-rim concentration profiles of crystals in (a) and (b), normalized to maximum (core) and minimum (rim) greyscale values. Length scale is same in both profiles and centered at x = 0. Assuming initially stepped zoning profile (solid black line) yields longer relaxation timescale for slowly decompressed sample.

Figure 13: Crystallization regime (N_A–ϕ) diagram for experimental and natural samples. Nucleation-dominated crystallization defines steep trends in N_A–ϕ space; growth-dominated trends are near-horizontal. Shaded fields in (a) and (b) show the range of values measured in natural pyroclasts erupted during 1980; LND = low number density clasts; BML = bimodal clasts; HND = high number density clasts (data from Cashman & Hoblitt, 2004; Cashman & McConnell, 2005). (a) Compares natural data with CD trends; black arrows are CD at XH_2O^{fl} = 1.0; grey dashed arrows are CD at XH_2O^{fl} = 0.8. Thick grey lines are approximate contours of final pressure. (b) Compares natural data with SSD experiments. Data are largely time-invariant; P_f shown by thick grey lines for t_{dw} = 24–168 hours. Panels (c) and (d) compare textural data for our water-saturated runs to those from other experimental decompressions of rhyolitic melts at similar temperatures (850–880 °C; data from Couch *et al.*, 2003; Brugger & Hammer, 2010*a*; Martel, 2012). Note the expanded x-axis range in (c) and (d).

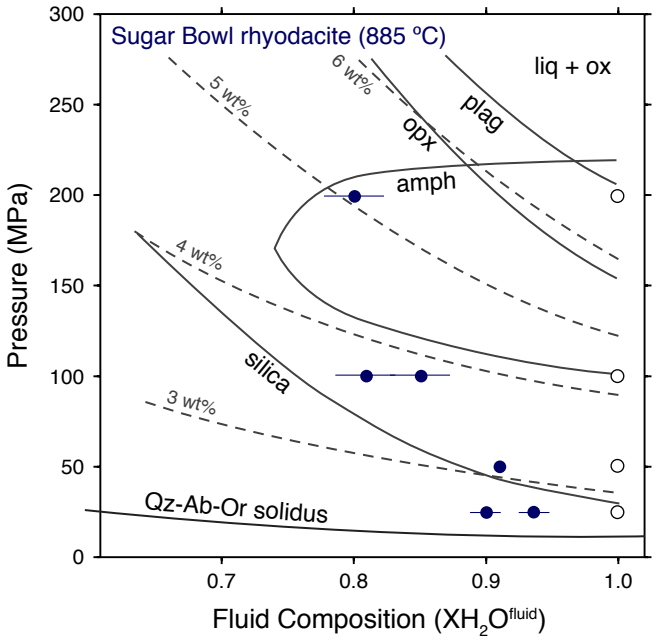
Sugar Bowl rhyodacite (885 ºC)
liq + ox
plag
opx
amph
silica
Qz-Ab-Or solidus
6 wt%
5 wt%
4 wt%
3 wt%
Pressure (MPa)
Fluid Composition (XH2Ofluid)
300
250
200
150
100
50
0
0.7
0.8
0.9
1.0

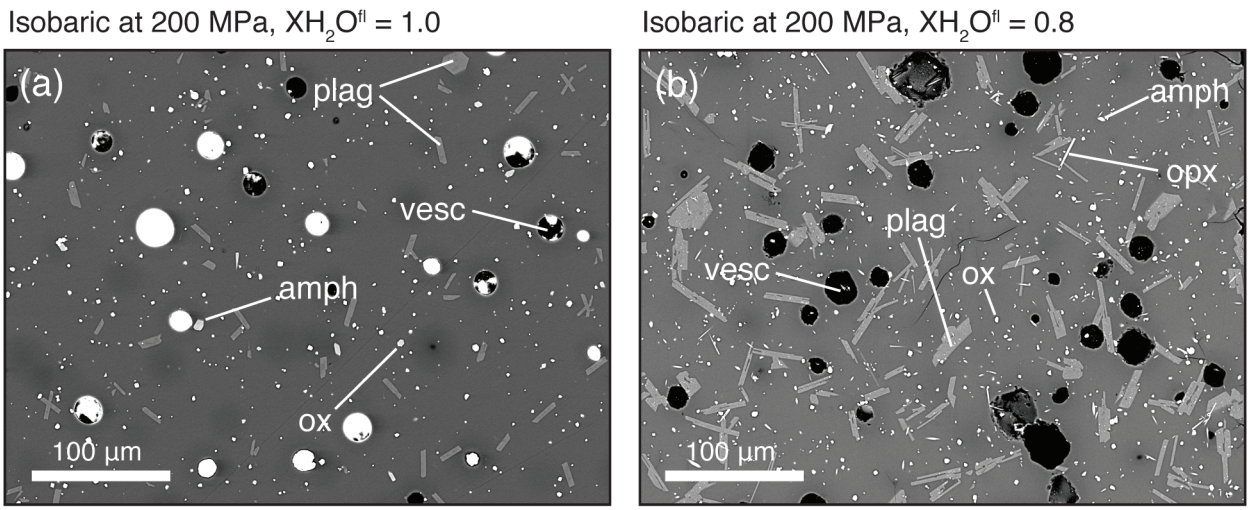
Isobaric at 200 MPa, XH_2O^{fl} = 1.0
(a)
plag
vesc
amph
ox
100 µm
Isobaric at 200 MPa, XH_2O^{fl} = 0.8
(b)
amph
opx
plag
vesc
ox
100 µm

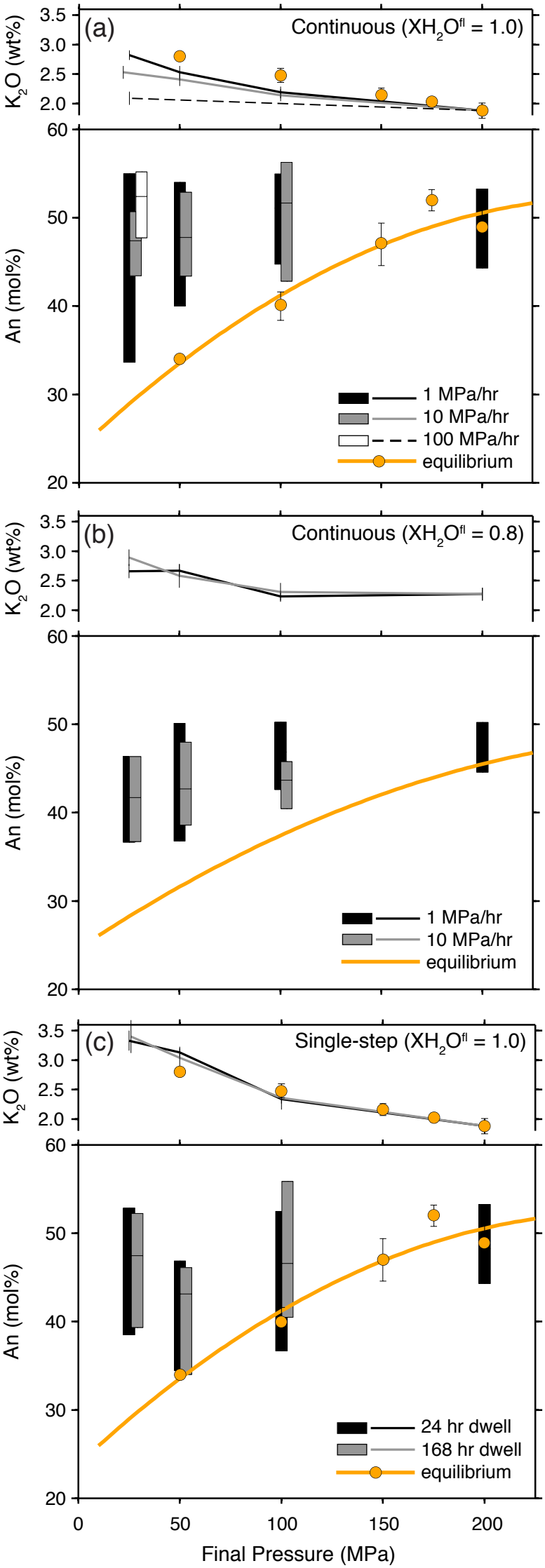
(a)
Continuous (XH_2O^{fl} = 1.0)
K_2O (wt%)
An (mol%)
1 MPa/hr
10 MPa/hr
100 MPa/hr
equilibrium
(b)
Continuous (XH_2O^{fl} = 0.8)
K_2O (wt%)
An (mol%)
1 MPa/hr
10 MPa/hr
equilibrium
(c)
Single-step (XH_2O^{fl} = 1.0)
K_2O (wt%)
An (mol%)
24 hr dwell
168 hr dwell
equilibrium
Final Pressure (MPa)

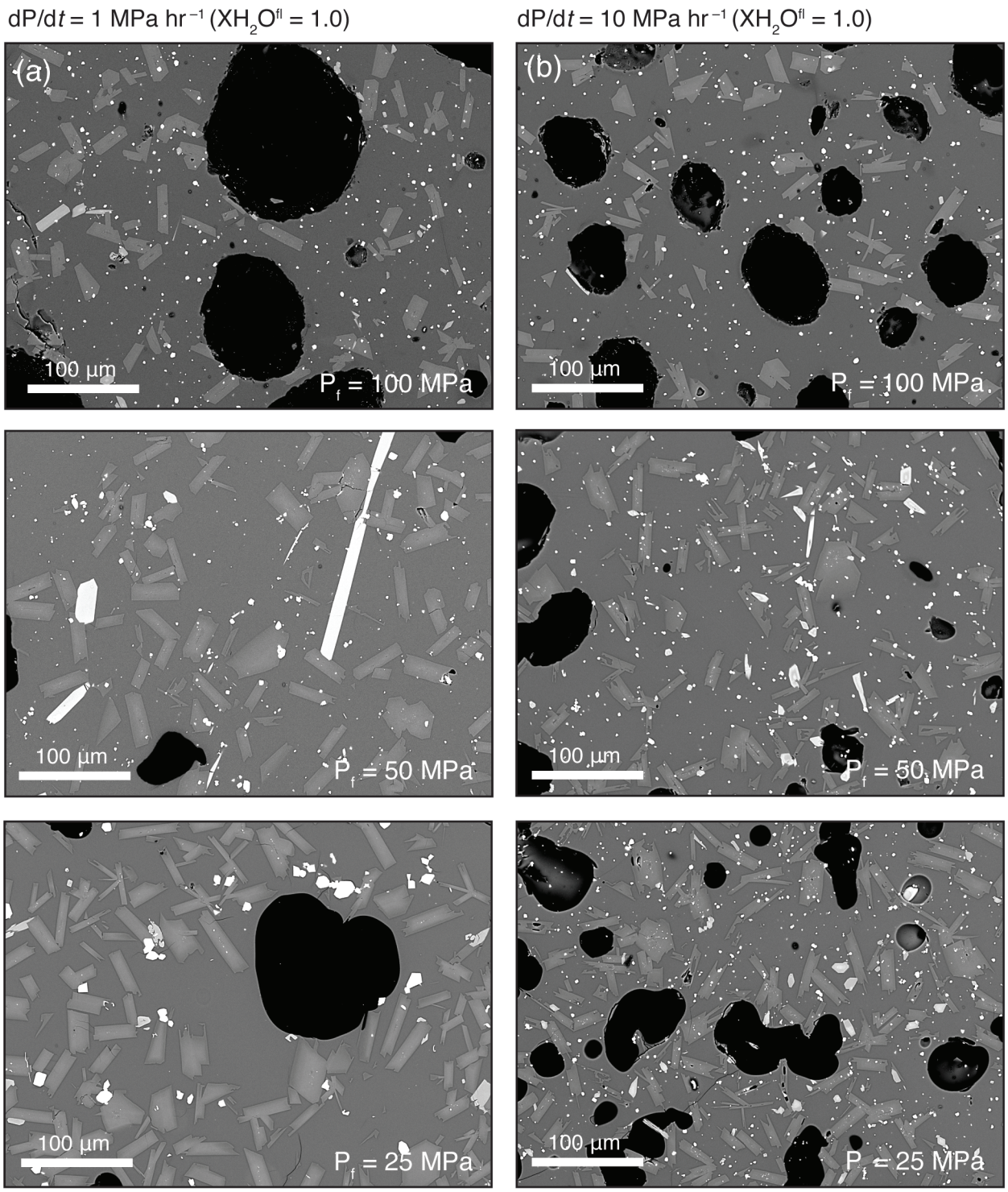
dP/dt = 1 MPa hr⁻¹ (XH2Of = 1.0)
dP/dt = 10 MPa hr⁻¹ (XH2Of = 1.0)
(a)
(b)
100 µm
Pf = 100 MPa
100 µm
Pf = 100 MPa
100 µm
Pf = 50 MPa
100 µm
Pf = 50 MPa
100 µm
Pf = 25 MPa
100 µm
Pf = 25 MPa

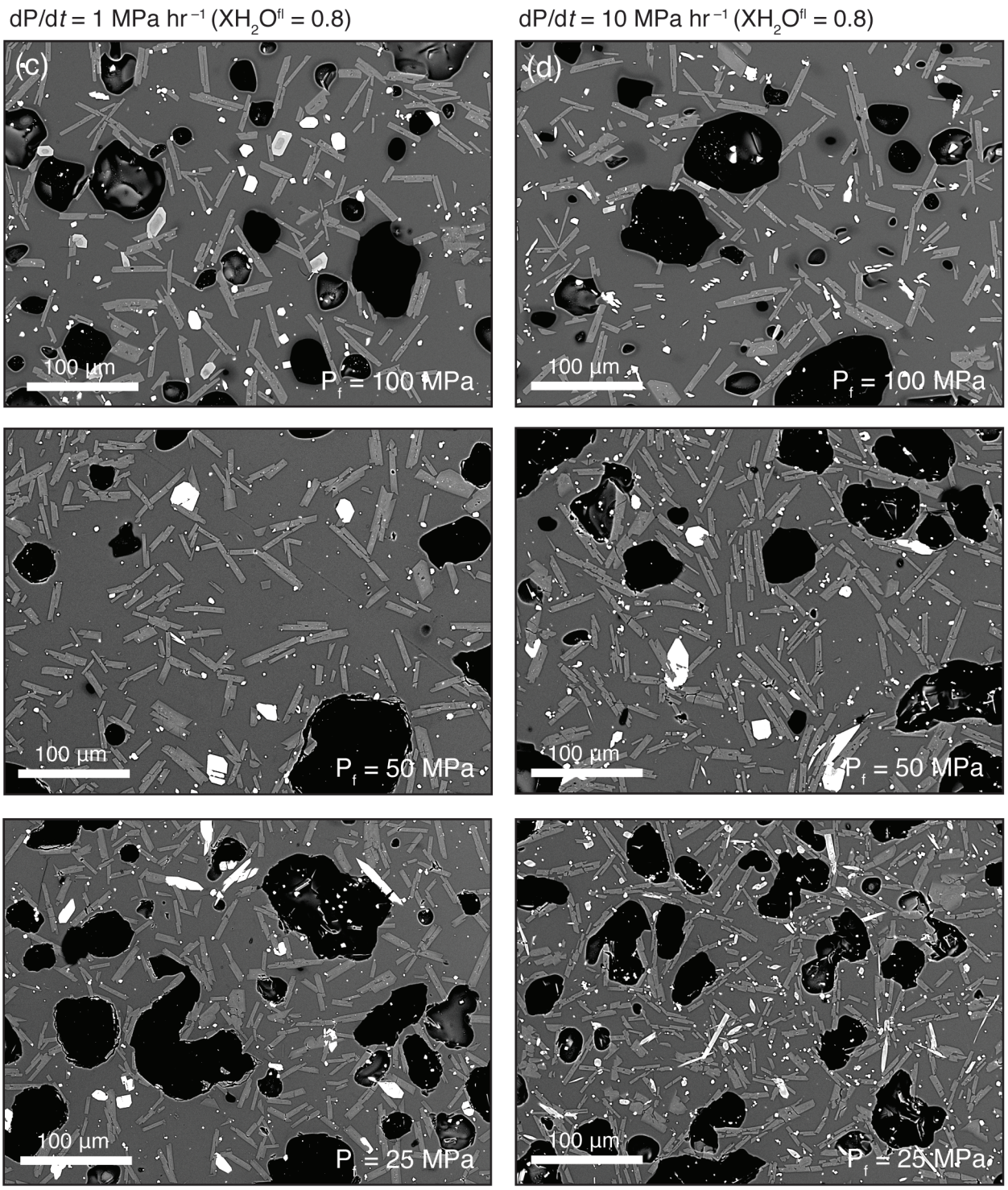
dP/dt = 1 MPa hr⁻¹ (XH2Of = 0.8)
dP/dt = 10 MPa hr⁻¹ (XH2Of = 0.8)
(c)
(d)
100 µm
Pf = 100 MPa
100 µm
Pf = 100 MPa
100 µm
Pf = 50 MPa
100 µm
Pf = 50 MPa
100 µm
Pf = 25 MPa
100 µm
Pf = 25 MPa

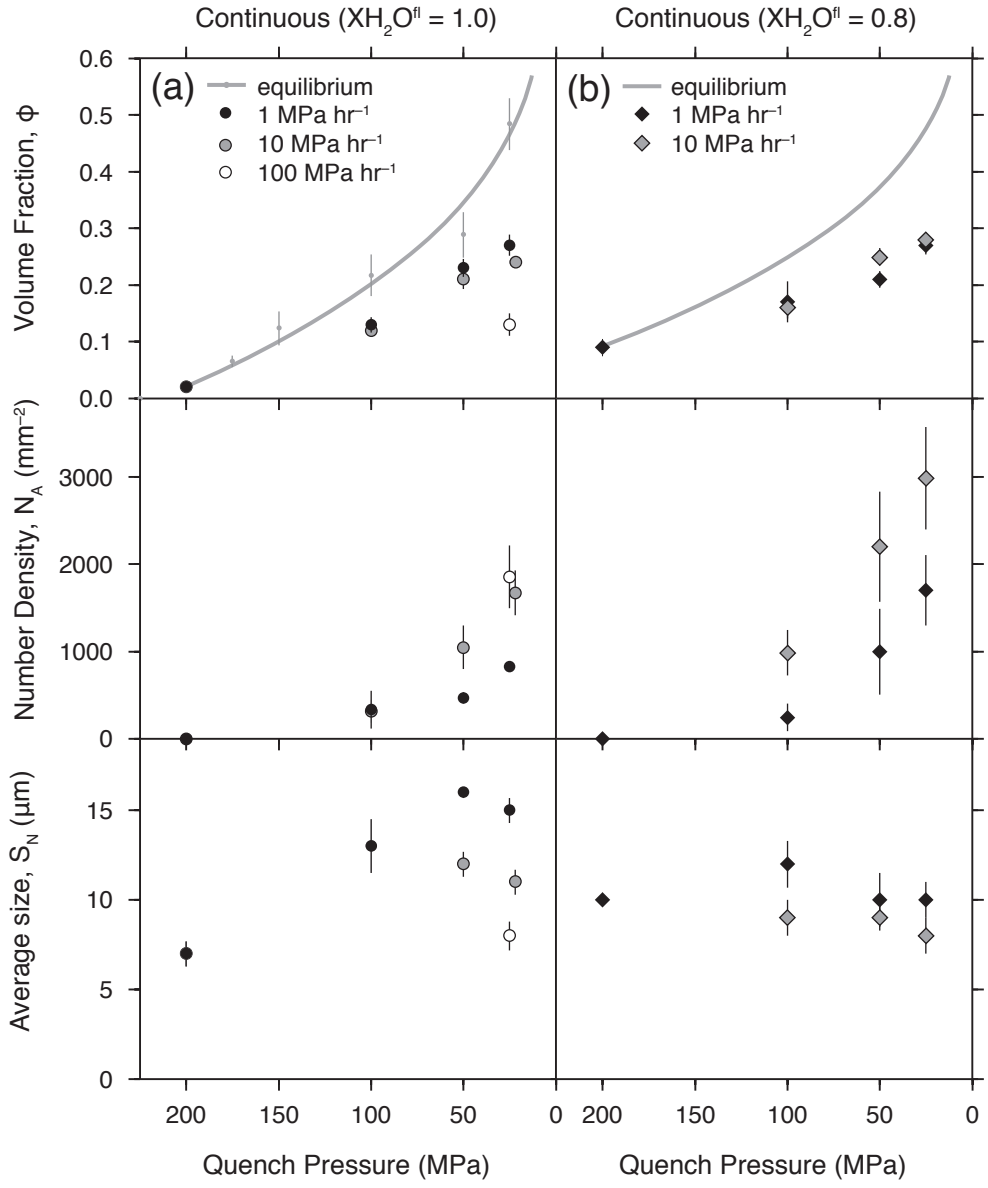
Continuous (XH_2O^{fl} = 1.0)
Continuous (XH_2O^{fl} = 0.8)
(a)
(b)
equilibrium
1 MPa hr^{-1}
10 MPa hr^{-1}
100 MPa hr^{-1}
Volume Fraction, Φ
Number Density, N_A (mm^{-2})
Average size, S_N (μm)
Quench Pressure (MPa)
0.0
0.1
0.2
0.3
0.4
0.5
0.6
0
1000
2000
3000
0
5
10
15
200
150
100
50
0

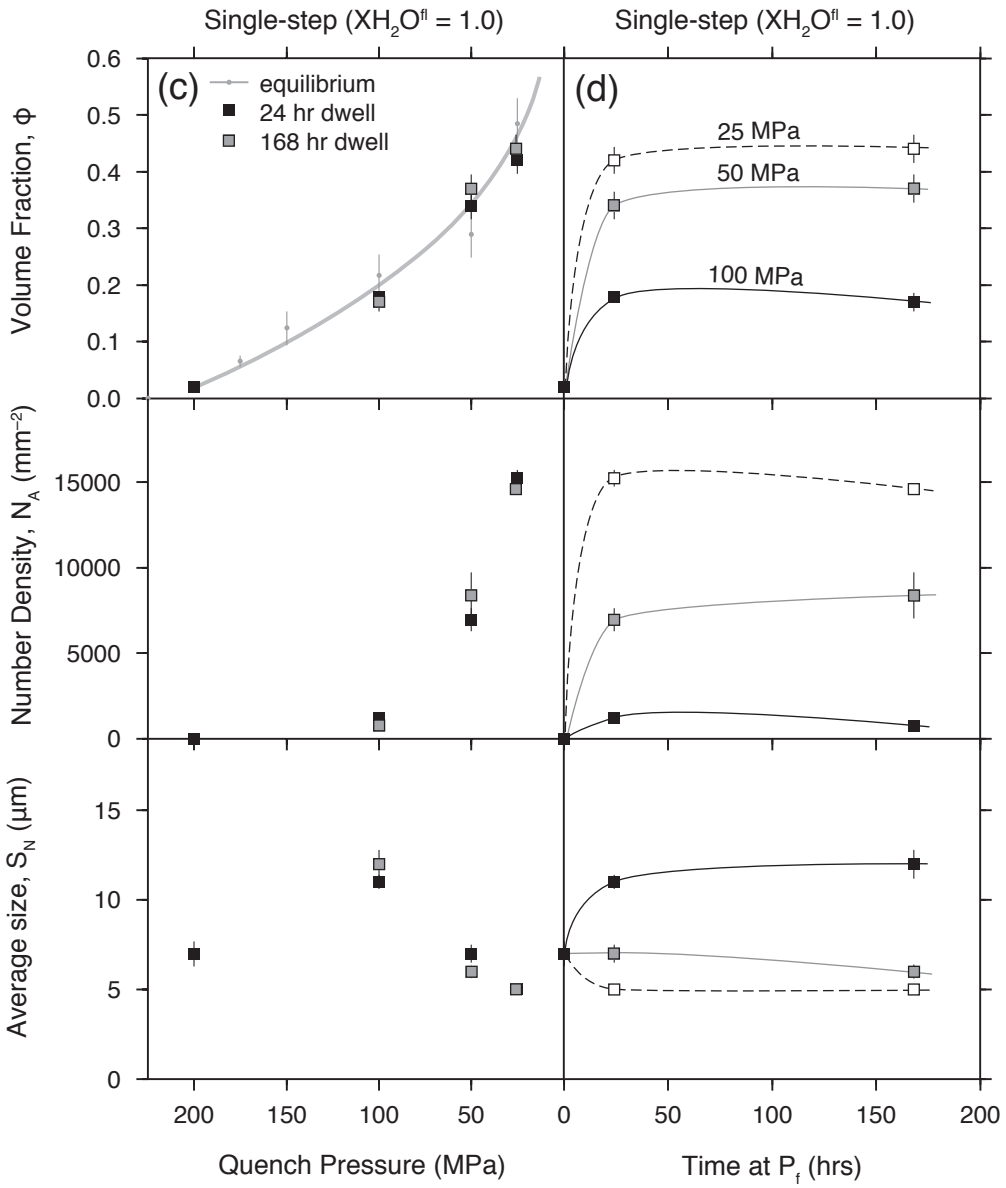
Single-step (XH_2O^{fl} = 1.0)
Single-step (XH_2O^{fl} = 1.0)
(c)
equilibrium
24 hr dwell
168 hr dwell
(d)
25 MPa
50 MPa
100 MPa
Volume Fraction, ϕ
Number Density, N_A (mm^{-2})
Average size, S_N (μm)
Quench Pressure (MPa)
Time at P_f (hrs)

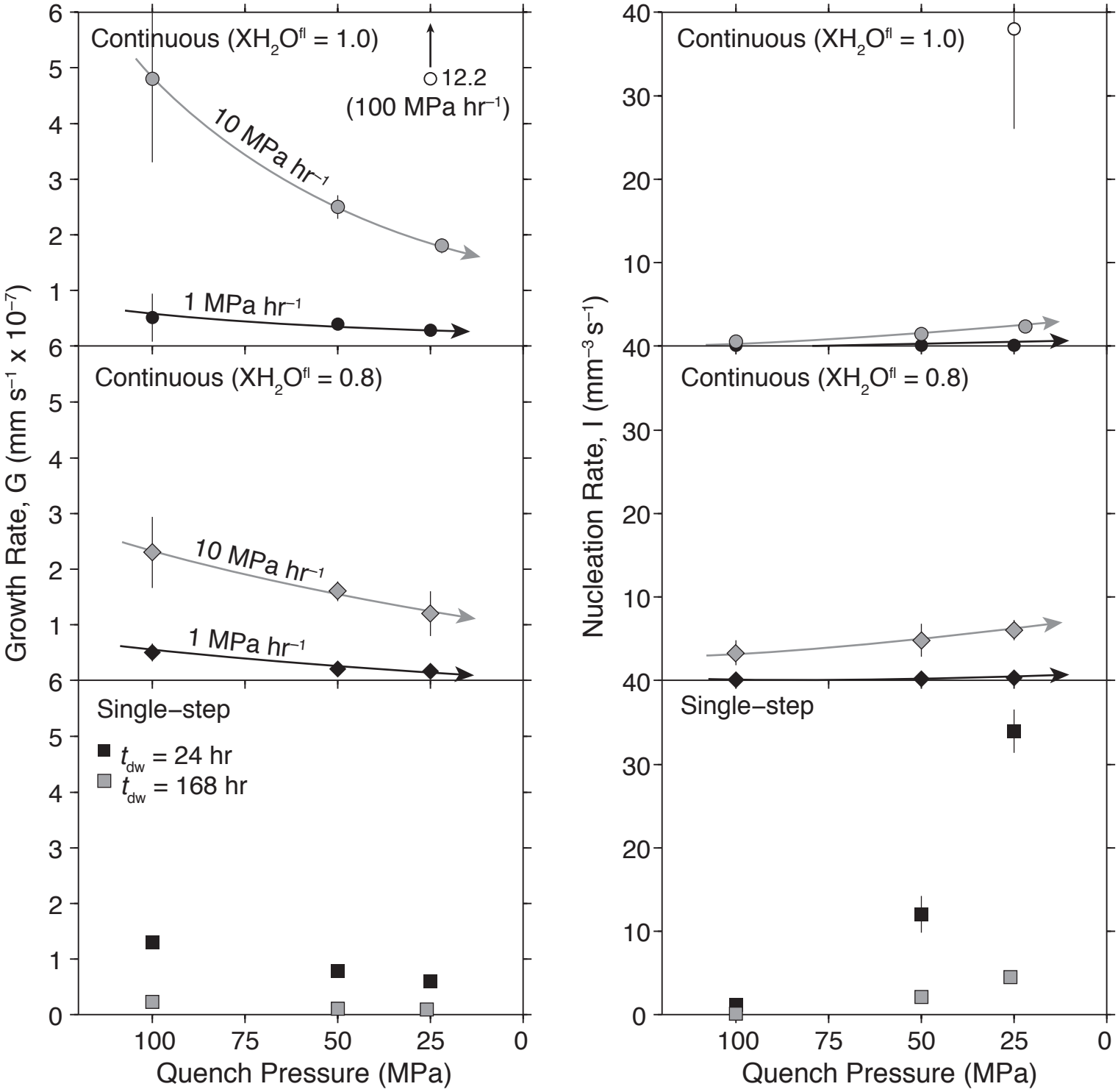
Continuous (XH_2O^{fl} = 1.0)
12.2
(100 MPa hr^{-1})
10 MPa hr^{-1}
1 MPa hr^{-1}
Continuous (XH_2O^{fl} = 0.8)
10 MPa hr^{-1}
1 MPa hr^{-1}
Single–step
t_{dw} = 24 hr
t_{dw} = 168 hr
Growth Rate, G (mm s^{-1} x 10^{-7})
Nucleation Rate, I (mm^{-3} s^{-1})
Quench Pressure (MPa)
100
75
50
25
0

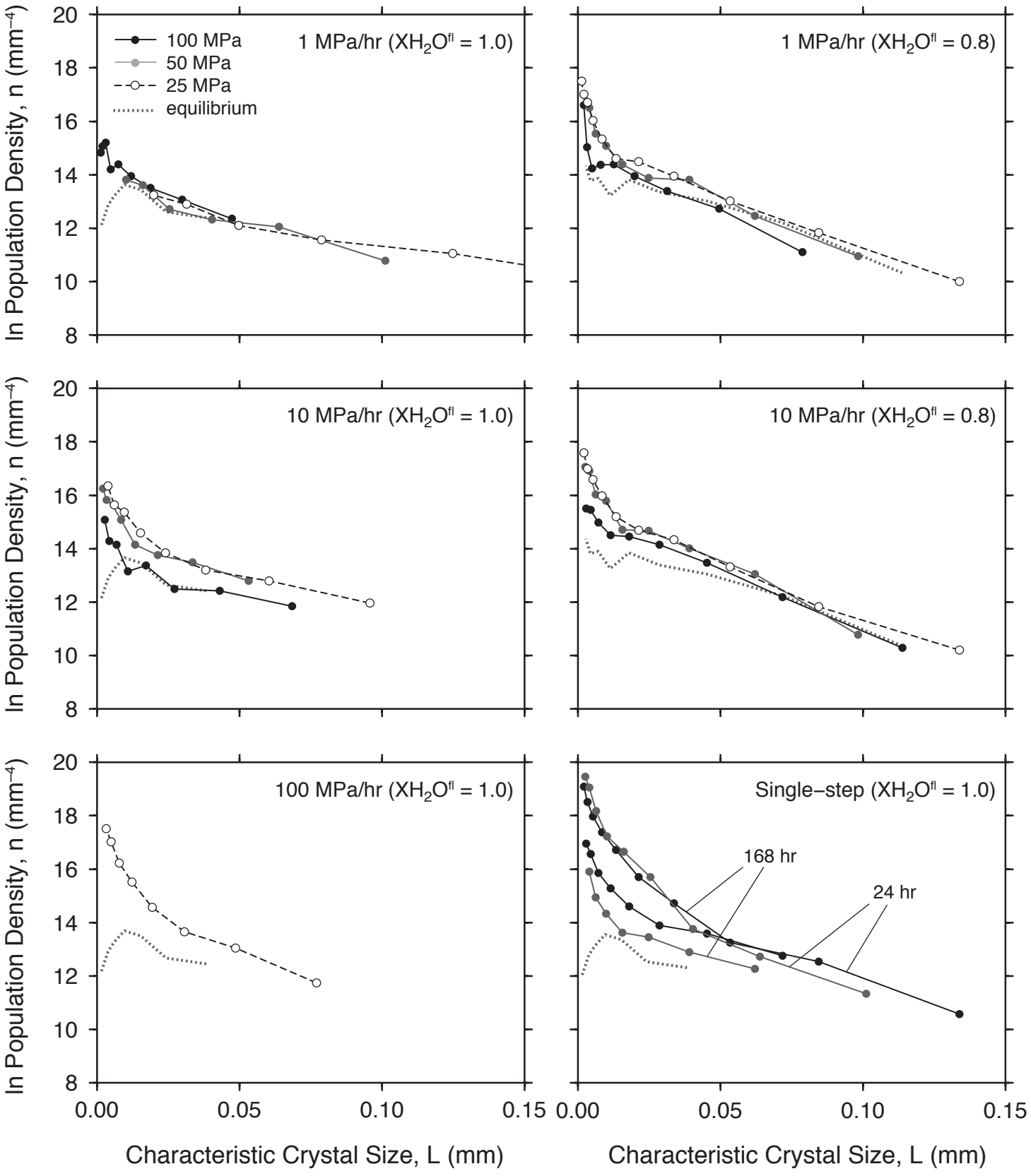
100 MPa
50 MPa
25 MPa
equilibrium
1 MPa/hr (XH_2O^{fl} = 1.0)
1 MPa/hr (XH_2O^{fl} = 0.8)
10 MPa/hr (XH_2O^{fl} = 1.0)
10 MPa/hr (XH_2O^{fl} = 0.8)
100 MPa/hr (XH_2O^{fl} = 1.0)
Single–step (XH_2O^{fl} = 1.0)
168 hr
24 hr
ln Population Density, n (mm^{-4})
Characteristic Crystal Size, L (mm)
20
18
16
14
12
10
8
0.00
0.05
0.10
0.15

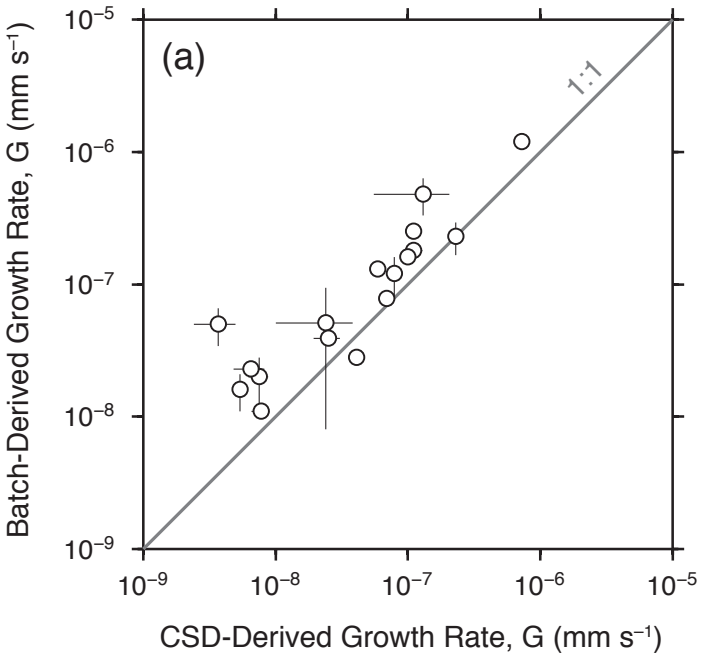
(a)
1:1
Batch-Derived Growth Rate, G (mm s⁻¹)
CSD-Derived Growth Rate, G (mm s⁻¹)
10⁻⁵
10⁻⁶
10⁻⁷
10⁻⁸
10⁻⁹

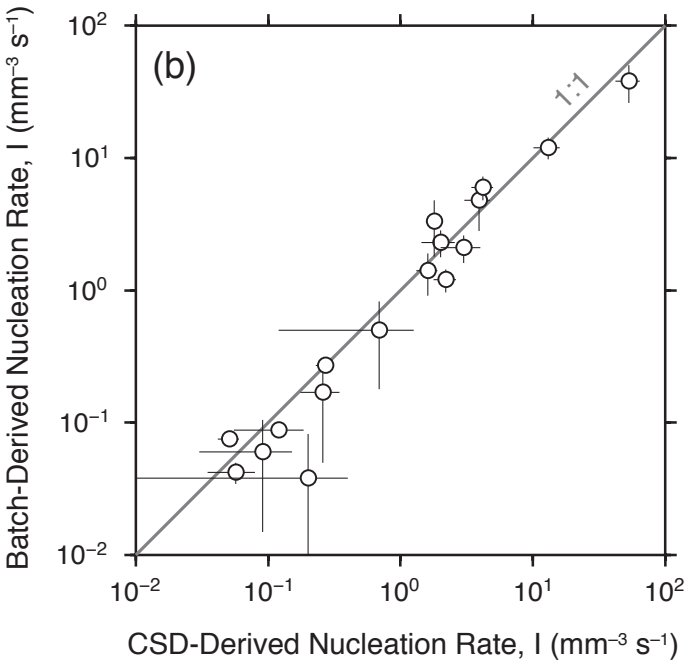
(b)
1:1
Batch-Derived Nucleation Rate, I (mm⁻³ s⁻¹)
CSD-Derived Nucleation Rate, I (mm⁻³ s⁻¹)
10²
10¹
10⁰
10⁻¹
10⁻²

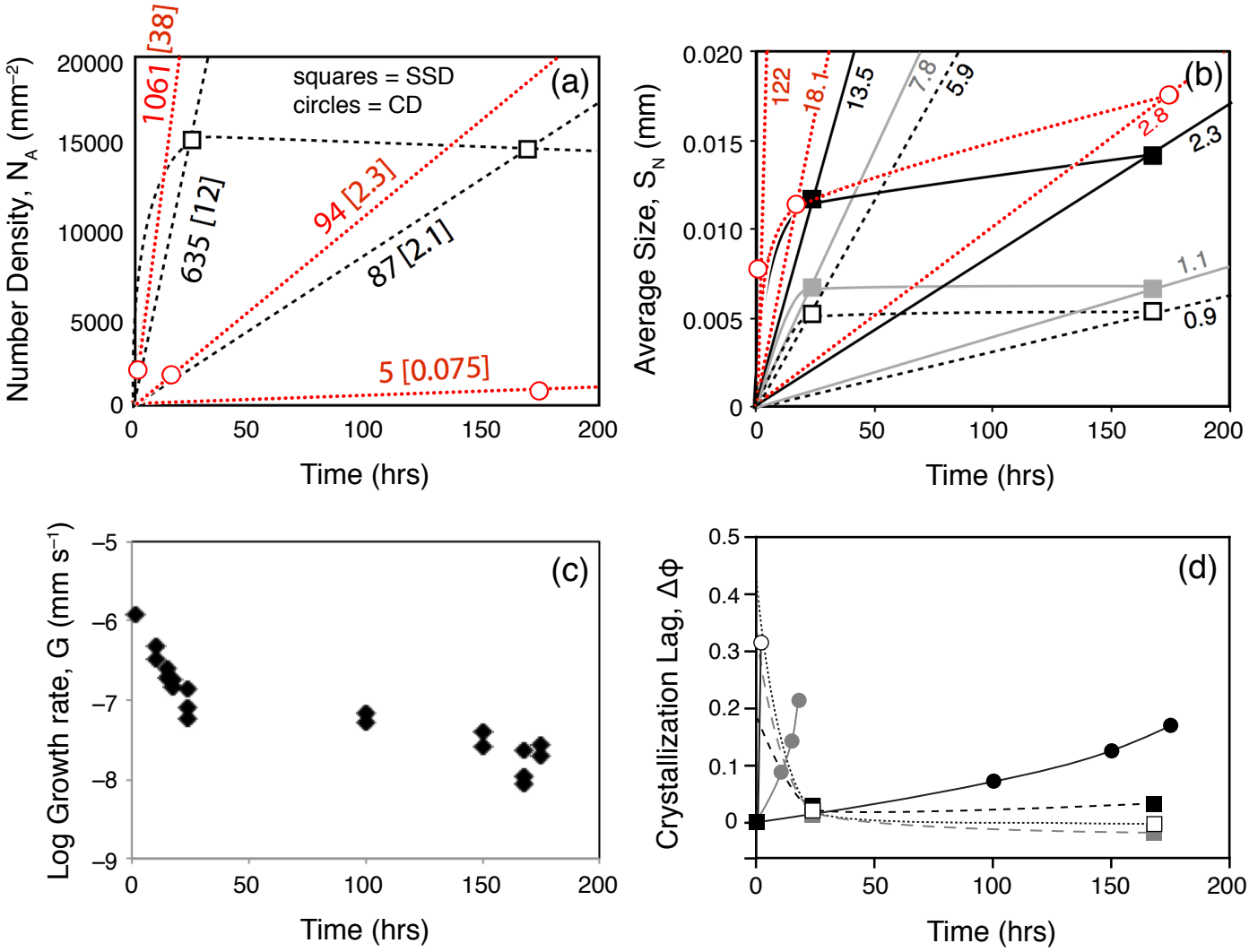
Number Density, N_A (mm^{-2})
20000
15000
10000
5000
0
squares = SSD
circles = CD
(a)
1061 [38]
635 [12]
94 [2.3]
87 [2.1]
5 [0.075]
0
50
100
150
200
Time (hrs)
Average Size, S_N (mm)
0.020
0.015
0.010
0.005
0
(b)
122
18.1
13.5
7.8
5.9
2.8
2.3
1.1
0.9
0
50
100
150
200
Time (hrs)
Log Growth rate, G (mm s^{-1})
−5
−6
−7
−8
−9
(c)
0
50
100
150
200
Time (hrs)
Crystallization Lag, Δφ
0.5
0.4
0.3
0.2
0.1
0
(d)
0
50
100
150
200
Time (hrs)

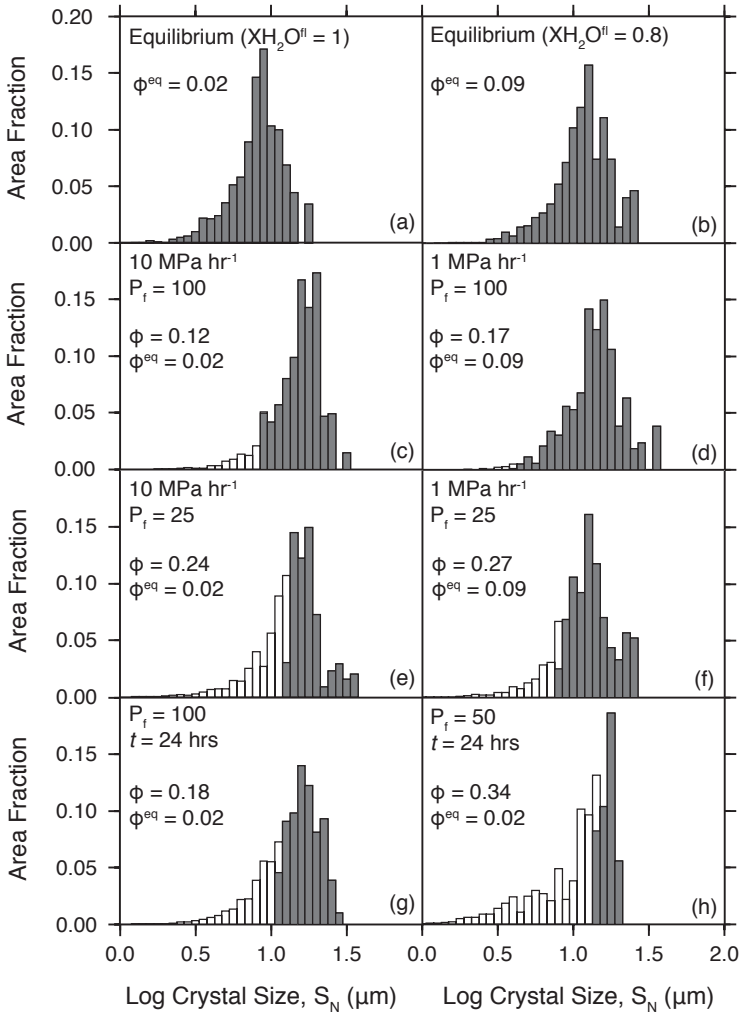
Equilibrium (XH_2O^{fl} = 1)
ϕ^{eq} = 0.02
(a)
Equilibrium (XH_2O^{fl} = 0.8)
ϕ^{eq} = 0.09
(b)
10 MPa hr^{-1}
P_f = 100
ϕ = 0.12
ϕ^{eq} = 0.02
(c)
1 MPa hr^{-1}
P_f = 100
ϕ = 0.17
ϕ^{eq} = 0.09
(d)
10 MPa hr^{-1}
P_f = 25
ϕ = 0.24
ϕ^{eq} = 0.02
(e)
1 MPa hr^{-1}
P_f = 25
ϕ = 0.27
ϕ^{eq} = 0.09
(f)
P_f = 100
t = 24 hrs
ϕ = 0.18
ϕ^{eq} = 0.02
(g)
P_f = 50
t = 24 hrs
ϕ = 0.34
ϕ^{eq} = 0.02
(h)
Area Fraction
0.00
0.05
0.10
0.15
0.20
0.0
0.5
1.0
1.5
2.0
Log Crystal Size, S_N (μm)

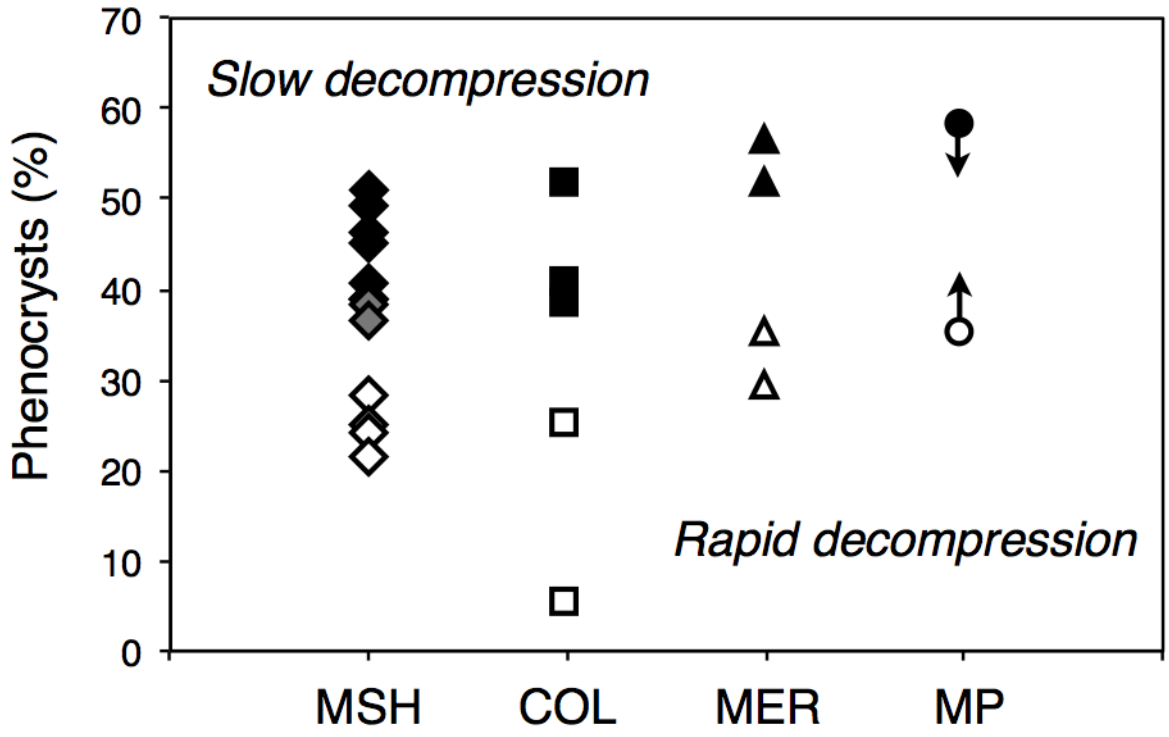
Slow decompression
Rapid decompression
Phenocrysts (%)
70
60
50
40
30
20
10
0
MSH
COL
MER
MP

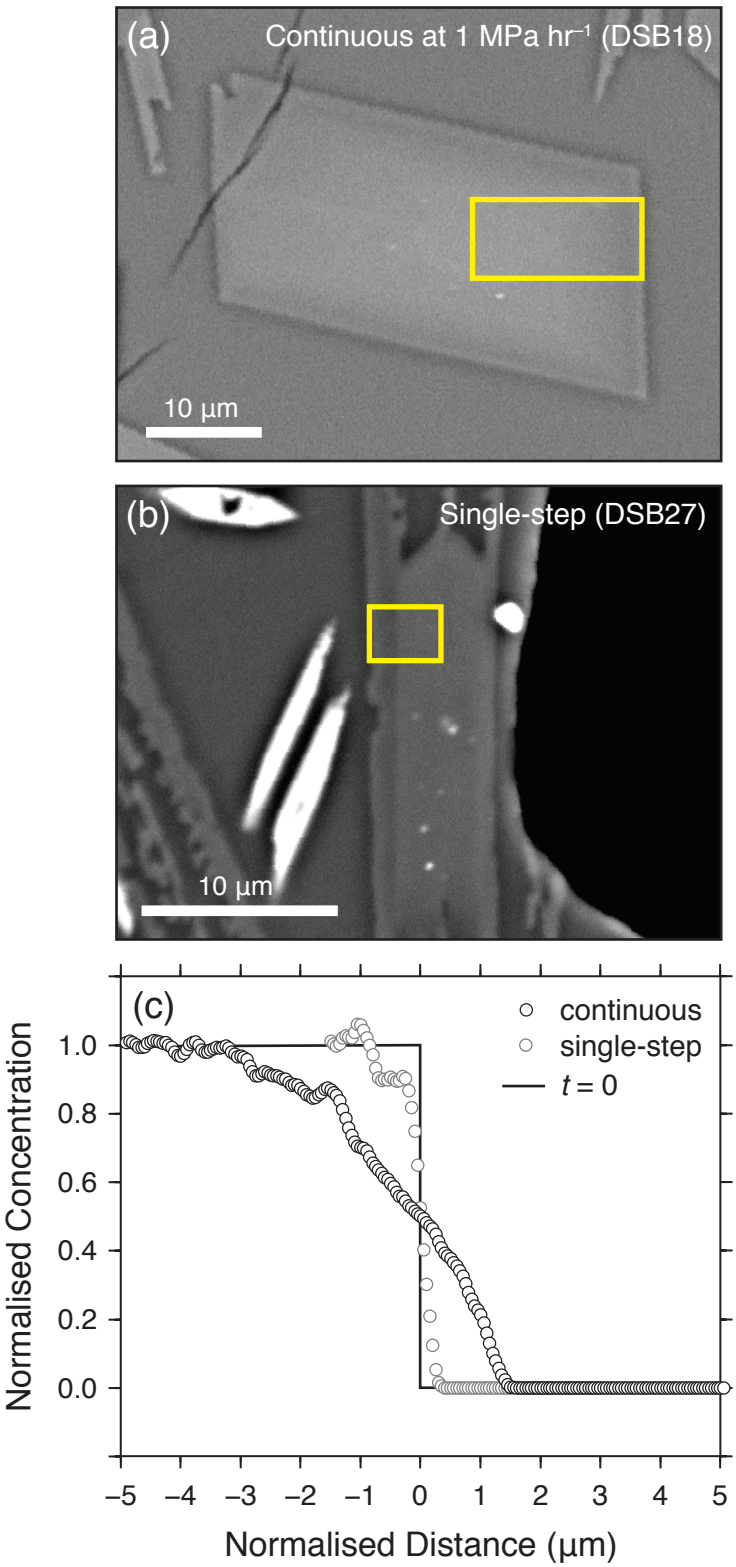
(a)
Continuous at 1 MPa hr⁻¹ (DSB18)
10 µm
(b)
Single-step (DSB27)
10 µm
(c)
continuous
single-step
t = 0
Normalised Concentration
1.0
0.8
0.6
0.4
0.2
0.0
−5
−4
−3
−2
−1
0
1
2
3
4
5
Normalised Distance (µm)

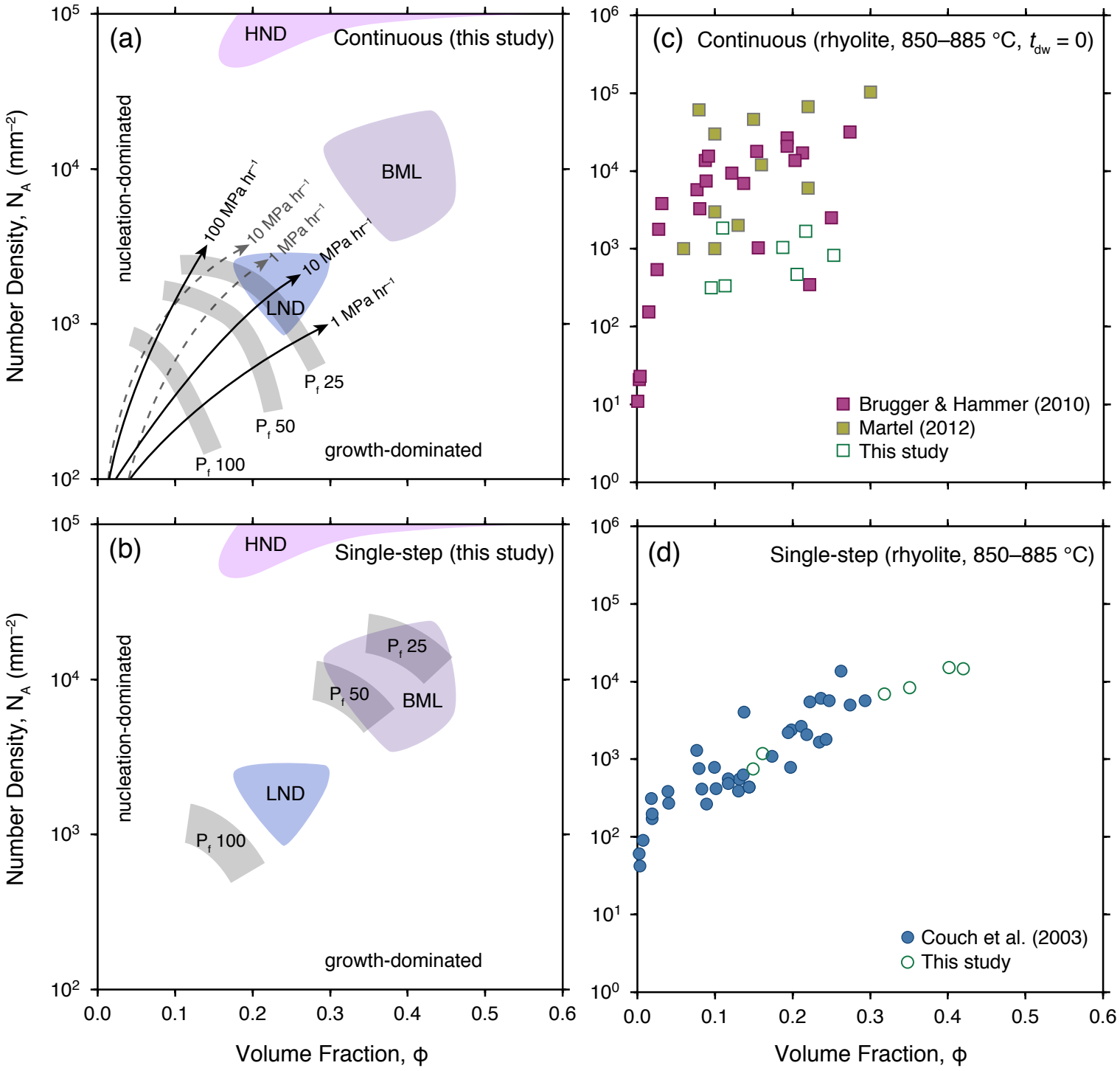
(a)
Continuous (this study)
HND
BML
LND
nucleation-dominated
growth-dominated
100 MPa hr⁻¹
10 MPa hr⁻¹
1 MPa hr⁻¹
10 MPa hr⁻¹
1 MPa hr⁻¹
P_f 25
P_f 50
P_f 100
(b)
Single-step (this study)
HND
P_f 25
P_f 50
BML
LND
P_f 100
nucleation-dominated
growth-dominated
(c)
Continuous (rhyolite, 850–885 °C, t_dw = 0)
Brugger & Hammer (2010)
Martel (2012)
This study
(d)
Single-step (rhyolite, 850–885 °C)
Couch et al. (2003)
This study
Number Density, N_A (mm⁻²)
Volume Fraction, ϕ

Table 1: Bulk composition of experimental starting material (wt% anhydrous)

SiO_2	TiO_2	Al_2O_3	FeO_T	MnO	MgO	CaO	Na_2O	K_2O	P_2O_5
69.52	0.36	16.05	3.36	0.06	0.83	3.00	4.90	1.81	0.10

Table 2: Run conditions and run products of decompression experiments. All runs at 885 °C.

Sample	Type [a]	XH_2O^{fl} [b] (initial)	XH_2O^{fl} [b] (final)	t_{eq} [c] (h)	dP/dt (MPa/h)	P_f (MPa)	t_{dw} [c] (h)	t_{dc} [c] (h)	t_{xst} [c] (h)	Run Products [d]
DSB6	REF	1.0	–	72	–	200	0	0	0	Gl, Vap, Pl, Ox, Am
DSB19	CD	1.0	–	72	1	100	0	100	100	Gl, Vap, Pl, Ox, Am
DSB9	CD	1.0	–	72	1	50	0	150	150	Gl, Vap, Pl, Ox, [Am], Opx
DSB18	CD	1.0	–	72	1	25	0	175	175	Gl, Vap, Pl, Ox, [Am], Opx
DSB16	CD	1.0	–	72	10	100	0	10	10	Gl, Vap, Pl, Ox, Am
DSB28	CD	1.0	–	72	10	50	0	15	15	Gl, Vap, Pl, Ox, Am
DSB26	CD	1.0	–	72	10	22	0	18	18	Gl, Vap, Pl, Ox, Am
DSB22	CD	1.0	–	72	100	25	0	2	2	Gl, Vap, Pl, Ox, Am
DSB39	REF	0.8	0.80 (0.02)	168	–	200	0	0	0	Gl, Vap, Pl, Ox, Opx, Am
DSB35	CD	0.8	0.81 (0.02)	168	1	100	0	100	100	Gl, Vap, Pl, Ox, Opx, [Am]
DSB38	CD	0.8	–	168	1	50	0	150	150	Gl, Vap, Pl, Ox, Opx
DSB34	CD	0.8	0.93 (0.01)	168	1	25	0	175	175	Gl, Vap, Pl, Ox, Opx
DSB36	CD	0.8	0.85 (0.02)	168	10	100	0	10	10	Gl, Vap, Pl, Ox, Opx, Am
DSB37	CD	0.8	0.91 (<0.01)	168	10	50	0	15	15	Gl, Vap, Pl, Ox, Opx, Am
DSB33	CD	0.8	0.90 (0.01)	168	10	25	0	18	18	Gl, Vap, Pl, Ox, Opx, [Am]
DSB23	SSD	1.0	–	72	–	100	24	0	24	Gl, Vap, Pl, Ox, Am
DSB13	SSD	1.0	–	72	–	50	24	0	24	Gl, Vap, Pl, Ox, Opx, [Am]
DSB25	SSD	1.0	–	72	–	25	24	0	24	Gl, Vap, Pl, Ox, Opx, Si
DSB17	SSD	1.0	–	72	–	100	168	0	168	Gl, Vap, Pl, Ox, Opx
DSB24	SSD	1.0	–	72	–	50	168	0	168	Gl, Vap, Pl, Ox, Opx, Si
DSB27	SSD	1.0	–	72	–	26	168	0	168	Gl, Vap, Pl, Ox, Opx, Si

[a] CD = continuous decompression; SSD = single-step decompression; REF = equilibrium reference run.

[b] Mole fraction of water in the fluid/vapour phase. Final fluid composition was measured by gravimetry; parentheses give uncertainties. Fluid compositions of water-saturated experiments were not measured.

[c] t_{eq} = length of time spent at initial pressure prior to the onset of decompression ("anneal" period); t_{dw} = dwell time at final pressure; t_{dc} = duration of active decompression; t_{xst} = time available for decompression crystallisation (= t_{dc} + t_{dw}).

[d] Gl = glass; Vap = vapor; Pl = plagioclase; Am = amphibole; Opx = orthopyroxene; Ox = Fe–Ti oxides; Si = silica phase. Brackets indicate resorbed or reacting amphibole.

Table 3: Two-dimensional (batch) textural analyses of experimental plagioclase crystals.

Sample	N_A[a] (mm^{-2})	ϕ[a] (vol. fraction)	S_N (mm)	Growth rate, G ($mm\ s^{-1}$)	Nucleation Rate, I ($mm^{-3}\ s^{-1}$)	Habit[b]	Aspect ratio[c]
Equilibrium reference runs							
DSB6	422 (74)	0.020 (0.004)	0.007 (0.001)	–	–	P	3.3
DSB39	1018 (80)	0.094 (0.015)	0.010 (0.000)	–	–	H	4.9
Continuous decompression, $XH_2O^{fl} = 1.0$							
DSB19	334 (217)[d]	0.134 (0.013)	0.013 (0.002)	5.1E-08 (4.3)	6.0E-02 (4.5)	P	2.8
DSB9	472 (67)	0.226 (0.016)	0.016 (0.000)	3.9E-08 (0.2)	4.2E-02 (0.8)	P	3.2
DSB18	827 (48)	0.273 (0.019)	0.015 (0.001)	2.8E-08 (0.2)	7.5E-02 (0.8)	P [S]	3.6
DSB16	315 (134)	0.116 (0.006)	0.013 (0.002)	4.8E-07 (1.5)	5.0E-01 (3.2)	P	3.5
DSB28	1047 (250)	0.208 (0.017)	0.012 (0.001)	2.5E-07 (0.2)	1.4E+00 (0.5)	P [S]	3.3
DSB26	1673 (254)	0.237 (0.001)	0.011 (0.001)	1.8E-07 (0.1)	2.3E+00 (0.5)	P [S]	3.9
DSB22	1857 (361)	0.130 (0.020)	0.008 (0.001)	1.2E-06 (0.2)	3.8E+01 (1.2)	S	3.4
Continuous decompression, $XH_2O^{fl} = 0.8$							
DSB35	244 (156)	0.173 (0.036)	0.012 (0.001)	5.0E-08 (1.6)	3.8E-02 (440)	H	4.3
DSB38	997 (491)	0.210 (0.015)	0.010 (0.002)	2.0E-08 (0.8)	1.7E-01 (0.1)	H	3.8
DSB34	1702 (402)	0.270 (0.016)	0.010 (0.001)	1.6E-08 (0.5)	2.7E-01 (0.3)	H	4.0
DSB36	985 (261)	0.163 (0.019)	0.009 (0.001)	2.3E-07 (0.6)	3.3E+00 (1.5)	H	4.5
DSB37	2201 (631)	0.252 (0.015)	0.009 (0.001)	1.6E-07 (0.2)	4.8E+00 (2.0)	H	4.0
DSB33	2984 (588)	0.279 (0.014)	0.008 (0.001)	1.2E-07 (0.4)	6.0E+00 (1.2)	H	4.1
Single-step decompression, $XH_2O^{fl} = 1.0$							
DSB23	1190 (176)	0.181 (0.008)	0.011 (0.000)	1.3E-07 (0.1)	1.2E+00 (0.2)	S	4.0
DSB13	6960 (666)	0.338 (0.024)	0.007 (0.001)	7.8E-08 (0.7)	1.2E+01 (0.2)	S	3.9
DSB25	15234 (473)	0.421 (0.024)	0.005 (0.000)	5.9E-08 (0.3)	3.4E+01 (0.3)	D	n.d.
DSB17	747 (37)	0.169 (0.016)	0.012 (0.001)	2.3E-08 (0.2)	8.8E-02 (1.1)	S	3.7
DSB24	8391 (1351)	0.371 (0.025)	0.006 (0.000)	1.1E-08 (0.1)	2.1E+00 (0.5)	S	4.3
DSB27	14585 (899)	0.440 (0.025)	0.005 (0.000)	8.9E-09 (0.4)	4.5E+00 (0.2)	D	n.d.

[a] Values corrected for the presence of pre-existing crystals as given by equilibrium reference experiments (N_A = measured $N_A - N_{AREF}$; ϕ = measured $\phi - \phi_{REF}$). Values for reference runs are reported as measured.

[b] Dominant crystal habit. P = prismatic; S = skeletal; H = hopper/swallowtail; D = dendritic. P [S] indicates dominantly prismatic crystals with hopper/swallowtail or skeletal overgrowths.

[c] Average 2D crystal aspect ratio, calculated as major axis length over minor axis length.

[d] Parentheses give 1σ variability of multiple images or sub-sampled crystal populations within a single image.

Table 4: Crystal size distribution (CSD) analyses of experimental plagioclase crystals.

Sample	n [a]	Crystal shapes [b]		CSD regressions [c]			n^0	Gτ (mm)	G (mm s^{-1})	I (mm^{-3} s^{-1})
		s:i:l	r^2	slope	intercept	r^2				
Equilibrium reference runs										
DSB6	416	1:3:6	0.91	-57.2 (14.2)	14.5 (0.3)	0.89	2.0e+6 (0.7)	0.017 (0.004)	6.7e-8 (1.7)	1.4e-1 (0.6)
DSB39	312	1:4:9	0.87	-39.0 (3.9)	14.2 (0.2)	0.93	1.5e+6 (0.3)	0.026 (0.003)	4.2e-8 (0.4)	6.4e-2 (1.4)
Continuous decompression, $XH_2O^{fl} = 1.0$										
DSB19	605	1:3:4	0.87	-117.8 (70.9)	15.2 (0.3)	0.48	3.9e+6 (1.2)	0.008 (0.005)	2.4e-8 (1.4)	9.1e-2 (6.1)
DSB9	405	1:3:5	0.84	-74.8 (16.9)	14.7 (0.3)	0.95	2.3e+6 (0.7)	0.013 (0.003)	2.5e-8 (0.6)	5.7e-2 (2.2)
DSB18	853	1:2:9	0.80	-38.3 (4.1)	14.0 (0.1)	0.99	1.2e+6 (0.2)	0.026 (0.003)	4.1e-8 (0.4)	5.1e-2 (1.0)
DSB16	470	1:3:6	0.88	-211.5 (121.1)	15.5 (0.6)	0.75	5.3e+6 (3.1)	0.005 (0.003)	1.3e-7 (0.8)	6.9e-1 (5.7)
DSB28	959	1:3:5	0.81	-174.1 (22.7)	16.5 (0.1)	0.97	1.5e+7 (0.2)	0.006 (0.001)	1.1e-7 (0.1)	1.6e+0 (0.3)
DSB26	606	1:3:9	0.94	-142.4 (23.4)	16.7 (0.2)	0.95	1.8e+7 (0.4)	0.007 (0.001)	1.1e-7 (0.2)	2.0e+0 (0.6)
DSB22	225	1:3:7	0.78	-219.5 (23.5)	18.1 (0.2)	0.98	7.3e+7 (1.3)	0.005 (0.000)	7.2e-7 (0.8)	5.3e+1 (1.1)
Continuous decompression, $XH_2O^{fl} = 0.8$										
DSB35	284	1:5:7	0.91	-748.8 (267.3)	17.8 (1.0)	0.89	5.4e+7 (5.2)	0.001 (0.000)	3.7e-9 (1.3)	2.0e-1 (2.0)
DSB38	293	1:4:7	0.90	-248.3 (43.8)	17.4 (0.3)	0.94	3.5e+7 (1.0)	0.004 (0.001)	7.5e-9 (1.3)	2.6e-1 (0.9)
DSB34	574	1:4:8	0.87	-294.9 (25.0)	17.7 (0.1)	0.98	5.0e+7 (0.6)	0.003 (0.000)	5.4e-9 (0.5)	2.7e-1 (0.4)
DSB36	300	1:4:9	0.88	-123.4 (12.8)	15.9 (0.1)	0.98	8.1e+6 (0.8)	0.008 (0.001)	2.3e-7 (0.2)	1.8e+0 (0.3)
DSB37	418	1:4:7	0.88	-176.9 (20.5)	17.4 (0.2)	0.96	3.8e+7 (0.7)	0.006 (0.001)	1.0e-7 (0.1)	3.9e+0 (0.9)
DSB33	656	1:4:8	0.85	-201.3 (20.8)	17.8 (0.2)	0.97	5.3e+7 (0.8)	0.005 (0.001)	7.9e-8 (0.8)	4.2e+0 (0.8)
Single-step decompression, $XH_2O^{fl} = 1.0$										
DSB23	873	1:3:9	0.83	-197.0 (22.0)	17.4 (0.2)	0.98	3.8e+7 (0.6)	0.005 (0.001)	5.9e-8 (0.7)	2.2e+0 (0.4)
DSB13	407	1:3:9	0.79	-167.4 (17.2)	19.1 (0.2)	0.96	1.9e+8 (0.4)	0.006 (0.001)	6.9e-8 (0.7)	1.3e+1 (0.3)
DSB17	373	1:4:7	0.88	-256.0 (65.8)	16.8 (0.5)	0.94	1.9e+7 (0.9)	0.004 (0.001)	6.5e-9 (1.7)	1.2e-1 (0.7)
DSB24	246	1:4:8	0.71	-211.7 (32.0)	19.8 (0.3)	0.94	3.9e+8 (1.1)	0.005 (0.001)	7.8e-9 (1.2)	3.0e+0 (1.0)

[a] Number of crystals measured

[b] Three-dimensional crystal shape (*s* = short axis, *i* = intermediate axis, *l* = long axis) calculated using CSDSlice (Morgan and Jerram, 2006). The r^2 value is a goodness of fit parameter output by the software.

[c] CSD regressions for crystals formed during decompression (except for equilibrium reference runs, where regressions are fit to all points but the downturn at small or large size classes). Parentheses give uncertainties propagated from the standard errors of regression slope and/or intercept.

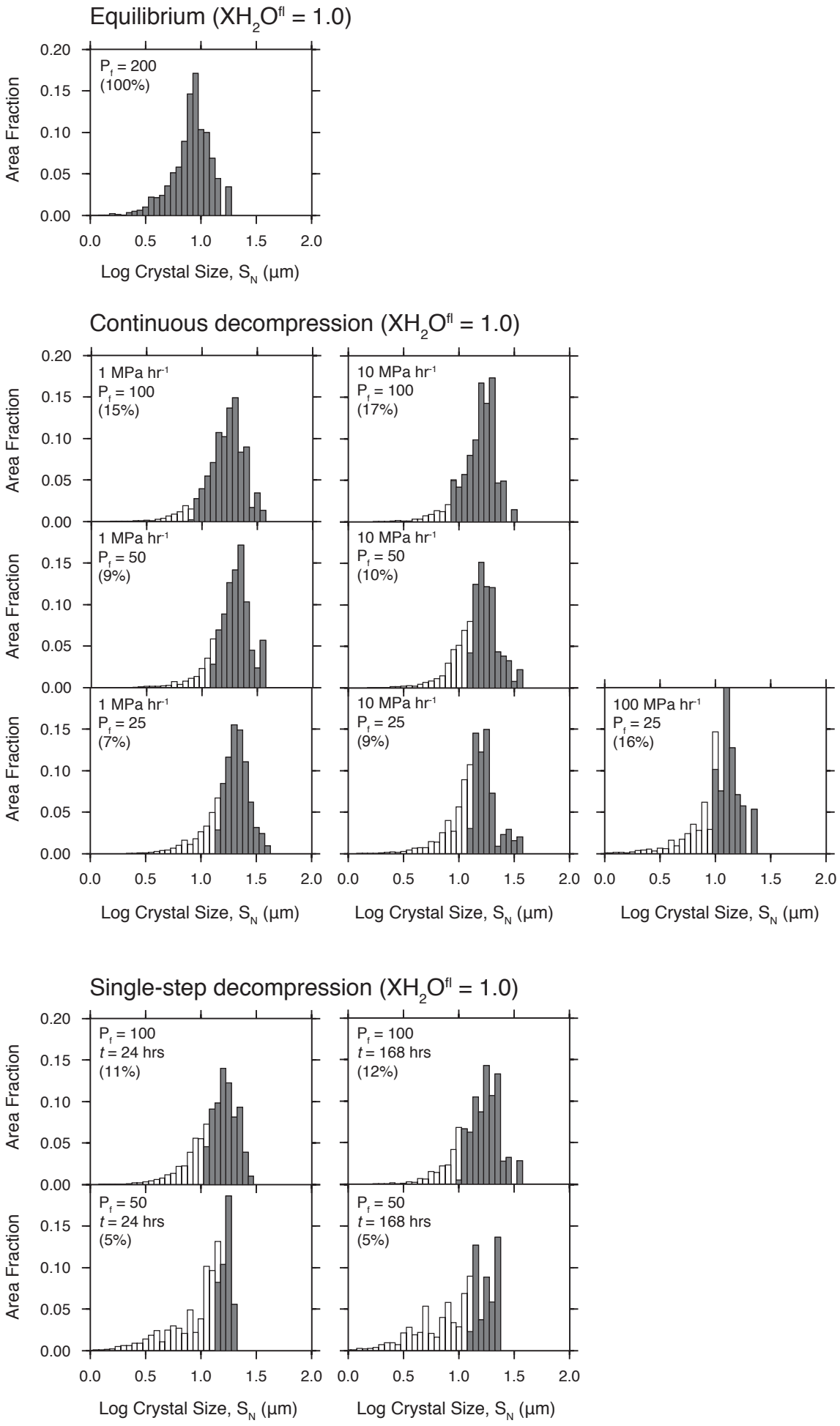

Figure S1a. Size histograms, as area fraction, of plagioclase in H_2O-saturated experiments. Data for crystals formed during the anneal period are overlain in grey. Anneal crystals are designated using the areal number density of plagioclase in the corresponding equilibrium reference sample, assuming the largest crystals in decompressed samples formed during equilibration. Parenethses give the percentage of total crystal area represented by the cores of anneal crystals.

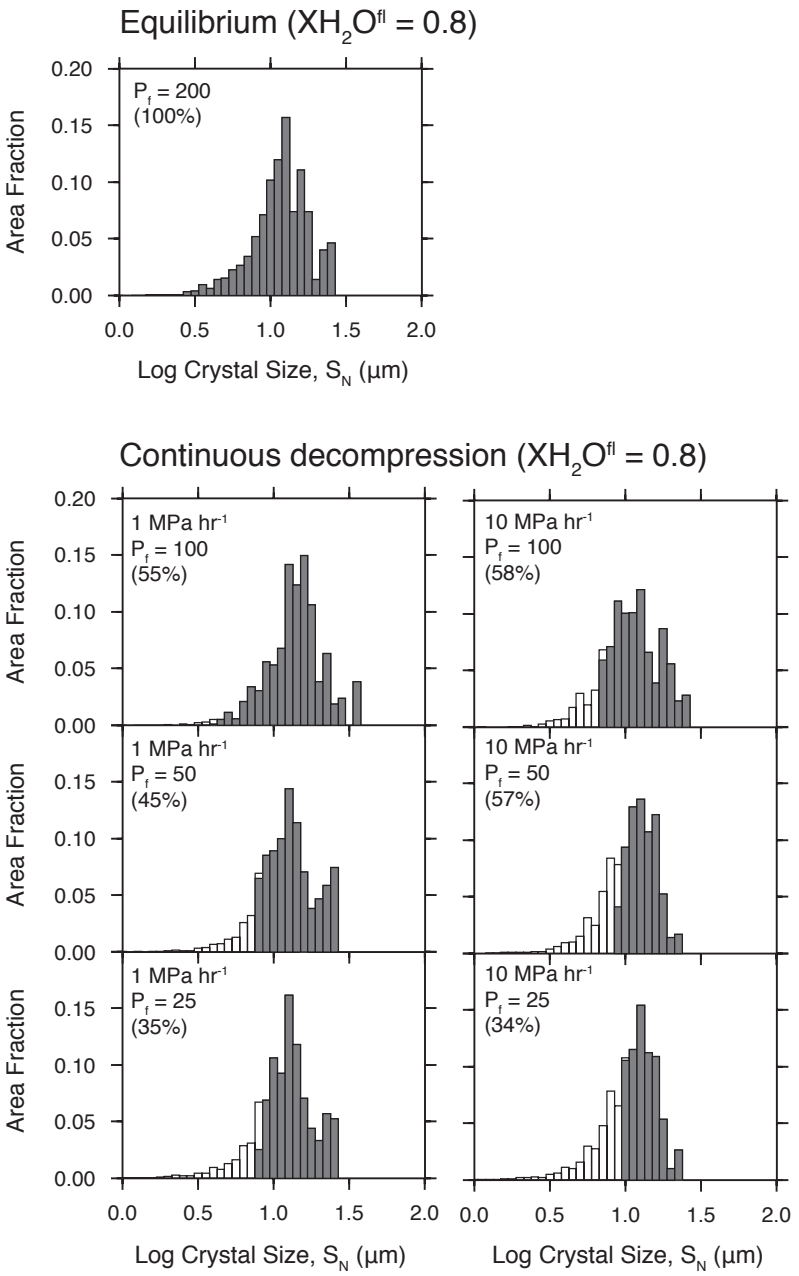

Figure S1b. Size histograms, as area fraction, of plagioclase in H_2O–CO_2-saturated experiments. Data for crystals formed during the anneal period are overlain in grey. Anneal crystals are designated using the areal number density of plagioclase in the corresponding equilibrium reference sample, assuming the largest crystals in decompressed samples formed during equilibration. Parenethses give the percentage of total crystal area represented by the cores of anneal crystals.

Table S1: Major element compositions of experimental glasses measured by electron microprobe (wt% anhydrous)

Sample	SiO_2	TiO_2	Al_2O_3	FeO_T	MnO	MgO	CaO	Na_2O	K_2O	P_2O_5	H_2O [a]	Total [b]	n [c]
DSB6	71.09 (0.30)	0.30 (0.02)	15.97 (0.10)	2.08 (0.10)	0.02 (0.03)	0.76 (0.05)	2.88 (0.07)	4.91 (0.24)	1.88 (0.13)	0.10 (0.03)	6.52 (0.34)	93.47	15
DSB19	74.15 (0.36)	0.31 (0.02)	14.34 (0.16)	1.65 (0.35)	0.07 (0.05)	0.66 (0.05)	1.65 (0.05)	4.84 (0.20)	2.19 (0.10)	0.14 (0.03)	4.63 (0.31)	95.38	15
DSB9	75.61 (0.41)	0.26 (0.05)	13.40 (0.30)	1.70 (0.20)	0.10 (0.07)	0.29 (0.06)	1.07 (0.04)	4.91 (0.27)	2.53 (0.11)	0.14 (0.02)	3.61 (0.54)	96.41	15
DSB18	76.42 (0.81)	0.31 (0.03)	13.14 (0.51)	1.05 (0.11)	0.04 (0.05)	0.36 (0.05)	0.76 (0.11)	4.96 (0.33)	2.82 (0.08)	0.13 (0.03)	2.19 (0.44)	97.80	15
DSB16	72.82 (0.27)	0.30 (0.03)	15.06 (0.22)	1.71 (0.15)	0.08 (0.04)	0.75 (0.04)	2.20 (0.10)	4.81 (0.15)	2.14 (0.10)	0.12 (0.03)	4.12 (0.51)	95.89	15
DSB28	74.09 (0.45)	0.24 (0.02)	14.16 (0.24)	1.94 (0.13)	0.08 (0.06)	0.54 (0.05)	1.53 (0.06)	4.87 (0.39)	2.41 (0.11)	0.14 (0.03)	3.75 (0.76)	96.25	15
DSB26	74.58 (0.77)	0.30 (0.04)	14.07 (0.33)	1.41 (0.17)	0.05 (0.04)	0.59 (0.07)	1.35 (0.11)	5.02 (0.24)	2.53 (0.11)	0.11 (0.03)	2.40 (0.39)	97.61	15
DSB22	71.83 (0.30)	0.30 (0.02)	15.40 (0.21)	1.83 (0.10)	0.07 (0.03)	0.80 (0.04)	2.54 (0.09)	5.06 (0.32)	2.09 (0.11)	0.09 (0.02)	2.59 (0.51)	97.42	15
DSB39	73.92 (0.37)	0.32 (0.02)	14.51 (0.18)	1.55 (0.13)	0.07 (0.05)	0.54 (0.05)	1.95 (0.04)	4.78 (0.37)	2.27 (0.11)	0.11 (0.04)	5.52 (0.58)	94.48	15
DSB35	75.05 (0.33)	0.33 (0.02)	13.87 (0.16)	1.43 (0.06)	0.05 (0.05)	0.56 (0.04)	1.42 (0.06)	4.94 (0.30)	2.23 (0.09)	0.11 (0.02)	4.26 (0.64)	95.73	10
DSB38	75.71 (0.59)	0.33 (0.08)	13.00 (0.23)	1.81 (0.13)	0.04 (0.04)	0.30 (0.07)	1.01 (0.09)	4.99 (0.25)	2.67 (0.11)	0.14 (0.04)	3.35 (0.75)	96.64	15
DSB34	75.80 (0.56)	0.34 (0.03)	13.36 (0.25)	1.30 (0.06)	0.09 (0.07)	0.52 (0.09)	0.99 (0.06)	4.81 (0.27)	2.66 (0.12)	0.14 (0.04)	3.31 (0.60)	96.69	14
DSB36	74.63 (0.35)	0.14 (0.02)	14.15 (0.26)	1.44 (0.11)	0.07 (0.05)	0.63 (0.06)	1.58 (0.07)	4.94 (0.26)	2.31 (0.15)	0.11 (0.02)	4.47 (0.48)	95.53	10
DSB37	75.34 (0.54)	0.28 (0.03)	13.39 (0.35)	1.77 (0.08)	0.07 (0.06)	0.37 (0.08)	1.25 (0.09)	4.83 (0.24)	2.58 (0.20)	0.12 (0.03)	3.44 (0.66)	96.55	15
DSB33	76.74 (0.38)	0.36 (0.03)	12.97 (0.29)	1.22 (0.09)	0.07 (0.10)	0.36 (0.08)	0.73 (0.10)	4.55 (0.23)	2.89 (0.14)	0.12 (0.02)	3.10 (1.01)	96.88	14
DSB23	75.62 (0.45)	0.22 (0.04)	13.80 (0.14)	1.28 (0.14)	0.07 (0.05)	0.52 (0.05)	1.38 (0.07)	4.66 (0.29)	2.34 (0.18)	0.11 (0.02)	4.76 (0.60)	95.25	15
DSB13	76.98 (1.34)	0.18 (0.06)	12.98 (0.74)	1.04 (0.12)	0.09 (0.08)	0.38 (0.08)	0.76 (0.11)	4.34 (0.40)	3.13 (0.10)	0.12 (0.02)	3.75 (0.77)	96.25	15
DSB25	77.28 (1.26)	0.30 (0.05)	12.70 (0.71)	1.16 (0.20)	0.04 (0.04)	0.23 (0.05)	0.70 (0.12)	4.12 (0.33)	3.33 (0.17)	0.14 (0.03)	2.65 (0.58)	97.34	15
DSB17	74.25 (0.25)	0.27 (0.05)	14.01 (0.12)	1.95 (0.11)	0.06 (0.05)	0.43 (0.05)	1.68 (0.04)	4.86 (0.22)	2.36 (0.10)	0.13 (0.03)	4.57 (0.52)	95.44	15
DSB24	80.01 (0.28)	0.21 (0.03)	11.19 (0.15)	0.85 (0.09)	0.03 (0.04)	0.15 (0.03)	0.54 (0.05)	3.86 (0.21)	3.04 (0.16)	0.10 (0.04)	3.57 (0.40)	96.41	15
DSB27	78.34 (0.89)	0.27 (0.04)	12.08 (0.63)	1.04 (0.06)	0.06 (0.06)	0.13 (0.04)	0.70 (0.26)	3.87 (0.25)	3.40 (0.28)	0.11 (0.01)	2.03 (0.29)	97.96	10

Parentheses give 1σ precision on multiple analyses.

[a] H_2O estimated as volatiles by difference

[b] Unnormalised total

[c] Number of analyses

Table S2: Major element compositions of representative experimental plagioclase cores and rims measured by electron microprobe

Sample [a]	SiO_2	TiO_2	Al_2O_3	FeO_T	MnO	MgO	CaO	Na_2O	K_2O	P_2O_5	An [b]	Ab [b]	Or [b]	Total
DSB6_c	56.31 (1.08)	0.06 (0.01)	27.34 (0.28)	0.89 (0.08)	0.00 (0.04)	0.07 (0.02)	10.25 (0.20)	5.42 (0.35)	0.20 (0.04)	0.03 (0.01)	49.3	48.3	1.17	100.56
DSB19_c	54.77 (1.26)	0.02 (0.02)	28.08 (0.60)	0.57 (0.06)	0.01 (0.07)	0.01 (0.02)	11.16 (0.20)	5.37 (0.33)	0.12 (0.03)	0.02 (0.01)	51.9	46.3	0.68	100.12
DSB19_r	56.80 (0.62)	0.02 (0.01)	27.11 (0.67)	0.64 (0.06)	0.01 (0.05)	0.04 (0.02)	9.45 (0.23)	5.99 (0.38)	0.16 (0.03)	0.02 (0.01)	46.1	52.9	0.93	100.25
DSB9_c	55.43 (0.60)	0.02 (0.01)	27.74 (0.68)	0.50 (0.05)	0.01 (0.05)	0.03 (0.02)	10.03 (0.24)	5.78 (0.37)	0.14 (0.03)	0.03 (0.01)	48.6	50.6	0.80	99.69
DSB9_r	57.85 (0.63)	0.02 (0.01)	26.36 (0.65)	0.46 (0.06)	0.05 (0.05)	0.04 (0.02)	8.78 (0.22)	6.61 (0.41)	0.20 (0.04)	0.03 (0.01)	41.9	57.0	1.11	100.39
DSB18_c	53.86 (0.59)	0.05 (0.01)	27.54 (0.68)	2.18 (0.10)	0.06 (0.05)	0.09 (0.02)	10.21 (0.25)	5.34 (0.35)	0.13 (0.03)	0.01 (0.01)	51.0	48.2	0.76	99.46
DSB18_r	59.28 (0.64)	0.03 (0.01)	25.15 (0.62)	0.52 (0.06)	0.01 (0.05)	0.03 (0.02)	6.92 (0.18)	7.39 (0.45)	0.23 (0.04)	0.03 (0.01)	33.7	65.0	1.30	99.58
DSB16_c	55.38 (1.28)	0.02 (0.02)	28.19 (0.60)	0.65 (0.07)	0.00 (0.08)	0.00 (0.02)	10.88 (0.20)	5.30 (0.32)	0.11 (0.04)	0.01 (0.01)	51.6	46.5	0.64	100.54
DSB16_r	56.83 (0.61)	0.02 (0.01)	27.51 (0.67)	0.63 (0.06)	0.00 (0.03)	0.07 (0.02)	9.81 (0.17)	5.81 (0.37)	0.18 (0.03)	0.03 (0.01)	47.8	51.2	1.03	100.88
DSB28_c	55.17 (0.61)	0.06 (0.01)	27.60 (0.68)	1.07 (0.07)	0.00 (0.05)	0.06 (0.02)	10.34 (0.18)	5.41 (0.35)	0.12 (0.03)	0.02 (0.01)	51.0	48.3	0.71	99.85
DSB28_r	57.24 (0.62)	0.03 (0.01)	26.96 (0.66)	0.53 (0.06)	0.01 (0.05)	0.03 (0.02)	9.20 (0.17)	6.26 (0.39)	0.16 (0.04)	0.01 (0.01)	44.4	54.7	0.94	100.42
DSB26_c	54.74 (0.87)	0.01 (0.01)	27.88 (0.78)	0.59 (0.06)	0.00 (0.05)	0.04 (0.02)	10.51 (0.23)	5.56 (0.44)	0.13 (0.04)	0.02 (0.01)	50.7	48.6	0.76	99.49
DSB26_r	57.38 (0.91)	0.02 (0.01)	26.41 (0.74)	0.63 (0.06)	0.00 (0.05)	0.04 (0.02)	9.00 (0.20)	6.36 (0.49)	0.17 (0.04)	0.01 (0.01)	43.5	55.6	0.97	100.01
DSB22_c	54.99 (0.60)	0.04 (0.01)	28.00 (0.69)	0.63 (0.06)	0.02 (0.05)	0.03 (0.02)	10.84 (0.19)	5.29 (0.35)	0.14 (0.03)	0.01 (0.01)	52.7	46.5	0.82	99.98
DSB22_r	56.59 (0.62)	0.03 (0.01)	26.83 (0.66)	0.63 (0.06)	0.00 (0.05)	0.04 (0.02)	9.73 (0.17)	5.76 (0.37)	0.19 (0.04)	0.02 (0.01)	47.7	51.1	1.13	99.80
DSB39_c	55.91 (0.88)	0.07 (0.01)	26.65 (0.78)	1.10 (0.07)	0.01 (0.05)	0.05 (0.02)	9.43 (0.22)	5.81 (0.46)	0.17 (0.03)	0.03 (0.01)	46.8	52.2	1.00	99.23
DSB35_c	56.47 (0.90)	0.04 (0.01)	26.86 (0.76)	0.85 (0.07)	0.03 (0.05)	0.12 (0.02)	9.31 (0.20)	5.85 (0.46)	0.21 (0.04)	0.01 (0.01)	46.2	52.6	1.25	99.75
DSB35_r	56.19 (0.89)	0.03 (0.01)	27.34 (0.77)	0.66 (0.07)	0.02 (0.05)	0.06 (0.02)	9.73 (0.21)	5.75 (0.45)	0.18 (0.04)	0.02 (0.01)	47.8	51.1	1.07	99.99
DSB38_c	56.19 (0.89)	0.02 (0.01)	27.18 (0.76)	0.55 (0.06)	0.04 (0.05)	0.06 (0.02)	9.90 (0.21)	5.65 (0.44)	0.17 (0.04)	0.01 (0.01)	48.7	50.3	1.01	99.77
DSB38_r	60.25 (0.95)	0.04 (0.01)	24.40 (0.69)	0.46 (0.06)	0.00 (0.06)	0.06 (0.02)	7.26 (0.16)	6.65 (0.51)	0.37 (0.05)	0.01 (0.01)	36.8	61.0	2.25	99.51
DSB34_c	57.46 (0.91)	0.08 (0.01)	24.78 (0.70)	1.12 (0.08)	0.01 (0.05)	0.48 (0.03)	8.38 (0.19)	5.77 (0.45)	0.41 (0.05)	0.02 (0.01)	43.4	54.1	2.54	98.52
DSB34_r	60.23 (0.95)	0.07 (0.01)	23.71 (0.67)	0.77 (0.07)	0.00 (0.05)	0.11 (0.02)	7.39 (0.17)	5.64 (0.44)	0.60 (0.06)	0.04 (0.01)	40.4	55.8	3.88	98.57
DSB36_c	56.99 (0.90)	0.03 (0.01)	26.86 (0.76)	1.12 (0.08)	0.02 (0.05)	0.07 (0.02)	9.11 (0.20)	5.99 (0.47)	0.19 (0.04)	0.01 (0.01)	45.2	53.7	1.12	100.40
DSB36_r	58.63 (0.93)	0.07 (0.01)	25.20 (0.71)	1.28 (0.09)	0.01 (0.05)	0.10 (0.02)	7.99 (0.18)	6.25 (0.49)	0.37 (0.05)	0.02 (0.01)	40.5	57.3	2.23	99.92
DSB37_c	56.65 (0.62)	0.02 (0.01)	27.53 (0.68)	0.54 (0.06)	0.01 (0.05)	0.06 (0.02)	9.81 (0.17)	5.77 (0.37)	0.15 (0.04)	0.02 (0.01)	48.0	51.1	0.90	100.56
DSB37_r	58.41 (0.64)	0.05 (0.01)	25.75 (0.63)	0.91 (0.07)	0.00 (0.05)	0.17 (0.02)	8.24 (0.15)	6.69 (0.42)	0.26 (0.04)	0.02 (0.01)	39.9	58.6	1.51	100.49
DSB33_c	56.47 (0.90)	0.04 (0.01)	26.54 (0.75)	1.26 (0.09)	0.03 (0.05)	0.19 (0.02)	9.35 (0.20)	5.88 (0.46)	0.22 (0.04)	0.02 (0.01)	46.2	52.5	1.28	100.01

Sample [a]	SiO_2	TiO_2	Al_2O_3	FeO_T	MnO	MgO	CaO	Na_2O	K_2O	P_2O_5	An [b]	Ab [b]	Or [b]	Total
DSB33_r	59.89 (0.95)	0.14 (0.01)	23.92 (0.67)	1.29 (0.09)	0.02 (0.05)	0.09 (0.02)	7.56 (0.17)	5.98 (0.47)	0.59 (0.06)	0.02 (0.01)	39.6	56.7	3.66	99.49
DSB23_c	55.55 (0.62)	0.03 (0.01)	27.71 (0.67)	1.00 (0.07)	0.03 (0.05)	0.07 (0.02)	10.02 (0.24)	5.42 (0.38)	0.13 (0.03)	0.03 (0.01)	50.1	49.1	0.77	99.98
DSB23_r	58.62 (0.64)	0.02 (0.01)	25.64 (0.61)	0.64 (0.06)	0.01 (0.05)	0.04 (0.02)	7.80 (0.19)	6.87 (0.39)	0.19 (0.05)	0.02 (0.01)	38.1	60.8	1.08	99.84
DSB13_c	56.28 (0.61)	0.03 (0.01)	26.85 (0.66)	0.83 (0.07)	0.00 (0.06)	0.05 (0.02)	9.63 (0.17)	5.94 (0.38)	0.15 (0.03)	0.02 (0.01)	46.9	52.3	0.85	99.79
DSB13_r	60.49 (0.65)	0.02 (0.01)	23.90 (0.59)	0.58 (0.06)	0.00 (0.05)	0.05 (0.02)	6.82 (0.13)	6.94 (0.43)	0.33 (0.05)	0.06 (0.01)	34.5	63.5	2.01	99.18
DSB25_c	55.56 (0.88)	0.02 (0.01)	27.73 (0.78)	0.77 (0.07)	0.00 (0.05)	0.05 (0.02)	10.19 (0.22)	5.63 (0.44)	0.17 (0.04)	0.03 (0.01)	49.5	49.5	0.95	100.15
DSB25_r	59.10 (0.93)	0.04 (0.01)	24.92 (0.70)	0.82 (0.07)	0.00 (0.05)	0.08 (0.02)	7.70 (0.17)	6.59 (0.51)	0.30 (0.05)	0.05 (0.01)	38.5	59.7	1.82	99.60
DSB17_c	54.68 (0.60)	0.02 (0.01)	27.67 (0.68)	0.99 (0.07)	0.00 (0.05)	0.06 (0.02)	10.54 (0.26)	5.24 (0.34)	0.14 (0.04)	0.02 (0.01)	52.2	47.0	0.81	99.34
DSB17_r	58.02 (0.63)	0.04 (0.01)	25.35 (0.62)	0.72 (0.06)	0.00 (0.06)	0.08 (0.02)	8.01 (0.20)	6.30 (0.40)	0.32 (0.05)	0.03 (0.01)	40.5	57.6	1.92	98.86
DSB24_c	56.31 (0.61)	0.04 (0.01)	26.67 (0.65)	1.14 (0.07)	0.00 (0.05)	0.06 (0.02)	9.46 (0.17)	6.06 (0.38)	0.13 (0.03)	0.02 (0.01)	46.0	53.3	0.76	99.88
DSB24_r	57.10 (0.62)	0.06 (0.01)	25.63 (0.63)	1.38 (0.08)	0.02 (0.05)	0.06 (0.02)	8.28 (0.15)	6.51 (0.41)	0.25 (0.04)	0.02 (0.01)	40.7	57.9	1.45	99.30
DSB27_c	54.81 (0.60)	0.02 (0.01)	27.28 (0.67)	1.02 (0.07)	0.02 (0.05)	0.06 (0.02)	10.40 (0.18)	5.43 (0.35)	0.17 (0.03)	0.02 (0.01)	50.9	48.1	0.98	99.23
DSB27_r	58.95 (0.64)	0.04 (0.01)	25.16 (0.62)	0.79 (0.07)	0.00 (0.05)	0.06 (0.02)	7.90 (0.15)	6.47 (0.41)	0.39 (0.05)	0.04 (0.01)	39.3	58.3	2.34	99.81

Parentheses give 1σ precision based on counting statistics.

Occasional elevated FeO_T values reflect oxide micro-inclusions that could not be avoided in all crystals.

[a] c = core, r = rim

[b] mol% anorthite (An), albite (Ab), and orthoclase (Or)